

Copyright  
by  
Steen Brian Schougaard  
2002

The Dissertation Committee for Steen Brian Schougaard  
certifies that this is the approved version of the following dissertation:

**DEVELOPMENT AND STUDY OF HIGH- $T_C$   
SUPERCONDUCTOR CONDUCTIVE POLYMER  
ASSEMBLIES**

Committee:

---

John T. McDevitt, Supervisor

---

John T. Markert

---

Paul F. Barbara

---

Keith Stevenson

---

David A. Vanden Bout

**DEVELOPMENT AND STUDY OF HIGH- $T_C$   
SUPERCONDUCTOR CONDUCTIVE POLYMER  
ASSEMBLIES**

by

**STEEN BRIAN SCHOUGAARD, M.S.**

**DISSERTATION**

Presented to the Faculty of the Graduate School of  
The University of Texas at Austin  
in Partial Fulfillment  
of the Requirements  
for the Degree of

**DOCTOR OF PHILOSOPHY**

THE UNIVERSITY OF TEXAS AT AUSTIN

December 2002

## Acknowledgments

There is a large number of people and institutions without who this dissertation would never have been possible. I would like to thank my former supervisor Prof. Thomas Bjørnholm who suggested that I apply for Graduate School at The University of Texas and who has been a good collaborator on the characterization of monolayer by X-ray diffraction. I would also like to thank the people whom facilitated individual components for the single crystal SAM work, without their prior knowledge and help the amount of work required would have been enormous. Thus, I would like to thank Koki Mochizuki and Prof. John Markert who facilitated the crystals, David Derro who showed me how to mount and cleave them, T. Randall Lee and coworker who synthesized the semi-fluorinated alkyl amines, and Robert Feidenhans'l and coworkers for their time spent collecting diffraction data on the SAM modified single crystals. I would also like to thank the Langmuir film diffraction group, especially Niels Reitzel and Thomas Bjørnholm for the structural determination of the semi fluorinated alkyl amine monolayer on water.

During the synthesis work I had great help from Suzanne Tobey, who showed me the ins and outs of hydrogenation of nitriles. I would also like to thank Prof. Alex De Lozanne for allowing me to use their AFM until our own could be upgraded.

The people of the McDevitt group deserve much praise for their help with this dissertation work: Chris T. Jones for the work with contact resistance, Bill Murray who introduced me to the practical aspects of PLD, Cyndi Wells for her work on the structure of the semi-fluorinated alkyl amine monolayer, Andrea Wells who introduced me to the practical aspects of electrochemistry, Adrian Goodey who proof read parts of this dissertation and lastly Sungwook Kim whose endless persistence during the PLD work is the source of the most of the successful outcome. Also belonging to the group of people deserving my thanks are the undergraduates: Brian Pallohusky, Mehnaaz Ali, and Glen Simmons, from whom I learned a great deal about instructing and communication.

I would also like to thank Prof. John T. McDevitt, who always allowed me to pursue any idea I might have, though they may not always have seemed worth pursuing to him. The funding for much of the work in this dissertation was provided by the Danish Research Agency, this institution and it's employees have been understanding and extremely helpful during this entire endeavor.

Finally, I would like to thank my girlfriend Janine Mauzeroll who have provided love, support and care during the preparation of this manuscript.

# DEVELOPMENT AND STUDY OF HIGH- $T_c$ SUPERCONDUCTOR CONDUCTIVE POLYMER ASSEMBLIES

Publication No. \_\_\_\_\_

Steen Brian Schougaard, Ph.D.  
The University of Texas at Austin, 2002

Supervisor: John T. McDevitt

This dissertation presents the development and study of organic polymeric conductor/High- $T_c$  superconductor bilayers, for exploration of the superconductor proximity effect. A major obstacle to this research is the instability of the High- $T_c$  superconductor towards  $H_2O$  and  $CO_2$  as it is necessary to create hybrid structures where the two conductors have intimate contact. For this reason, a study of the corrosion characteristics of the  $RBa_2Cu_3O_7$  ( $R=Y, Eu, Nd$ ) series was undertaken. In this study,  $R=Nd$  was shown to have enhanced corrosion resistance.

In an effort to develop chemical processing methods that allow for the production of intimate contact between the cuprate superconductor and the conductive polymer systems, a study of alkyl amine adsorbed onto the surface

of the superconductor is presented. In the electrochemical part of the study, alkyl amine ferrocene adsorbed onto the surface revealed that the amines are strongly adhered to the superconductor while still allowing electrons to pass from the superconductor to the ferrocene moiety. The self-assembled monolayer (SAM) structure of  $\text{CF}_3(\text{CF}_2)_3(\text{CH}_2)_{11}\text{NH}_2$  atop the superconductor was elucidated by employing several techniques, including atomic scale atomic force microscopy (AFM).

A novel multistep bilayer sample preparation protocol is presented involving thin film fabrication by pulsed laser deposition (PLD), patterning by shadow mask ablation, sample thinning by scanning probe and electropolymerization of the polymer. Scanning probe thinning yields a smooth superconductor surface, a known superconductor thickness, and if a blocking layer is employed prior to thinning, the localization of polymer growth.

Studies of the response of a bilayer structure of  $\text{Y}_{0.6}\text{Ca}_{0.4}\text{Ba}_{1.6}\text{La}_{0.4}\text{Cu}_3\text{O}_7$ /poly pyrrole to polymer redox cycling showed a semi-reversible suppression of transition temperature qualitatively consistent with a combination of corrosion and superconductor proximity effect. Quantitative analysis in the framework of the proximity effect shows evidence suggestive of an unexpected long superconductor coherence length. A qualitative model based on grain boundaries is postulated to explain this effect.

# Table of Contents

<b>Acknowledgments</b>	<b>iv</b>
<b>Abstract</b>	<b>vi</b>
<b>List of Tables</b>	<b>xi</b>
<b>List of Figures</b>	<b>xii</b>
<b>Chapter 1. Introduction</b>	<b>1</b>
1.1 Organic polymeric conductors . . . . .	4
1.2 Introduction to superconductivity . . . . .	9
1.3 On the measurement of the critical curve J vs. T . . . . .	13
1.4 Coupling of superconducting states: The Josephson junction .	16
1.5 Josephson junctions in magnetic fields . . . . .	20
1.6 The superconducting proximity effect . . . . .	25
<b>Chapter 2. The Superconductor: Structure and preparation</b>	<b>32</b>
2.1 Structure of the superconductors . . . . .	34
2.2 The effect of crystal orientation on electronic properties . . . .	36
2.3 Experimental: Preparation and characterization of polycrystalline bulk superconductors . . . . .	38
2.4 Experimental: Measurement of superconductor corrosion stability	39
2.5 Corrosion mechanism and stability of $\text{RBa}_2\text{Cu}_3\text{O}_{7\pm\delta}$ phases . .	40
2.6 Thin films growth by Pulsed Laser Deposition (PLD) . . . . .	45
2.7 Experimental: PLD setup . . . . .	52
2.8 Experimental: PLD procedure . . . . .	56
2.9 Experimental: Characterization of thin films . . . . .	58
2.10 On the thin films grown by PLD . . . . .	58



<b>Chapter 3. Self-assembled monolayers (SAM) on copper oxide superconductors</b>	<b>66</b>
3.1 Experimental: Fabrication and characterization of monolayer modified superconductor surfaces . . . . .	67
3.2 Experimental: Synthesis of molecules for surface modification .	70
3.3 On the chemical evidence for an adsorbed monolayer . . . . .	72
3.4 Characterization of SAMs atop <i>ab</i> -plane of single crystal $\text{YBa}_2\text{Cu}_3\text{O}_{7-\delta}$ . . . . .	78
<b>Chapter 4. Superconductor conductive polymer assemblies</b>	<b>88</b>
4.1 Superconductor/conductive polymer bilayer preparation . . .	89
4.1.1 Experimental: Preparation of $100\mu\text{m}$ wide superconducting bridge structure by ablation through a shadow mask	93
4.1.2 Experimental: Preparation of localized thin superconductor structures by Atomic Force Microscope (AFM) Machining . . . . .	94
4.1.3 Experimental: Formation of blocking layer and pyrrole tether layer . . . . .	97
4.1.4 Experimental: Electropolymerization of pyrrole . . . . .	97
4.2 Characterization of polymer-superconductor assemblies . . . .	98
<b>Chapter 5. On the superconductive properties of high-temperature superconductor/conductive polymer assemblies</b>	<b>108</b>
5.1 On the measurement of contact resistance of superconductor/normal conductor (S/N) interfaces . . . . .	109
5.2 Order parameter suppression at the S/N boundary . . . . .	115
5.3 Experimental: $S/\frac{N}{S}/S$ sample preparation and transport measurements . . . . .	119
5.4 $S/\frac{N}{S}/S$ sample geometry . . . . .	120
5.5 Current transport properties of the $S/\frac{N}{S}/S$ superconductor conductive polymer bilayer structure . . . . .	126
5.6 Analysis and discussion of current transport properties of superconductor/conductive polymer bilayers . . . . .	134
<b>Chapter 6. Closing remarks</b>	<b>143</b>
<b>Appendix</b>	<b>146</b>

<b>Appendix A. Calculation of <math>\gamma</math>-values</b>	<b>147</b>
<b>Bibliography</b>	<b>151</b>
<b>Vita</b>	<b>160</b>

## List of Tables

2.1	Superconducting and normal state properties . . . . .	36
2.2	Pellet preparation. . . . .	39
2.3	PLD process parameters. . . . .	48
2.4	Substrate parameters. . . . .	51
2.5	Deposition parameters for optimization . . . . .	59
5.1	Boundary parameters . . . . .	117
5.2	Current transport measurements legend . . . . .	127
5.3	Modulation of $T_c$ for Polypyrrole/ $\text{YBa}_2\text{Cu}_3\text{O}_7$ bilayers . . . .	136
5.4	Superconductive properties of oxygen deficient single crystal .	140

## List of Figures

1.1	W.A. Little's proposed polymeric superconductor . . . . .	2
1.2	Conductive organic polymeric systems . . . . .	4
1.3	Oxidized polymer state . . . . .	5
1.4	Polymer structure schematic . . . . .	8
1.5	Meissner state vs. perfect conductor . . . . .	10
1.6	Cooper pair formation . . . . .	10
1.7	The critical surface . . . . .	12
1.8	Sample for measuring current transport properties . . . . .	14
1.9	Characteristic current transport curves . . . . .	15
1.10	Josephson junction in a magnetic field . . . . .	21
1.11	Josephson Fraunhofer pattern . . . . .	24
1.12	Suppression of superconductivity by proximity effect . . . . .	26
1.13	IV-characteristics of a S/N/S-junction . . . . .	28
2.1	The crystal structure of $\text{YBa}_2\text{Cu}_3\text{O}_7$ . . . . .	35
2.2	Current transport as a function of crystallographic grain orientation . . . . .	37
2.3	Accelerated corrosion. . . . .	41
2.4	Water penetration into the 123 system . . . . .	42
2.5	SEM micrographs of corroded samples . . . . .	43
2.6	PLD schematic . . . . .	47
2.7	SEM of particles formed during the PLD process . . . . .	50
2.8	PLD deposition system setup . . . . .	53
2.9	Plume cross-section on substrate holder. . . . .	55
2.10	Diffraction pattern vs. setpoint temperature . . . . .	60
2.11	Transition temperature and width vs. substrate temperature . . . . .	61
2.12	Expanded view of diffraction pattern vs. set-point temperature. . . . .	63
2.13	$a$ -axis oriented $\text{Y}_{0.4}\text{La}_{0.6}\text{Ba}_{1.6}\text{La}_{0.4}\text{Cu}_3\text{O}_7$ film . . . . .	64

2.14	NdBa <sub>2</sub> Cu <sub>3</sub> O <sub>7</sub> film . . . . .	65
3.1	AFM of HOPG reference . . . . .	70
3.2	Removal of corrosion layer by Br <sub>2</sub> /EtOH etch . . . . .	73
3.3	Cyclic voltammograms of electroactive monolayer . . . . .	75
3.4	I <sub>p,red</sub> vs. scan rate . . . . .	77
3.5	Cleaving YBa <sub>2</sub> Cu <sub>3</sub> O <sub>7-δ</sub> structure . . . . .	79
3.6	Optical micrograph of a cleaved crystal . . . . .	80
3.7	AFM of monolayer . . . . .	81
3.8	The proposed SAM structure . . . . .	82
3.9	CF <sub>3</sub> (CF <sub>2</sub> ) <sub>9</sub> (CH <sub>2</sub> ) <sub>11</sub> NH <sub>2</sub> Langmuir monolayer grazing incidence X-ray diffraction . . . . .	83
3.10	X-ray reflectance . . . . .	85
4.1	Sample preparation . . . . .	90
4.2	Final superconductor polymer/bilayer structure . . . . .	92
4.3	The AFM setup . . . . .	95
4.4	Localized polymer growth . . . . .	100
4.5	Intial CV's of a blocked bridge with a 6μm x 90μm opening. . . . .	101
4.6	Polymer growth . . . . .	102
4.7	Polymer delamination . . . . .	103
4.8	Polymer delamination (II) . . . . .	104
4.9	Electron micrograph evidence for strong adhesion of tethered polypyrrole . . . . .	105
4.10	Polymer growth on 3-aminopropyl-N-pyrrole modified sample. . . . .	106
4.11	Doping and undoping cyclic voltammograms . . . . .	107
5.1	Sample setup and equivalent circuit for contact resistance mea- surement . . . . .	109
5.2	Contact resistance on Au/(Pb,Bi) <sub>2</sub> Sr <sub>2</sub> Ca <sub>2</sub> Cu <sub>3</sub> O <sub>7</sub> S/N interface. . . . .	111
5.3	Diffusion of quasi particles and Cooper pair across an S/N in- terface due to proximity effect . . . . .	113
5.4	Order parameter supression at the S/N interface . . . . .	116
5.5	Transition temperature reduction as modeled the theory of Gol- ubov <i>et al.</i> . . . . .	118

5.6	AFM of a bridge before and after thinning . . . . .	121
5.7	Superconductor bridge profile . . . . .	122
5.8	Polymer growth on transport measurement sample . . . . .	123
5.9	Scanning electron micrographs of polymer on current transport sample . . . . .	124
5.10	Polymer morphology . . . . .	125
5.11	Doping and undoping of the superconductor/poly-pyrrole bilayer . . . . .	127
5.12	Resistance vs. temperature for the superconductor/polymer bi- layer . . . . .	128
5.13	Current voltage response of the bilayer below $T_c$ . . . . .	129
5.14	The lack of $T_c$ recovery in the $\text{NdBa}_2\text{Cu}_3\text{O}_{7-\delta}$ samples . . . .	131
5.15	Second redox cycle . . . . .	133
5.16	Transition temperature differences . . . . .	135
5.17	$a$ -axis film morphology . . . . .	138
5.18	Grain boundary junction as it passes from normal conductor to superconducting . . . . .	139
6.1	Superconductor bridge severed by AFM machining . . . . .	145

# Chapter 1

## Introduction

Superconductivity, the conduction of electricity without resistance, in *organic polymeric* materials has been a long standing dream of experimentalists and theoreticians alike. In a 1964 paper, W. A. Little [1] describes how a one-dimensional organic backbone with highly polarizable side-groups would, in theory, allow for superconductivity close to room temperature (Fig 1.1). Little’s purely theoretical paper came at a time when scarcely any work had been done in the area of organic conductors, and helped to initiate this highly active area of research. These new research activities, in turn, lead to the 2000 Nobel prize being awarded to A. J. Heeger, A. G. MacDiarmid and H. Shirakawa “for the discovery and development of conductive polymers” [2].

Little’s original paper exemplifies two key features of *organic polymeric* materials which are uniquely interesting from a fundamental point of view:

- Conductivity is predominantly one-dimensional
- The polymer structure and, thus, the electronic structure can be modified by standard organic transformations

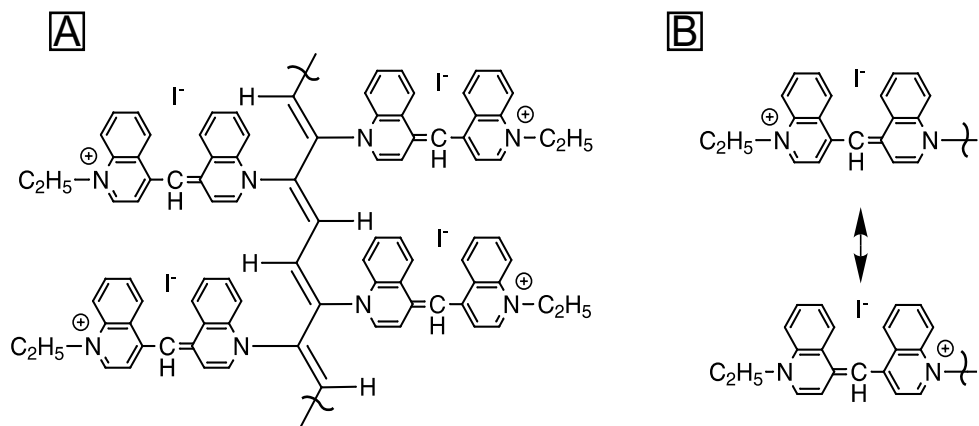


Figure 1.1: W.A. Little's proposed room temperature polymeric superconductor. A) Full structure. B) Resonance structure of the polarizable side-groups.

To date, however, there have been no reports which show a superconducting state in *organic polymeric* conductors. There are, however, several discoveries made since 1964 which makes us optimistic towards the prospects of finding *organic polymeric* superconductivity:

- One case of inorganic polymeric superconductivity is known:  $(\text{SN})_x$  ( $T_c=0.26\text{K}$ ) [3] [4]
- All organic superconductivity have been found in a class of crystalline charge transfer salts collectively known as Bechgaard salts ( $T_c \sim 1.4\text{K}$ ) [4] [5]

Furthermore, several completely new classes of superconductors, which remain superconducting at unprecedented high temperatures, have been dis-



covered, while specific guidelines for their design still remain scarce. Thus, the ability to tailor the molecular structure, control the type and concentration of the charge carrier makes the study of organic polymers in conjunction with superconductivity a very interesting area of research. With this in mind, the goal for this dissertation research was formulated:

*To develop methodologies that allow for the fabrication of high temperature superconductor/organic-conductor composites with well-defined geometries for the study of the superconductor proximity effect in polymers.*

We explore the proximity effect (i.e. the induction of superconductivity in a normal conductor by close contact to a superconductor) because it makes it possible to examine how superconductivity flows into and decays within the polymer. We are thus not attempting to create bulk superconducting state in the polymer, an endeavor for which there is little literature precedence.

The research completed towards the goal stated above is organized in this dissertation as follows. Chapter one is an introduction to the basic properties of organic polymeric conductors and to the principles of superconductivity with the main emphasis on proximity effect and Josephson junctions. Chapter two is a discussion of the characteristics and preparation of high temperature (high- $T_c$ ) ceramic superconductors, which is followed by a discussion of self-assembled monolayers on high- $T_c$  superconductors in Chapter three. Chapter four is concerned with the experimental details and characterization of polymer/high- $T_c$  superconductor assemblies. These assemblies are then used in Chapter five for measurement of the proximity effect between

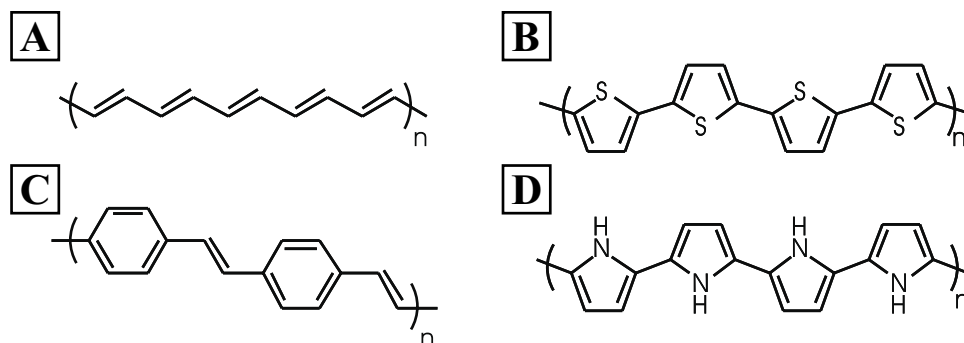


Figure 1.2: Conductive organic polymeric systems. A) Poly-acetylene, B) Poly-thiophene, C) Poly-paravinylene, D) Poly-pyrrole.

the conductive polymer and high- $T_c$  superconductor. The dissertation ends in Chapter six with a short summary and an outlook on what experiments may, in the future be employed, for further study of organic polymer/high- $T_c$  superconductor proximity effects.

Here, the discussion begins with the properties of organic polymeric conductors.

## 1.1 Organic polymeric conductors

Organic polymeric conductors (Fig. 1.2) consist of a backbone of carbon atoms held together by  $\sigma$ -bonds. Perpendicular to this backbone are the  $\pi$ -bonds. It is these  $\pi$ -bonds that are responsible for the conduction of electricity in most organic polymers.

Conduction requires conjugated  $\pi$ -bonds and the monomer

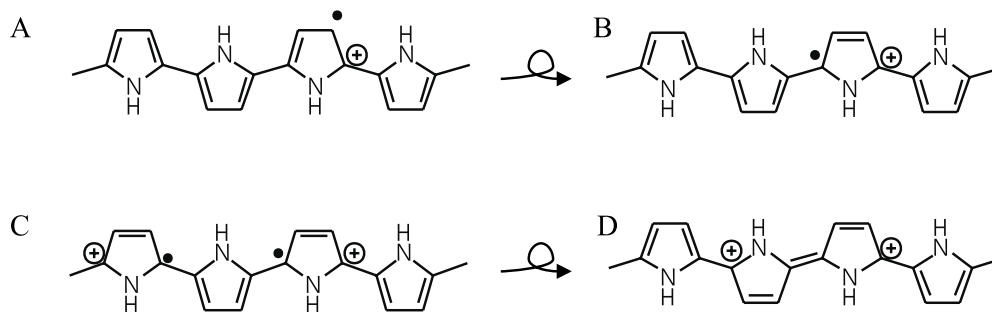


Figure 1.3: Oxidized polymer state. The initial radical cation or polaron before A) and after B) nuclei relaxation. C) Two polarons interact and combine to form a bipolaron (D)

$\pi$ -wavefunctions must therefore have non zero overlap. This is important as monomers with perpendicular backbones do not allow for overlap due to the symmetry of the  $\pi$ -systems. Arranging the monomers in a planar fashion, however, allows for good  $\pi$  overlap and thus strong conjugation. The desired geometry for such polymeric conductors is therefore planar. However, these planar polymers are still poor conductors of electricity in their native (i.e. undoped state) due to the existence of a large bandgap ( $\sim 1.7\text{eV}$  in polyacetylene [4]) between the bonding  $\pi$  and the anti bonding  $\pi^*$  levels. The size of the bandgap may be lowered by removal of electrons (i.e. oxidation) from the  $\pi$ -system. Oxidation is usually accomplished by either chemical doping with agents like  $\text{I}_2(\text{g})$ ,  $\text{AuCl}_3$  [6] or electrochemically. Using electrochemistry or  $\text{I}_2(\text{g})$  makes the reaction reversible (i.e. the polymer can be cycled from the oxidized conducting state to the insulating reduced state and back).

In the most simplistic model of charge transport in polymeric conduc-

tors, removal of *one* electron leaves a radical cation [4](Fig. 1.3A). Since this is no longer a double bond, the nuclei relaxes to the lowest energy state (Fig. 1.3B). The net effect is that a singly occupied state is introduced in the middle of the bandgap. The radical cation can now be moved up and down the  $\pi$ -system by the application of an external electric field. Opposing the movement of charge is both the Coulombic interactions with the counter ion (pinning) and the activation energy associated with distorting the lattice. In most conductive polymer systems, the distortion due to the introduction of one hole (cation) is not limited to one bond, but extends over several units. Thus, as more radical ions are introduced into the polymer by oxidation, the initially separated polarons will start to interact, forming bipolarons (Fig. 1.3C,D). The maximum oxidation state obtainable by chemical means in poly-pyrrole and poly-thiophene is a structure where approximately one in every four units are oxidized. The concentration of charge carriers ( $n$ ) in this state is high enough to where movement of charge up and down the chain requires little energy, i.e. the mobility ( $\mu$ ) is high and, thus, also conductivity ( $\sigma$ ) as

$$\sigma = en\mu \quad (1.1)$$

where  $e$  is the elemental charge.

While high mobilities and large charge carrier concentrations in the molecular strand are a prerequisite for the observation of high macroscopic conductivities, it *cannot* be concluded that high strand conductivities ensure

high macroscopic conductivities. What hampers the conductivity is that even if single strands did extend the full length of the sample, the one-dimensionality of the strand would make it difficult for electrons to travel past any structural defects. Thus, conduction in polymer samples must involve at least some interchain conductivity. The overall conductivity is therefore dependant on the molecular assembly structure.

Two extreme cases of molecular assembly can be used to explain the behavior of a real sample. The first one is that of the disordered "spaghetti" like structure found in electropolymerized poly-pyrrole (Fig. 1.4A). The other is the structured assembly found in systems like regio-regular alkyl-polythiophene (RR-APT) (Fig 1.4B). The RR-APT naturally assembles into crystallites where the polymer backbones of the strands are planar and stacked in a highly regular manner. The driving force for this conformation is the alkyl-alkyl chain interaction [7]. Upon examining the conformation the optimum intra-strand  $\pi$ -conjugation and good inter-strand  $\pi$ -overlap is found. The effect of the polymer packing regularly, is that carriers do not have to rely solely on mobility along the strand, which may be obstructed by a defect, but can also move perpendicular to the strand through the inter strand  $\pi$ -band. Thus, the system resembles a highly anisotropic, two dimensional conductor. There are, however, two effects which complicate matters further: a) disorder induced by the counter ions and b) limited domain size [8]. In the domains boundaries the conduction of charge is hampered due to disorder which upsets both inter-strand  $\pi$ -overlap and intra-strand  $\pi$ -conjugation. This behavior

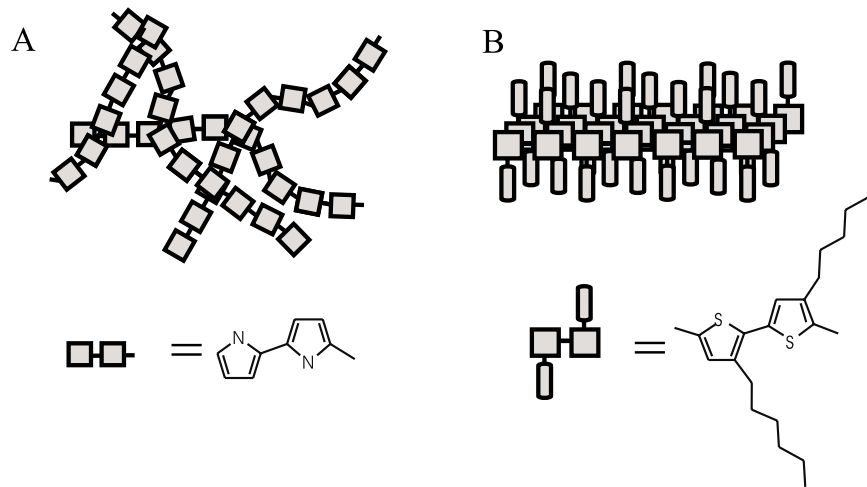


Figure 1.4: Polymer structure schematic: A) disordered "spagetti" like structure of poly-pyrrole B) Ordered 3d-structure of regio-regular polythiophene.

leads to high resistances between domain [8]. Similarly, introducing a counter ion into the close packed native structure leads to disorder in the structure and consequently to a reduction of mobility.

In poly-pyrrole, little structural change is expected from inserting the counter ion. This is, in part, because the polymer is assembled and doped at the same time, thus, yielding space for the counter ion. It is also because of the disordered "spaggetti" like structure, i.e. there was little order to disrupt in the first place. The disadvantage of this approach is that the only inter-chain interaction favoring the highly conductive planar state is  $\pi$ - $\pi$ -overlap. Thus, charge transport must rely primarily on one-dimensional conduction along the strand, because, intra-strand conduction is limited to tunneling, incidental  $\pi$ -

$\pi$ -overlap or polymerization flaws like branching. It is therefore surprising, considering the disorder of the poly-pyrrole compared to RR-APT, to find that the conductivity for the most conducting samples at room temperature of poly-pyrrole is only about an order of magnitude lower than that of RR-APT (200-400  $\text{Scm}^{-1}$  vs. 1000-1600  $\text{Scm}^{-1}$  [9]).

Furthermore, what is intriguing about the poly-pyrrole system is that samples made by low temperature synthesis do not show strong carrier freeze-out<sup>1</sup> even at temperatures as low as 10K [10]. For these reasons, the poly-pyrrole system is used extensively in this dissertation.

Now that the properties of normal state conduction have been established for the polymeric conductors, it is time to introduce the properties associated with the superconducting state.

## 1.2 Introduction to superconductivity

A superconductor is a material which below a specific temperature, known as the transition temperature ( $T_c$ ), conducts electricity with **zero resistance**. The superconducting *state* is uniquely different from that of a perfect conductor as it expels all magnetic field lines from its interior. This unusual magnetic expulsion phenomenon is known as the **Meissner effect** (see Fig. 1.5 ).

---

<sup>1</sup>Freeze-out: The lack sufficient of thermal energy to overcome the activation energy associated with charge movement.

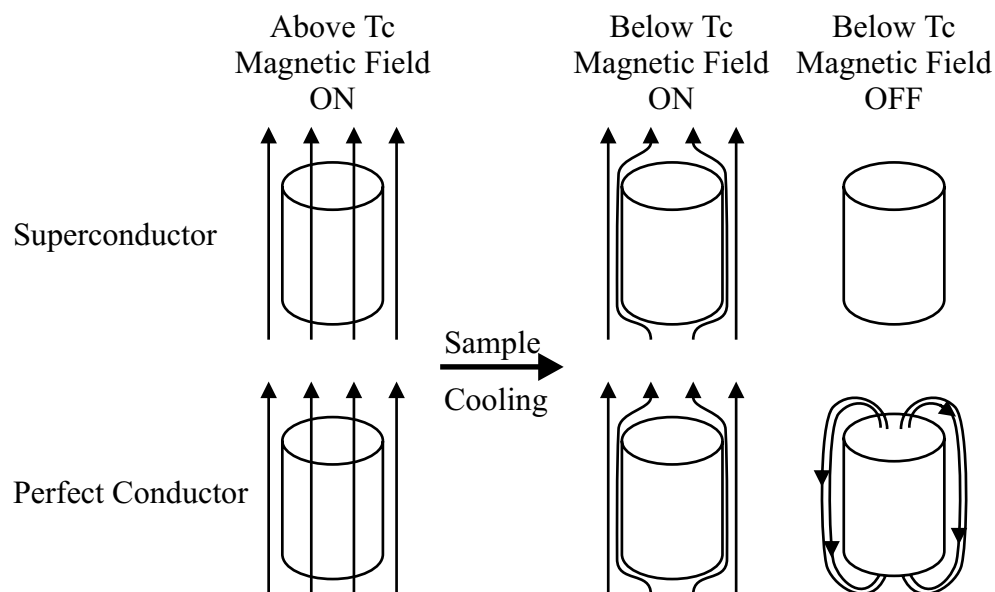


Figure 1.5: Meissner state versus perfect conductor for a field cooled sample. (Arrows indicate the magnetic field lines)

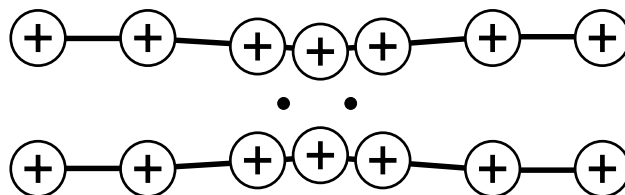


Figure 1.6: Cooper pair formation. The electron (•) distorts the lattice making a second electron follow, effectively coupling the two negative particles.



The theoretical mechanism that overcomes the effect of electron scattering, (i.e. resistance) first formulated by Bardeen, Cooper and Schriffer<sup>2</sup> (BCS theory) is based on electron pairing. Electrons are repelled by Coulomb forces due to their negative charge both in the metallic state and in vacuum. However, in the superconducting state these coulombic interactions are overcome by coupling with lattice vibrations also known as phonons (see Fig. 1.6). Thus, as one electron moves through the lattice it will slightly displace the positively charged nuclei thereby affecting the charges surrounding the electron following it. Collectively, these processes lead to the formation of **Cooper pairs**: the condensate of two electrons with opposite spin and momentum. Since the Cooper pair has a total spin of 0 it must be treated as a Boson. The Pauli exclusion principle, therefore, allows all the Cooper pairs to occupy the same state. In fact, the Cooper pairs are not isolated particles, but form a collective state in the bulk superconductor which can be described by *one* wavefunction ( $\psi$ ):

$$\psi(r) = n_c^{1/2} \exp(i\varphi(r)) \quad (1.2)$$

where  $\psi^*(r)\psi(r) = n_c$  is the concentration of Cooper pairs, and  $\varphi(r)$  is the phase at the position vector  $(x, y, z) = r$ . In normal conductors, phase coherence is only observable in systems with dimensions shorter than the electron mean free path. In the superconductor,  $\varphi$  is a macroscopic observable.

---

<sup>2</sup>See reference [11] for an introduction to BCS theory.

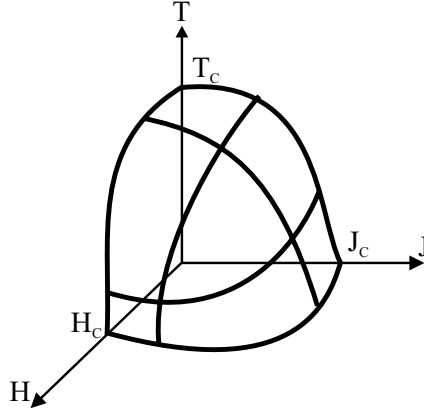


Figure 1.7: The critical surface of a superconductor. (H: Magnetic field, J: Current density, T: Temperature and Subscript c: Critical value)

How the formation of Cooper pairs and  $\varphi$  affect the electronic behavior is the subject of the next sections. Here, the phase boundaries of the superconducting state is the next topic.

Cooper pairs consist of two electrons with spin in opposite direction. Applying an external magnetic field will, therefore, tend to break up the Cooper pairs as the electrons align their spin along the field. The Cooper pairs that have broken up in response to the field do not affect the phase coherence of the superconducting phase, but they do reduce the size of the local magnetic field. Thus, the magnetic phase transition from the normal to the superconducting state is found to be gradual (i.e. a  $2^{nd}$  order transition). The field where all the Cooper pairs have become broken up is known as the critical magnetic field ( $H_c$ ). Also, since the Cooper pair has charge ( $2e$ ), the conduction of charge yields a magnetic field which limits the maximum cur-

rent density ( $J_c$ ) that can be carried by a superconductor. Combining all the critical parameters leads to the phase diagram shown (Fig. 1.7), where the superconducting state is limited by  $T_c$ ,  $H_c$  and  $J_c$ .

It is true for all superconductors that the magnetic field is expelled from the bulk by the Meissner effect. However, upon examining the surface of a superconductor, a skin layer where the magnetic field and the screening current are decaying exponentially is found. The characteristic length of the decay is known as the **London penetration depth**,  $\lambda_L$ .

Superconductors are often divided into two types. Type I has a phase diagram as described above. Type II has a second superconducting phase that allows the magnetic field to penetrate the superconductor in small normal state pockets (vortices) without general breakdown of superconductivity. Thus, the Type II class to which the high temperature superconductors belong has two critical magnetic fields:  $H_{c1}$ , which separates the true Meissner state from the mixed state, and  $H_{c2}$ , which separates the mixed state from the normal state.

The next section will deal with the practical aspect of determining the critical values  $T_c$  and  $J_c$ .

### 1.3 On the measurement of the critical curve $J$ vs. $T$

The data presented in this dissertation are at zero magnetic field (more precisely the earth background magnetic field). The data collected is, therefore, a cross-section of limiting surface i.e. a limiting line. Determination of

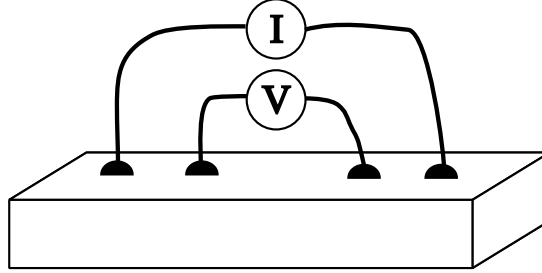


Figure 1.8: Sample for measuring current transport properties. Current ( $I$ ) is sourced and the potential difference ( $V$ ) is measured.

the limiting line is based on the fact that the superconducting state, both the Meissner and mixed state, yields zero sample resistance. Thus, by *controlling* the temperature ( $T$ ) and the current ( $I$ ) passed through the sample and *measuring* the potential difference ( $V$ ) between two points along the current path, makes it is possible to determine the boundary of the superconducting state (Fig. 1.8). Two approaches are commonly used: Constant current variable temperature also know as resistance vs. temperature<sup>3</sup> ( $R$  vs.  $T$ 's), and constant temperature variable current, also known as current vs. potential ( $IV$ 's).

Starting with the interpretation of the  $IV$  curves (Fig. 1.9A), the value of  $I_c$  is found as the highest current which yields zero potential difference. In real samples, determining  $I_c$  is complicated by rounding of the  $IV$  curve around

---

<sup>3</sup>The resistance vs. temperature is misleading as resistance implies that Ohms law applies i.e. that  $V/I$  is a constant independent of current which is only true in the normal state above  $T_c$ . The label is, however, used extensively in the superconducting literature and to be consistent, also in this text.

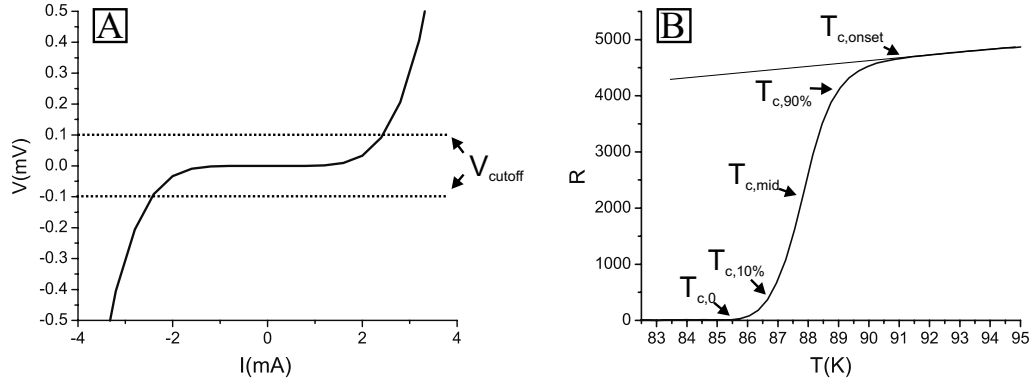


Figure 1.9: Characteristic current transport curves A) IV and B) R vs T.

$I_c$  due to either thermal effect ( $T \neq 0K$ ) or by inhomogeneous samples. The latter is often found with granular superconductors like the high temperature ones. The problem of finding  $I_c$  may be resolved by selecting a small but non-zero potential difference as the cutoff for  $I_c$ .

The R vs. T of real samples is also the source of considerable confusion. In principle,  $T_c$  is defined in the limit of  $J \rightarrow 0$  and  $H \rightarrow 0$ . However, in order to obtain a measurable potential difference in the normal state, the current must be different from zero. Transition temperatures should, therefore, be measured with the smallest possible current, which allows for the transition to zero potential difference to be measured reliably. While the current density used to gather the R vs T information seems important from a fundamental point of view, they are almost never reported in the literature. This may be because this effect is considered minor compared with the factors discussed below e.g. for a perfect sample a 5% shift in  $T_c$  would require that the current

density ( $J$ ) is 30% of the maximum 0K value.

Considering that the IV curves are rounded around  $I_c$  it should not come as a surprise that the transition from the normal state to the superconducting state in the  $R$  vs.  $T$  curve exhibit both nonzero width and rounding. For this reason, several different definitions of  $T_c$  have been devised. Some of these are depicted in Fig. 1.9B. In this dissertation, the width  $\Delta T_c$  is measured from the points where the resistance is 10% and 90% of the extrapolated normal state value. The  $T_c$  values reported here are determined from the 50% value, also known as  $T_{c,mid}$ .

Now that the important bulk properties of the superconductor have been described, it is time to move on to how the discussion of two superconductors may be coupled.

## 1.4 Coupling of superconducting states: The Josephson junction

Discussion of Josephson junctions, i.e. the coupling of two superconducting states, is included here for two reasons: a) as an introduction to the unique properties of the superconducting states and b) as a starting point for the introduction of the superconducting proximity effect.

The following description of the junction behavior is based on a combination of several representations [11–14] and emphasis is given to key principles, not to the qualitative modeling of real junctions.

Since the wave nature of the Cooper pairs have already been established (eq. 1.2), the quantum mechanical equation of motion in an isolated superconductor yields

$$-i\hbar\frac{\partial\psi(r,t)}{\partial t} = E\psi(r,t) \quad (1.3)$$

where  $r$  and  $t$  are the position vector and time respectively and  $E$  is the energy.

The next step is to couple two similar superconductors ( $S_1$  and  $S_2$ ) so that there is a *small*, but finite probability ( $K$ ) that Cooper pairs from one superconductor can travel to the other. The region of coupling is known as a superconductor **weak link**. There are several ways to attain weak links e.g. a thin insulator (I) between two superconductors (S) through which Cooper pairs can tunnel (S/I/S-junction) or a point contact where the weak link is the contact of sharp point onto a planar surface. The practical realization of weak links is a subject that will be discussed later. Here, the coupling of two superconducting states is the center of attention.

The coupling can be added as a *small* perturbation to the energy. Thus, the equation of motion of the Cooper pairs in the two superconductors becomes

$$-i\hbar\frac{\partial\psi_1(r,t)}{\partial t} = E\psi_1(r,t) + K_{21}\psi_2(r,t) \quad (1.4)$$

$$-i\hbar\frac{\partial\psi_2(r,t)}{\partial t} = E\psi_2(r,t) + K_{12}\psi_1(r,t) \quad (1.5)$$

where  $\psi_1$  is the wavefunction of superconductor 1, and  $K_{12}$  is the energy which is proportional to the probability of a Cooper pair traveling from superconductor 1 to superconductor 2.

The  $r$  and  $t$  dependence of  $\psi$  is omitted to simplify the notation. Insertion of the wavefunction, eq. 1.2, into eq. 1.4, performing the differentiation and multiplying through with  $n_{c1}^{1/2} \exp(i\varphi(r))$  yields

$$\frac{1}{2} \frac{\partial n_1}{\partial t} + i n_{c1}^{1/2} \frac{\partial \varphi_1}{\partial t} = -\frac{i}{\hbar} (E_1 n_{c1} + K_{21} n_{c1}^{1/2} n_{c2}^{1/2} e^{i(\varphi_2 - \varphi_1)}) \quad (1.6)$$

Performing the same manipulations on eq. 1.5, yields

$$\frac{1}{2} \frac{\partial n_2}{\partial t} + i n_{c2}^{1/2} \frac{\partial \varphi_2}{\partial t} = -\frac{i}{\hbar} (E_2 n_{c2} + K_{12} n_{c1}^{1/2} n_{c2}^{1/2} e^{-i(\varphi_2 - \varphi_1)}) \quad (1.7)$$

By assuming that the probability of Cooper pair transfer from  $S_1$  to  $S_2$  is the same as Cooper pair transfer from  $S_2$  to  $S_1$ , i.e.  $K = K_{12} = K_{21}$ , and by separating eq. 1.6 and eq. 1.7 into real and imaginary parts, it is found that

$$\frac{\partial n_1}{\partial t} = -\frac{\partial n_2}{\partial t} = \frac{2K}{\hbar} (n_1 n_2)^{1/2} \sin(\Delta\varphi) \quad (1.8)$$

$$\frac{\partial \varphi_1}{\partial t} = -\frac{1}{\hbar} (E_1 + K \left(\frac{n_2}{n_1}\right)^{1/2} \cos(\Delta\varphi) \quad (1.9)$$

$$\frac{\partial \varphi_2}{\partial t} = -\frac{1}{\hbar} (E_2 + K \left(\frac{n_1}{n_2}\right)^{1/2} \cos(\Delta\varphi) \quad (1.10)$$

Eq. 1.8 is known as the DC (direct current) equation as the current across the junction is given by



$$I = 2e \frac{\partial n_1}{\partial t} V = 2eV \frac{2K}{\hbar} (n_1 n_2)^{1/2} \sin(\Delta\varphi) = I_c \sin \Delta\varphi \quad (1.11)$$

where  $V$  is the volume of  $S_1$ , and  $I_c$  is the maximum current that can pass through the junction. The consequence of eq. 1.11 is that current ( $I$ ) will flow across the junction even in the absence of an external electric field if the phase difference between  $S_1$  and  $S_2$  ( $\Delta\varphi$ ) is not equal to zero. On the other hand, the presence of a potential difference ( $U = E_2 - E_1$ ) between  $S_2$  and  $S_1$  leads to an oscillating behavior as detailed below.

Subtracting eq. 1.10 from eq. 1.9 and assuming the same density of Cooper pairs ( $n$ ) on both sides of the junction (i.e.  $S_1$  and  $S_2$  are the same material) yields

$$\frac{d(\varphi_2 - \varphi_1)}{dt} = -\frac{1}{\hbar}(E_2 - E_1) \quad (1.12)$$

which after integration yields

$$\Delta\varphi(t) = \Delta\varphi(0) + \frac{2eU}{\hbar}t \quad (1.13)$$

Thus, a time varying current across the junction is expected as

$$I(t) = I_c \sin(2\pi \frac{2eU}{\hbar}t + \Delta\varphi(0)) \quad (1.14)$$

All the current-voltage (IV-curve) measurements in this dissertation are made by averaging the response of a square wave current with frequency

below 1Hz. The potential difference over the junction should, according to eq. 1.14, be on the order of  $10^{-15}\text{V}$  or smaller in order for our measurements to be affected by interference effects. This is well below our measurement capabilities, thus, only an average effect of  $U$  on  $\Delta\varphi(0)$  is measured.

Throughout this section, all effects of the magnetic field generated by the Josephson current were omitted for simplicity. This will also be the case in the following section, where the response of the phase  $\varphi$  and, thus, the Josephson current to *external* magnetic field will be discussed.

## 1.5 Josephson junctions in magnetic fields

This section is concerned with how the current ( $I$ ) of a Josephson junction is affected by an external magnetic field (Fig. 1.10). The junction is aligned in a coordinate system so that it is in the  $yz$ -plane at  $x = 0$ . The magnetic field  $B$  is applied along the  $y$ -axis.

Eq. 1.11 related the current to the phase difference ( $\Delta\varphi$ ), thus the analysis begins by analyzing how the phase difference is affected by the field. Examining Figure 1.10, the object of interest is the phase difference at  $z_0$  and  $z_4$  moving from  $S_1$  to  $S_2$ . The path 1'-2'-3'-4', 4'-4, 4-3-2-1 and 1-1' forms a closed loop and, thus,

$$\Delta\varphi(z_0) + \Delta\varphi_{1,2,3,4} - \Delta\varphi(z_1) - \Delta\varphi_{1',2',3',4'} = 0 \quad (1.15)$$

The phase difference between two points separated by the distance  $l$

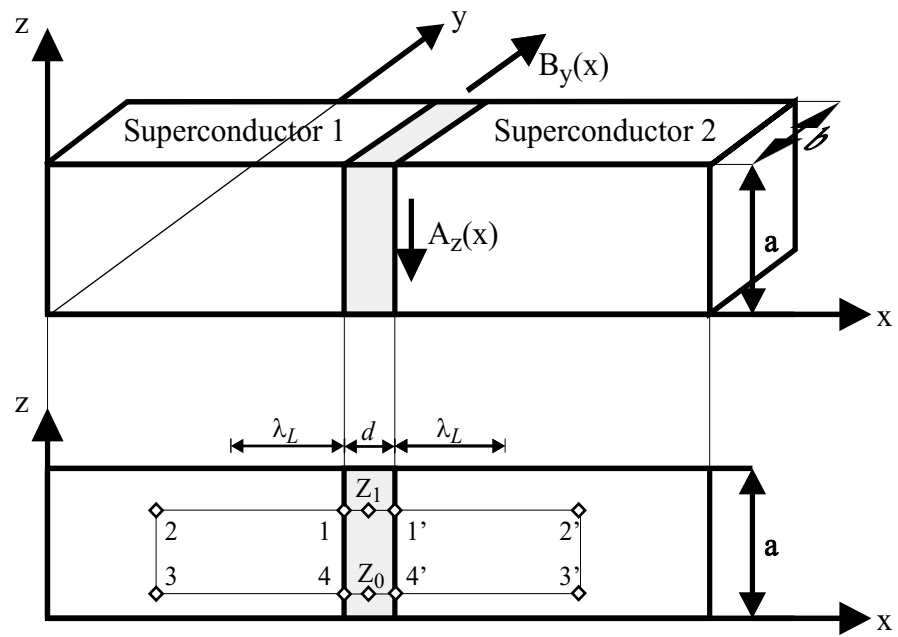


Figure 1.10: Josephson junction in magnetic field  $B$ . Top: 3d-schematic. Bottom: 2d-schematic of the same junction (Redrawn and modified from [14])

is  $\varphi = 2\pi \cdot l/\lambda$ . Thus, for the wave following the 1-2-3-4 curve, the phase difference is

$$\Delta\varphi_{1,2,3,4} = 2\pi \oint_1^4 \frac{1}{\lambda} dl = \frac{2\pi}{h} \oint_1^4 p dl \quad (1.16)$$

where de Broglie's principle  $p = h/\lambda$  was used. The momentum ( $p$ ) of a Cooper pair in a magnetic field  $B$  is

$$p = m_c v + q_c A \quad (1.17)$$

where  $m_c$  and  $q_c$  are the mass and charge of the Cooper pair, respectively, and the vector field,  $A$ , is given by

$$\text{curl } A = B \quad (1.18)$$

The magnetic field is chosen to have only a  $z$ -component so

$$A_x = 0, A_y = 0, \frac{\partial A_z}{\partial x} = B \quad (1.19)$$

will satisfy eq. 1.18.

Returning to eq. 1.15

$$\Delta\varphi(z_1) = \Delta\varphi(z_0) + \frac{2\pi}{h} \oint_1^4 (m_c v + q_c A) dl - \frac{2\pi}{h} \oint_{1'}^{4'} (m_c v + q_c A) dl \quad (1.20)$$

Figure 1.10 reveals that curve 1-4 and 1'-4' are two halves of a closed loop. The current ( $j = m_c v$ ) that passes over the junction, therefore, has no

effect on the combined integral. It is further assumed that the width of the junction ( $b$ ) is large so that the screening currents induced on the surface in the  $xz$ -plane by  $B$  are negligible compared to the bulk, thus,

$$\oint_1^4 (m_c v) dl - \oint_{1'}^{4'} (m_c v) dl = 0 \quad (1.21)$$

Combining eq. 1.20, eq. 1.19, eq. 1.21 and realizing that deep inside the superconductor  $A$  is a constant, yields

$$\Delta\varphi(z_1) = \Delta\varphi(z_0) + 2 \cdot \frac{2\pi}{h} q_c |x| B (z_1 - z_o) \quad (1.22)$$

The magnetic flux through the  $|x| (z_1 - z_o)$  area of junction is approximately given by

$$\Phi(z) = (z_1 - z_o)(d + 2\lambda_{Lo})B \quad (1.23)$$

Thus, the relation that shows a direct correlation between the phase  $\varphi$  and the imposed magnetic field has been found, as the current across the junction is given by integrating eq. 1.11 from  $z_0 = 0$  to  $z_1 = a$

$$I = I_c \int_0^a \sin(\varphi_0 + 4\pi \frac{\Phi(z)}{\Phi_0}) dz = I_c \sin \varphi_0 \frac{\sin(\pi\Phi/\Phi_0)}{\pi\Phi/\Phi_0} \quad (1.24)$$

where  $\Phi_0 = h/q_c$  and  $\Phi = a(d + 2\lambda_{Lo})B$ .

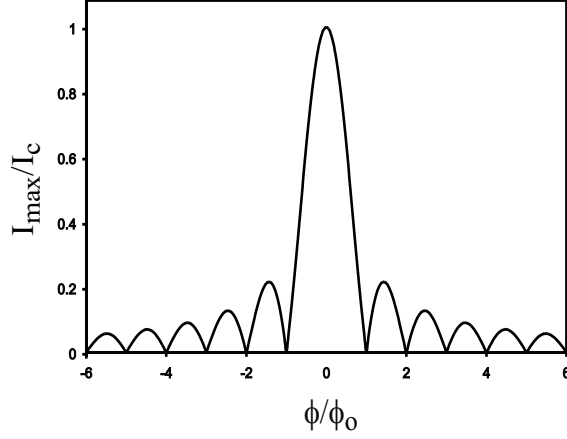


Figure 1.11: Josephson Fraunhofer pattern (normalized).

While the phase difference  $\varphi_0$  is an unknown quantity, the function  $\sin \varphi_0$  has the maximum value of one. The maximum current ( $I_{max}$ ) response relative to the magnetic field is, therefore,

$$I_{max} = I_c \left| \frac{\sin(\pi\Phi/\Phi_0)}{\pi\Phi/\Phi_0} \right| \quad (1.25)$$

The effect of imposing an external magnetic field is a current response which resembles the Fraunhofer diffraction pattern (Fig. 1.11) found when light is diffracted through a rectangular slit. The importance of this result is that the junction is ultra-sensitive to the field, e.g. a junction with just  $10\mu\text{m}^2$  area will go from  $I = I_c$  to  $I = 0$  when subjected to the earth's magnetic field ( $\sim 10^{-4}$  T). Thus, for all the samples in this dissertation the effect of the earth magnetic field can not generally be neglected. The effect can, however, be minimized by placing the plane with the largest junction area perpendicular

to the earth's magnetic field.

## 1.6 The superconducting proximity effect

The superconductor proximity effect is at the heart of the work presented in this dissertation as it is this effect that allows for introduction of superconductivity in the conductive polymer.

The proximity effect arises when a superconductor and a normal conductor which has mobile charge carriers are brought into contact with each other. The net effect is that superconducting Cooper pairs may diffuse into the normal conductor thus inducing a superconducting state therein. Further, the normal electrons may diffuse into the superconductor weakening the superconductivity there. The effect arises due to boundary conditions at the superconductor/normal conductor (S/N) interface [15]. Thus, the probability ( $F$ ) of finding a Cooper pair on the normal side is exponentially dependent on the distance ( $x$ ) from the S/N interface [15]

$$F \propto \exp(-\xi_n^{-1} |x|) \quad (1.26)$$

where the characteristic length of decay  $\xi_n$  is known as the coherence length of the normal conductor<sup>4</sup>.

Some of the classic experimental manifestations of the superconductor proximity are discussed below.

---

<sup>4</sup>eq. 1.26 is only valid when the thickness of the normal film is larger than  $\xi_n$

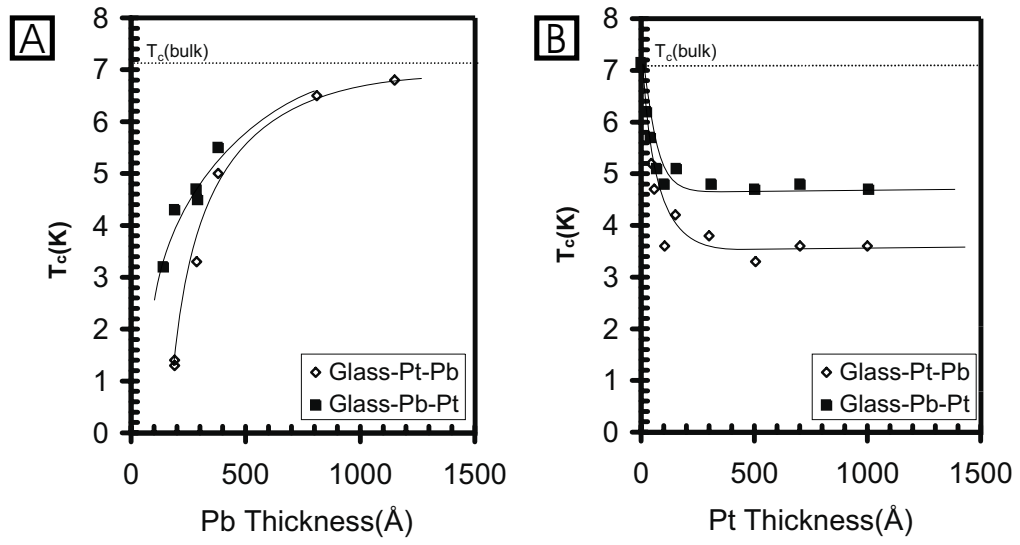


Figure 1.12: Suppression of superconductivity by proximity effect. A) Constant normal layer (Pt) thickness(1000Å). B) Constant superconductor (Pb) thickness(300Å). (Data from [16])



The effect of the proximity effect on transition temperatures of S/N sandwich thin films was studied by Werthammer *et al.* [16]. When examining the data of their study (Fig. 1.12) it is found that increasing the superconductor (Pb) thickness increases the transition temperature until it reaches the value of bulk Pb. This is expected as the proximity layer progressively constitutes less of the S-layer.

The reverse effect on  $T_c$  is witnessed as the normal layer (Pt) is extended. This is rationalized by assuming that more Cooper pairs can flow into the normal layer as it is extended, lowering the concentration in the S-layer. It is clear from the data that the proximity effect does not extend more than  $\sim 80\text{nm}$  on the S side and less than  $\sim 20\text{nm}$  on the N side.

Surprisingly, it is also found that the order in which the films are deposited has an effect on  $T_c$ . This result brings about a key point.

Suppression of the proximity effect when Pb is deposited first stems from the fact that Pb is more readily oxidized than Pt. This leads to formation of an insulating oxide layer only a couple of atomic layers thick, which is enough to affect the proximity effect greatly. The requirement of a clean interface is a constant source of complications when using high temperature superconductors because these materials are highly oxidized and react readily with common environmental agents, like moist air to form insulating phases. Thus, a major part of this dissertation research has been devoted to finding protocols and materials which yield intimate contact between the superconductor and the polymer.

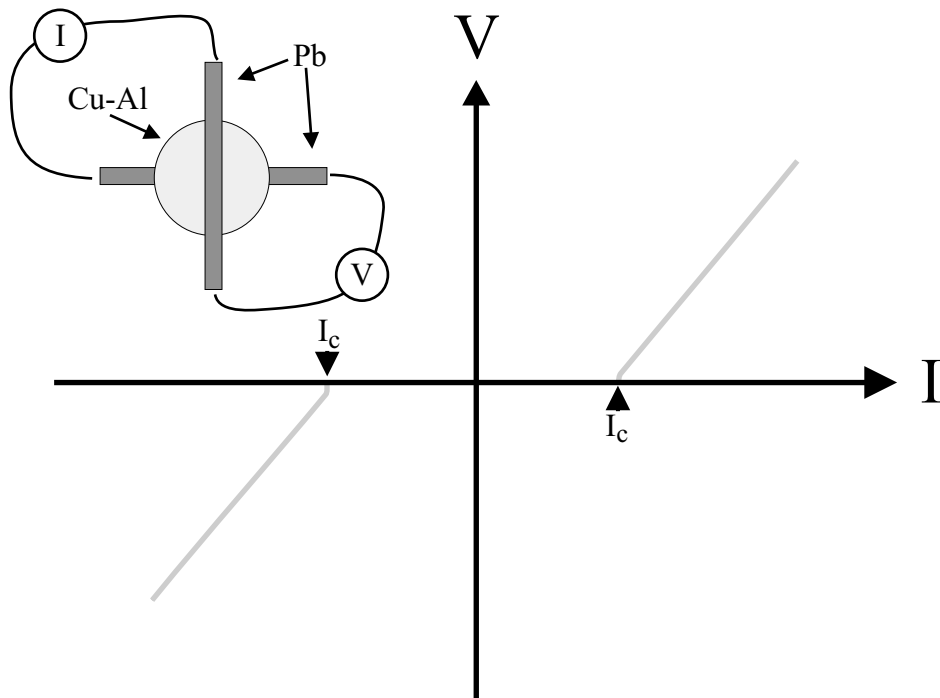


Figure 1.13: The Current-Voltage (IV) response of an S/N/S junction. Inset: Sample geometry used by Clarke [17]

To further prove that Cooper pairs truly are present in the normal layer, a S/N/S junction was assembled by Clarke [17]. The idea was to use the proximity induced Cooper pair in the normal metal as the weak link in a Josephson junction. The schematic of the key current-voltage (IV) characteristics (Fig. 1.13) shows that a supercurrent is indeed transferred between the two S electrodes (the flat part of the curve between  $I_c$ ). From Figure 1.13, it is also clear that there is a maximum current  $I_c$  as predicted by eq. 1.11. Furthermore, Clarke found that  $I_c$  was dependent on the thickness of the normal layer, the temperature and the presence of an oxide layer.

In both Clarke and Werthammer's studies the normal conductor was a metal. However, the focus of the remainder of this section will be on conductors which more closely resemble conductive polymers, i.e. the doped inorganic semiconductors.

It is the universal assumption throughout the rest of this section that Bardeen-Cooper-Schriber (BCS) theory is valid. However, this has not been conclusively proven for low-dimensional normal conductors like polymers nor for high temperature superconductors. It is, in spite of this, the best theory which is currently available and accepted for normal and superconducting metals.

The proximity effect theory by de Gennes [18] yields, in the dirty limit where the coherence length ( $\xi_n$ ) is shorter than the mean free path ( $l_n$ ), that

$$\xi_n = (\frac{\hbar}{2\pi k_B T} D)^{1/2} \quad (1.27)$$

where the carrier diffusion constant ( $D$ ) is based on a random walk assumption. Thus,  $D$  is related to the Fermi velocity ( $v_F$ ) the dimensionality of the system ( $d$ ) by

$$D = \frac{v_F \cdot l_n}{d}$$

Furthermore, if the normal conductor is a superconductor above it's transition temperature ( $T_{cn}$ ) (i.e. the material has an attractive electron paring energy), then the following expression is valid [17]

$$\xi_n = (\frac{\hbar}{2\pi k_B T} \frac{v_F \cdot l_n}{d})^{1/2} (1 - \frac{2}{\ln(T/T_{cn})})^{1/2} \quad (1.28)$$

Seto and Van Duzer used this expression to analyze the coherence length of a three-dimensional semiconductor in the framework of the free electron model [17]

$$\xi_n(T) = (\frac{\hbar^3 \mu}{6\pi k_B T e m^*})^{1/2} (3\pi n)^{1/3} (1 - \frac{2}{\ln(T/T_{cn})})^{1/2} \quad (1.29)$$

where  $m^*$  is the reduced mass,  $\mu$  is the mobility and  $n$  is the carrier density. Similarly for a two-dimensional semiconductor [19]

$$\xi_n(T) = (\frac{\hbar^3 \mu n_{sheet}}{2k_B T e m^*})^{1/2} (1 - \frac{2}{\ln(T/T_{cn})})^{1/2} \quad (1.30)$$

where  $n_{sheet}$  is the sheet carrier density.

Junctions of the S/N/S type where S is a metallic superconductor and N is an intrinsic [20] or doped semiconductor [19, 21, 22], have been analyzed in the framework of eq. 1.29 and eq. 1.30 and good agreement between experiment and theory is found.

The advantage of using semiconductors in S/N/S junctions is that it is relatively easy to control the coupling,  $K$  (eq. 1.4), by controlling the carrier density. This can be done either by extrinsic doping with impurity atoms and/or by the use of Field Effects. The latter has been exploited to make Field Effect Josephson junctions using InAs [19] and Si [22].

The subject of the proximity effect in semiconductors will return again for the special case of polymeric conductors (Chapter five), but before embarking on the final measurement, it will be necessary to see how the superconductor and the polymer are produced. The properties and fabrication methods of the copper oxide superconductors is, therefore, the subject of the next chapter.

**To summarize:** This chapter has introduced the fundamental properties of conductive polymers and superconductors. It was shown how two superconducting states may be coupled through a weak link by examples of some of the unique physical properties which arise as a result. This discussion has further led to the introduction of the proximity effect, which is central to our goal of introducing superconductivity into organic polymeric conductors.

## Chapter 2

### The Superconductor: Structure and preparation

Several classes of materials ranging from metals to complex oxides exhibit superconductivity. Of these, one class known as the copper oxide high temperature superconductors, seems to be uniquely suited for the study of polymeric proximity effects as they exhibit

- High transition temperature ( $>77\text{K}$ )
- High thresholds of oxidative breakdown

A third advantage of the class is that organic amines bind strongly to the surface, a desirable quality when making organic-inorganic composites but not a requirement. The subject of derivatizing the surface with organic molecules is discussed further in the next chapter. For now, it will be noted that organic amines provide a convenient method for binding, in an intimate way, organic conductors to high- $T_c$  superconductors.

The metallic superconductors, which are arguably simpler to process into thin film form than the ceramic high- $T_c$  ones, are not used in this dissertation because a) their low transition temperature precludes the study of

polymers which are prone to carrier freeze-out<sup>1</sup> and b) because the low oxidation potential would cause both the superconductor and polymer to oxidize when the polymer was doped. The oxidation of the superconductor renders the surface non superconducting.

While the copper-oxide superconductors are the system of choice here, they do have some features which are less desirable.

They are:

- stoichiometrically and structurally complex
- exhibit anisotropic structure
- possess reactive characteristics

To illustrate these points will require knowledge of the crystal (Section 2.1) and the electronic structures (Section 2.2) of the high- $T_c$  superconductors. The detailed knowledge of the structure will furthermore allow for an understanding of why some members of the high- $T_c$  superconductor family, which appear to be almost isostructural, have widely different corrosion characteristics (Section 2.5 experimental details are given in Section 2.4).

However, before embarking on corrosion analysis or any superconductor research in general, one must make these materials. So, Section 2.3 is

---

<sup>1</sup>Charge carriers are immobilized as the molecular vibrations which lower the activation energy of polaronic charge transport are dampened at low temperature.

devoted to fabrication of polycrystalline bulk samples and sections 2.6-2.10 to the theory, experimental details and characterization of thin films deposited by pulsed laser deposition.

## 2.1 Structure of the superconductors

All the known high- $T_c$  superconductors have one common structural feature: The presence of copper oxide sheet layers. It is believed that superconductivity takes place here and that the remainder of the structure serves as a charge reservoir that keeps the formal Cu oxidation state in the sheet at the optimal value for superconductivity.<sup>2</sup>

Throughout this dissertation, mainly two superconducting systems were used, the  $\text{R}\text{Ba}_2\text{Cu}_3\text{O}_{7-\delta}$  where  $\text{R}=\text{Y}^{3+}$  or rare earth<sup>3+</sup> and less extensively  $\text{Bi}_2\text{Sr}_2\text{Ca}_2\text{Cu}_3\text{O}_{10+\delta}$  (BSCCO-2223). The BSCCO-2223 was not used throughout in spite of the high transition temperature ( $T_c \sim 110\text{K}$ ) and enhanced corrosion stability [25] because it is hard to obtain in phase pure form, especially when thin films are needed. We, therefore, concentrated on the features of the  $\text{R}\text{Ba}_2\text{Cu}_3\text{O}_{7-\delta}$  system, which may be grown as oriented thin film samples atop a variety of insulating single crystal substrates.

The  $\text{R}\text{Ba}_2\text{Cu}_3\text{O}_{7-\delta}$  unit cell consists of a rare earth ion (R) sandwiched between Cu-O<sub>2</sub> sheets (Fig. 2.1). These sheets are surrounded by the charge

---

<sup>2</sup>The optimal *formal* oxidation state for  $\text{Y}\text{Ba}_2\text{Cu}_3\text{O}_{7-\delta}$  is +2.33. However, a more detailed analysis based on a bond valence analysis shows the oxidation state closer to +2.2. see references [23] [24]



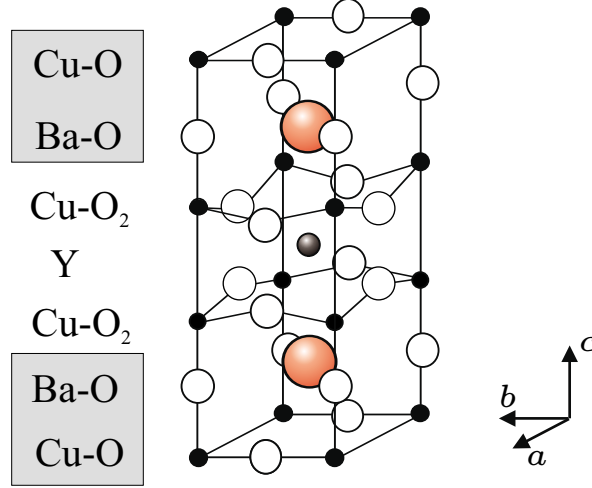


Figure 2.1: The crystal structure of  $\text{YBa}_2\text{Cu}_3\text{O}_7$ . See text for nomenclature. (Shaded area: charge reservoirs)

reservoirs which consists of the Ba-O and Cu-O chain layers. The chain layer is responsible for a number of features of strong importance for this class of materials. First, the oxygen of the chain layer are labile. Thus, it is possible to form at elevated temperatures  $\text{RBa}_2\text{Cu}_3\text{O}_6$  and the related  $\text{RBa}_2\text{Cu}_3\text{O}_{7-\delta}$  compounds where  $0 < \delta < 1$ . To overcome the problem of oxygen loss and to form  $\text{RBa}_2\text{Cu}_3\text{O}_7$  which exhibit the optimal superconducting properties, it is necessary to anneal the samples in an oxygen rich environment at temperatures around  $450^\circ\text{C}$ . Since the structure is stable over the entire range  $\delta = 1$  to 0 and the transition temperature is highly dependent on the oxygen level [23] [24], great care must be taken to ensure that the entire multigrain structure is fully oxidized. Secondly, the formation of the chain Cu-O layer (at  $\delta = 0$ ) reduces

Table 2.1: Superconducting and normal state properties of  $\text{YBa}_2\text{Cu}_3\text{O}_{7-\delta}$

along	<i>ab</i> -axis	<i>c</i> -axis	Reference
$\rho(300\text{K})$	110 $\mu\Omega$ cm	5 m $\Omega$ cm	[26]
$\frac{d\rho}{dT}$	<0	>0	[14, 26]
$\xi_{T=0}$	1.6nm	0.3nm	[14]
$\lambda_L$	160-240nm	1360-1480nm	[14]

the crystal symmetry from tetragonal to orthorhombic. Thirdly, the vacancies in the Cu-O layer forms channels, through which small molecules may enter or leave the structure (see section 2.5).

The highly anisotropic structure also affects the electronic transport properties in both the normal and superconducting states as will be described further in the next section.

## 2.2 The effect of crystal orientation on electronic properties

Transport of charge in the  $\text{RBa}_2\text{Cu}_3\text{O}_7$  samples takes place predominantly in the mixed valence CuO network. This network extends continuously (except for defects) in the *ab*-plane, but is interrupted by the oxygen deficient R layer in the *c*-axis direction. It is, therefore, expected that (Table 2.1) the normal state conductivities to be quite different in the two directions. Similarly, the superconducting properties are also affected (Table 2.1), which will have a profound effect on the theoretical discussion of the proximity effect in our samples (section 5.2).

The anisotropy of the conductive properties are important when deal-

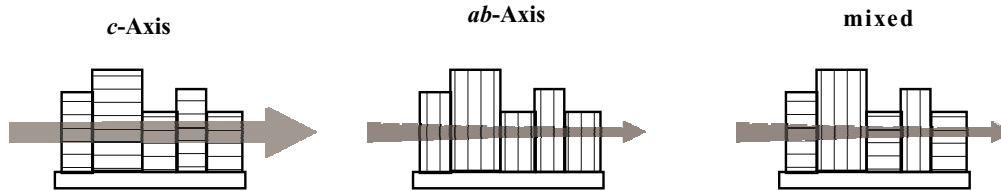


Figure 2.2: Current transport as a function of crystallographic grain orientation. Thin hatched lines illustrate the direction of the copper-oxide sheet layers and the arrows show the transport of current.

ing with multigrain thin films. By varying the deposition temperature, it is possible to grow the grains epitaxially with either the long unit cell axis ( $c$ -axis) or the short axis ( $ab$ -axis) perpendicular to the surface (Fig. 2.2). At intermediate temperatures, mixed  $c$ -axis and  $ab$ -axis films are obtained (see Section 2.10).

While the local superconductive properties resemble those obtained in single crystals, conductivity through the film requires transport between grains. In  $\text{RBa}_2\text{Cu}_3\text{O}_7$   $ab$ -axis films the conduction requires moving charge perpendicular to the  $\text{Cu-O}_2$  sheets (Fig. 2.2). This leads to weak contacts between grains and to current transport where the electrons/Cooper pair travel a meandering path of least resistance (i.e. the superconductive one). In  $\text{RBa}_2\text{Cu}_3\text{O}_7$   $c$ -axis films, however, the  $\text{Cu-O}_2$  sheets are aligned in the plane of the thin film. It is, therefore, expected that superconductive properties will resemble those of single crystals more closely than the  $ab$ -axis films.

Before any measurement can be preformed it will be necessary to syn-

thesize the superconductor specimens. This, and the corrosion stability of the superconductor phases, is the subject of the next sections.

### **2.3 Experimental: Preparation and characterization of polycrystalline bulk superconductors**

All bulk samples used in the following sections were prepared from stoichiometric quantities of  $R_2O_3$  ( $R=Y$ , La or rare earth),  $CaCO_3$ ,  $BaCO_3$  and  $CuO$  (>99% purity), which were mixed in an agate mortar and pestle with small amounts of acetone or ethanol. The samples were then heated in air in fused alumina crucibles (1<sup>st</sup> sintering) (see table 2.2 for typical heating schedule). Once the sample had cooled to room temperature it was ground in the agate mortar using acetone or ethanol, allowed to air dry and pressed into pellets of  $\sim 1$ cm diameter and 2-5mm thickness at pressures of 3-5 metric ton before next sintering. The process was repeated until satisfactory superconductive properties could be confirmed after oxygen annealing. Samples were annealed at 450°C in flowing oxygen for more than one week.

Samples used for pulsed laser deposition (PLD) targets were prepared as above, except the material was pressed into a one inch diameter 7-10mm thick disk before the final sintering, which took place closer to the melting temperature in order to increase the density of the pellet.

Sample structure was determined by powder X-ray diffraction [27], the formal oxidation state (FOS) of Cu by iodometric titration [28], and the superconductive properties by four point probe conductivity measurements (section

Table 2.2: Pellet preparation.				
REBa <sub>2</sub> Cu <sub>3</sub> O <sub>7</sub>	RE=Y	RE=Eu	RE=Nd	YCaBaLa <sup>a)</sup>
Sintering	Time(Hours)/Temp(°C)			
1	12/850	12/850	19/850	12/850
2	12/900	12/900	12/870	12/900
3	12/950	12/950	20/900	12/950
4			18/920	
5			14/950	
O <sub>2</sub> anneal	200h/400-550°C			
FOS(Cu) <sup>b)</sup>	2.22± .02	2.24± .01	2.27± .01	2.32± .04
T <sub>c,mid</sub> (K) <sup>c)</sup>	88	87	87	82
Δ T <sub>c</sub> (K)	3	6	5.5	3.5

<sup>a)</sup> Y<sub>0.6</sub>Ca<sub>0.4</sub>Ba<sub>1.6</sub>La<sub>0.4</sub>Cu<sub>3</sub>O<sub>7</sub> <sup>b)</sup> Formal Oxidation State  
<sup>c)</sup> Resistance of 50% of extrapolated normal state resistance

2.9).

## 2.4 Experimental: Measurement of superconductor corrosion stability

Ceramics prepared as described in Table 2.2 were ground to the same approximate particle size. This powder was adhered to a glass slide, by covering the slide with silicon grease and sprinkling the powder onto it. Great care was taken to prevent particles from being covered with the grease.

The samples were exposed to 75°C and 75% relative humidity in a controlled environment chamber to accelerate corrosion. Periodically, the samples were removed from the chamber and a diffractogram was gathered. The level of corrosion was then gauged by ratioing the average of diffraction peaks at

$2\theta=33^\circ$  and  $2\theta=58^\circ$  <sup>3</sup> before and after corrosion. Any variation due to beam instability was eliminated by collecting a reference diffractogram before every run.

Samples for Scanning Electron Microscopy (SEM) study were prepared by exposing a  $\frac{1}{4}$  pellet ( $\sim 0.16\text{g}$ ) to  $\sim 1.5\text{ml}$  of aerated filtered deionized water ( $\rho > 17.4\text{M}\Omega\text{cm}$ ) in a vessel that was covered, but not air tight for 1.5h. The samples were rinsed with EtOH and blown dry in a gentle stream of  $\text{N}_2$  immediately after the samples were removed from the water. No further surface treatment was performed before introduction to the SEM.

## 2.5 Corrosion mechanism and stability of $\text{RBa}_2\text{Cu}_3\text{O}_{7\pm\delta}$ phases<sup>4</sup>

The objective of this section is to identify more stable cuprate samples which would make the requirement of inert atmosphere handling of the superconductor/polymer bilayer less stringent.

In Figure 2.3, the corrosion characteristics of a series of  $\text{RBa}_2\text{Cu}_3\text{O}_7$  phases ( $\text{R}=\text{Y}, \text{Eu}, \text{Nd}$ ), are compared to the  $\text{Y}_{0.6}\text{Ca}_{0.4}\text{Ba}_{1.6}\text{La}_{0.4}\text{Cu}_3\text{O}_{7-\delta}$  phase which has been optimized for high corrosion resistance at the expense of transition temperature [29]. From the corrosion data, little effect of increasing the ionic size from  $\text{R}=\text{Y}^{3+}$  ( $1.02\text{\AA}$ ) to  $\text{R}=\text{Eu}^{3+}$  ( $1.07\text{\AA}$ ) (Fig.2.3) is wit-

---

<sup>3</sup>The  $\langle 013 \rangle, \langle 103 \rangle, \langle 110 \rangle$  and the  $\langle 116 \rangle, \langle 123 \rangle, \langle 213 \rangle$  peaks

<sup>4</sup>The work deccribed in this section was completed in collaboration with then undergraduate M. Ali.

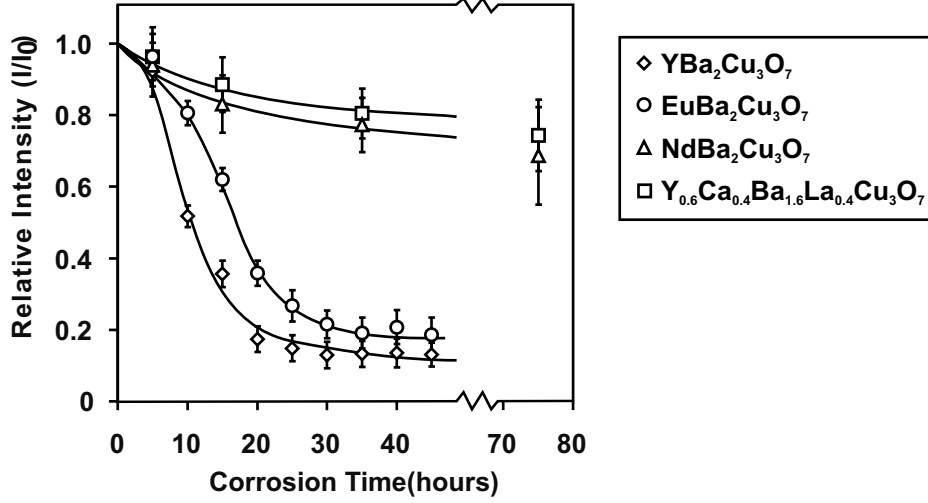
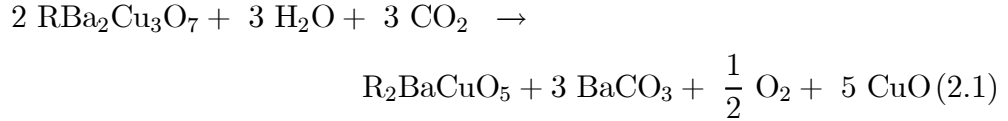


Figure 2.3: Accelerated corrosion gauged by decay of diffraction. (See table 2.2 for sample preparation details)

nessed. This is consistent with previous studies of  $R=\text{Gd}^{3+}$  ( $1.05\text{\AA}$ ) [29]. However, when  $R=\text{Nd}^{3+}$  ( $1.10\text{\AA}$ ) the corrosion stability rivals that of  $\text{Y}_{0.6}\text{Ca}_{0.4}\text{Ba}_{1.6}\text{La}_{0.4}\text{Cu}_3\text{O}_{7-\delta}$  markedly without a serious reduction of  $T_c$ . Understanding the unique behavior of the  $R=\text{Nd}^{3+}$  phase requires an understanding of the corrosion mechanisms of the  $\text{RBa}_2\text{Cu}_3\text{O}_7$  phases as well as the structural changes induced by using different R ions.

The overall corrosion reaction of the  $\text{RBa}_2\text{Cu}_3\text{O}_7$  phases



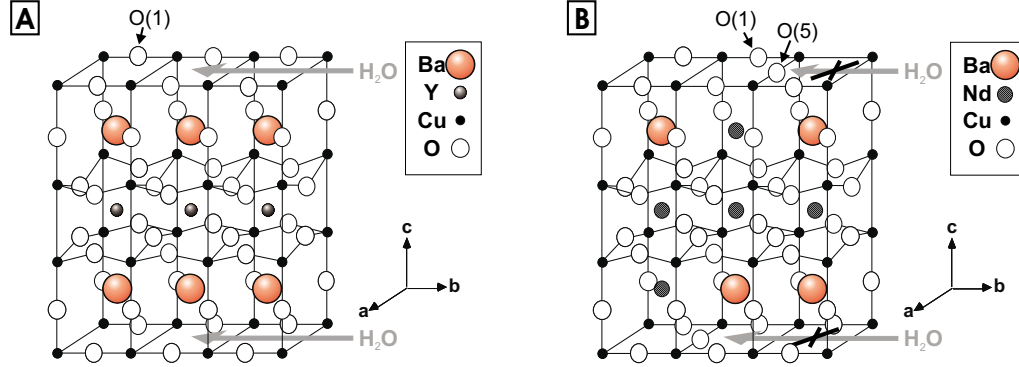
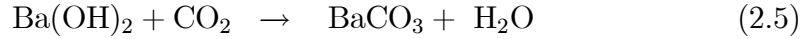
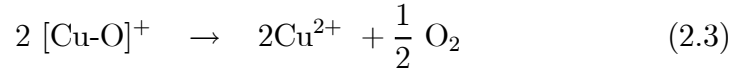


Figure 2.4: Water penetration. A) Water enters easily through the channels of vacant oxygen in  $\text{YBa}_2\text{Cu}_3\text{O}_7$ . B) In  $\text{NdBa}_2\text{Cu}_3\text{O}_7$  the channels are blocked by extra or rearranged oxygen atoms.

is believed to involve at least four steps:<sup>5</sup>



In the initial step, water enters deep into the structure through the vacancies next to the chain layer at the O(5) position (Fig. 2.4A). There, it can react with one of the chain oxygen and form  $\text{OH}^-$ . This is followed by a redox reaction where the Cu-O network is reduced and molecular oxygen

---

<sup>5</sup>reference [29] and references therein.



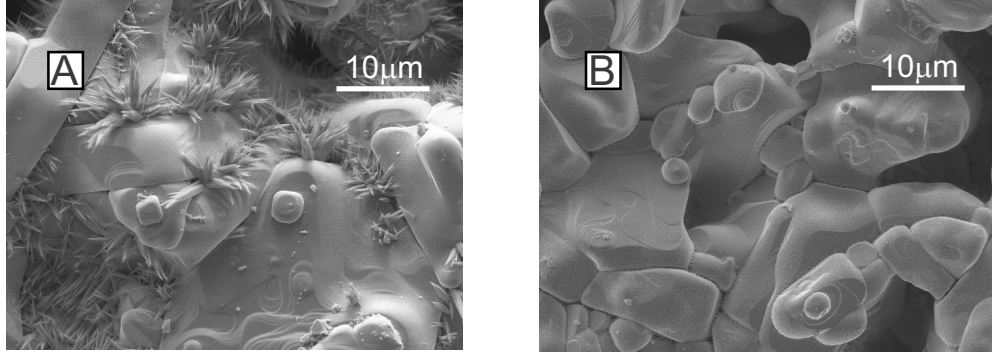


Figure 2.5: SEM micrographs of A)  $\text{YBa}_2\text{Cu}_3\text{O}_7$  and B)  $\text{NdBa}_2\text{Cu}_3\text{O}_7$  after 1.5 hours of exposure to aerated water.

is released. Then,  $\text{Ba}^{2+}$  will associate with  $\text{OH}^-$  and subsequently leach to the surface due to the high hydration energy of  $\text{Ba}^{2+}$  [29]. On the surface,  $\text{Ba}(\text{OH})_2$  reacts with  $\text{CO}_2$  and reforms water. The  $\text{Ba}(\text{CO})_3$  formed in the last step is directly observable in a Scanning Electron Microscope (SEM) image as small needle shaped crystals on the surface. The SEM micrographs (Fig. 2.5), therefore, serve as a more qualitative measure of the corrosion resistance.

One of the key parameters that have been used in the past when designing highly corrosion resistant  $\text{RBa}_2\text{Cu}_3\text{O}_7$  phases is crystal stress due to bondlength mismatch. The principle is, briefly, to calculate the optimal bondlength and compare it with the experimental bondlength. The calculation is based on the equilibrium bondlength previously deduced from simple binary compound corrected for non integer valence [30] [24]. Using this method of

analysis<sup>6</sup> the crystal stress trend is  $R=Y > Gd > Eu > Nd$ , but since there was no corrosion resistance enhancement with the earlier members of the series this does not seem to explain why  $R=Nd$  is unique. The focus is instead turned to a structural feature which  $NdBa_2Cu_3O_7$  and  $Y_{0.6}Ca_{0.4}Ba_{1.6}La_{0.4}Cu_3O_{7-\delta}$  have in common.

Since the first corrosion step is water entering the structure through the channels left open by the vacant O(5) sites, any mechanism that could close these channels would hamper corrosion considerably. In  $YBa_2Cu_3O_{7-\delta}$  substitution of 25% of the  $Ba^{2+}$  by  $La^{3+}$  seems to accomplish this as it brings about a transition from an orthorhombic to a tetragonal phase [29]. This means that the O(5) and the O(1) sites are crystallographically equivalent and that the O(5) must be, at least partially, occupied (Fig. 2.4B).

In  $NdBa_2Cu_3O_{7+\delta}$ , the substitution of  $Nd^{3+}$  into the  $Ba^{2+}$  site is naturally occurring due to the similarity of ionic radii. The level of substitution is, however, modest; less than 5% inferred from comparison of  $T_c$  values of our sample and samples of known substitution [31] and there is no evidence of a tetragonal to orthorhombic phase transition. However, closing of the water channels at these low doping levels is still possible because approximately  $\frac{1}{2}$  of the  $Nd^{3+}$  substituted into the Ba sites brings with it an extra oxygen, which locates at the vacant O(5) site (Fig. 2.4B). The water channels are further obstructed as the oxygen already present in the Cu-O layer rearranges

---

<sup>6</sup>To simplify the analysis only Ba-O and R-O bondlength were included.

to compensate the extra charge of  $\text{Nd}^{3+}$ . Combined, these two effects seem to effectively slow the penetration of water into the structure and, thus, slow corrosion. The overall scheme which hampers corrosion seems to be the same in both  $\text{NdBa}_2\text{Cu}_3\text{O}_7$  and  $\text{Y}_{0.6}\text{Ca}_{0.4}\text{Ba}_{1.6}\text{La}_{0.4}\text{Cu}_3\text{O}_{7-\delta}$ . However, the implementation has quite different effects on the superconductive properties.

The substitution of 25%  $\text{La}^{3+}$  for  $\text{Ba}^{2+}$  in  $\text{Y}_{0.6}\text{Ca}_{0.4}\text{Ba}_{1.6}\text{La}_{0.4}\text{Cu}_3\text{O}_{7-\delta}$  reduces the Copper oxidation state to 2.2 as the extra charge is not compensated by an increase in oxygen content. Co-substitution of  $\text{Ca}^{2+}$  of  $\text{Y}^{3+}$  brings the Cu oxidation state back to its optimal level, however,  $T_c$  never fully recovers to the value of the parent structure ( $T_c(\text{YBa}_2\text{Cu}_3\text{O}_{7-\delta}) \sim 92\text{K}$ ,  $T_c(\text{Y}_{0.6}\text{Ca}_{0.4}\text{Ba}_{1.6}\text{La}_{0.4}\text{Cu}_3\text{O}_{7-\delta}) \sim 82\text{K}$ ).

A similar suppression is not found in the  $\text{NdBa}_2\text{Cu}_3\text{O}_{7+\delta}$  sample ( $T_c \sim 92\text{K}$ ) as the level of substitution is much smaller and is partially compensated by a larger oxygen content. With the knowledge that the  $\text{NdBa}_2\text{Cu}_3\text{O}_7$  system is both more corrosion resistant and retains a high  $T_c$ , thin films production of this and other  $\text{RBa}_2\text{Cu}_3\text{O}_7$  systems by pulsed laser deposition will now be addressed.

## 2.6 Thin films growth by Pulsed Laser Deposition(PLD)<sup>7</sup>

The objective of this and the following section is to describe the process of thin film growth by pulsed laser deposition (PLD). In PLD, a pulsed laser is

---

<sup>7</sup>The process is also known as laser ablation

focused onto a target with the desired stoichiometry, situated inside a vacuum chamber (Fig. 2.6). When the laser energy density is above  $\sim 1\text{J}/\text{cm}^2$  and the pulses are short (10-30ns), the interaction between the laser and the target leads to formation of a plume with approximately the same overall stoichiometry as the target. This ability to duplicate the complex stoichiometry of a single source (the target) to a flux of ions, atoms, and clusters is central to PLD's popularity. Other deposition techniques, like sputtering (both AC and DC) as well as thermal evaporation, have widely different yields for different ions and the stoichiometry of the source materials must therefore be empirically adjusted. Once the plume is formed at the target it expands into the partial vacuum of the chamber. When the desired structure contains atoms that have a high vapor pressure, like the oxygen of the ceramic superconductors, then it is often necessary to deposit in a background gas of this element. Failure to do so will make the concentration too low for forming the desired structure when the plume condenses onto the heated substrate. The ability for the deposition to take place in high ( $<1\text{torr}$ ) background pressures of reactive gasses is another reason for the popularity of PLD when making ceramics. Using the right substrate and growth temperature results in thin films with large grains that are crystallographically aligned.

While the principle of PLD is simple, the practical execution of the technique is, unfortunately, not so simple. The next three sections are devoted to a discussion of each step of the process (Table 2.3). This is followed by a brief description of the setup and procedure used to make the thin films described

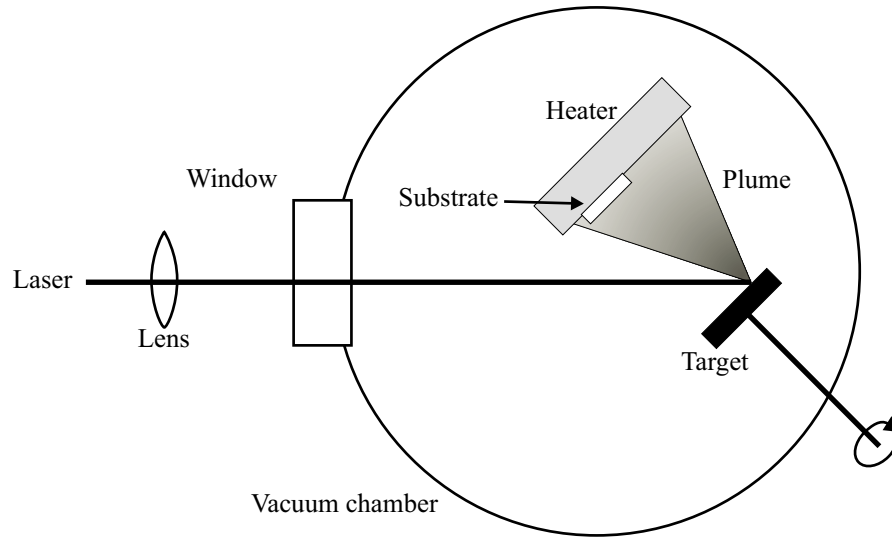


Figure 2.6: PLD schematic.

in the last section.

### Interaction between Laser and Target

The high energy laser beam is typically generated by an excimer laser reflected by a mirror for positioning and focused through a vacuum chamber view port onto the target. It is desirable to have the shortest possible penetration into the target as this yields the largest possible energy density in the ablated area. It is, therefore, common to use UV-lasers, as the extension coefficient for most materials is large in this spectral range. It is also common to use a beam profile which is non-gaussian as this profile yields the most uniform energy density over the spot area. While non-gaussian beam optics is

Table 2.3: PLD process parameters.

Parameter	Range <sup>a</sup>
Laser and focus	
Energy density	0.5-2 Jcm <sup>-2</sup>
Spot area	6-9mm <sup>2</sup>
Pulse rate	5-10Hz
Target	
Density	70-90% <sup>b</sup>
Background gas	
Pressure	100-900mtorr
Substrate	
Temperature	700-900°C
Type	SrTiO <sub>3</sub> ,MgO
$\ell(\text{T-S})^c$	5-10cm
$\ell(\text{radial-horz})^d$	0-3cm
$\ell(\text{radial-vert})^d$	0-3cm

<sup>a</sup> Value range for superconductor deposition

<sup>b</sup> of theoretical density

<sup>c</sup> Distance from perpendicular from target

<sup>d</sup>Radial distance from target spot (horizontal and vertical)

outside the scope of the dissertation, it is important to realize that the shape of the beam profile sets limitations on the focused spot, both in terms of size and energy density distribution.

Several mechanisms are involved when the beam interacts with the target, like thermal evaporation of a skin layer, electronic interaction between the electric field of the beam and the evaporated material, etc. While their discussion is well outside the scope of this dissertation<sup>8</sup>, it is important to address, in a general sense, the effect that target morphology has on the ablation process.

In the most simple model of pulse target interactions, the pulse hits the target and is absorbed in a thin surface layer. Due to the high energy density in the interaction volume, most of the material will be heated well above the evaporation temperature, regardless of composition, prior to expulsion from the surface. There is, however, a problem if the material is granular with voids<sup>9</sup> like most ceramics. The granular morphology leads to nonuniform heat transfer from the surface of the target to the bulk, as well as nonuniform heating of the surface layer. The heating and cooling profiles vs. time, therefore, vary for different grains, and with them the mechanism of mass transfer to the plume. In turn this leads to a nonuniform plume.<sup>10</sup>

The voids also cause problems as the gas they contain expands during

---

<sup>8</sup>See e.g. reference [32] for a discussion of ablation mechanisms.

<sup>9</sup>See references [33–35] for a comparison of single crystal vs. granular target.

<sup>10</sup>Nonuniform in terms of stoichiometry, and type of species i.e. ions, clusters, etc.

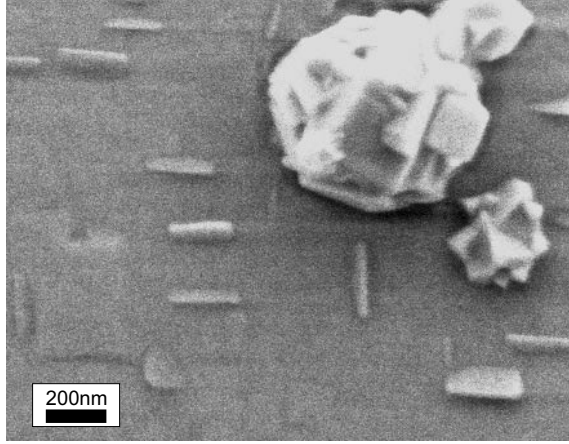


Figure 2.7: Scanning electron micrograph (SEM) of particles formed during the PLD process on top of a  $\text{NdBa}_2\text{Cu}_3\text{O}_{7-\delta}$  thin film.

ablation leading to expulsion of large pieces of material from the surface of the target.

### **Interaction between plume and background gas**

The necessity of employing a background gas consisting of the lighter structural elements brings about several adverse effects. First, even a plume, which is uniform when it leaves the target, will be scattered non-uniformly by the background gas as lighter elements change their trajectory more than heavier elements after collision with a gas molecule. Thus, the radial distribution of species is non-uniform and the radial distance from the laser spot on the target is, therefore, an important process parameter [36].

Second, reaction between the gas and the plume lead to formation of



Table 2.4: Substrate parameters.

	$a$ -axis(Å)	$b$ -axis(Å)	$\alpha(\text{ppm}\cdot\text{K}^{-1})^a$	mp( $^{\circ}\text{C}$ ) <sup>b</sup>	
YBa <sub>2</sub> Cu <sub>3</sub> O <sub>7</sub>	3.8	3.9	17	-	[14]
MgO	4.2	= $a$	14	2800	[37]p.398
SrTiO <sub>3</sub>	3.9	= $a$	11	2080	[37]p.398

<sup>a</sup> Thermal expansion coefficient <sup>b</sup> Melting point

molecular species which may condense into larger particles. This is, combined with the pieces expelled from the target, the main source of particulates on the surface of the film (Fig. 2.7).

### Condensation of the plume onto Substrate

Central to the formation of high quality thin films of ceramic superconductors is epitaxy. Thin film growth, therefore, requires a substrate stable at elevated temperatures in oxygen, with a surface unit cell axis comparable to those of the superconductor, and a comparable thermal expansion coefficient (Table 2.4). Given these requirements, our substrates of choice have been SrTiO<sub>3</sub>(100) and MgO(100) which are commercially available with highly polished surfaces. Crystal compatibility is, however, not enough to ensure epitaxy; the crystals must also be heated.

Two methods of heating are typically found in literature, contact heating where the substrate is bonded to a heated metal block and radiative heating where substrate is separated from the heat source. The heat sources are typically resistive coils or quartz lamps and the temperature is often measured by a thermocouple mounted on the heating block or on the substrate holder.

These temperatures may be 0-150°C lower than the actual temperature on the surface of the substrate. The optimal deposition temperature is furthermore dependent on the mass and energy transfer from the plume.

Given the large number of deposition parameters and their complex interdependence, it is difficult to transfer parameters from one deposition system to another. The common approach to PLD thin film fabrication is, therefore, to use values found in literature as starting points and then vary all parameters until an optimized set is found which yields thin films of the desired quality.<sup>11</sup>

## 2.7 Experimental: PLD setup

The PLD setup used to fabricate the thin films described in section 2.10 is depicted in Figure 2.8. It consists of a laser, an optical setup and a vacuum chamber (chamber hereafter). Each of these components will be described in detail below.

The laser, a Lambda Physics Complex 201, generates 248nm (KrF excimer), 100-600mJ, 25ns (FWHM) pulses at a repetitious rate of 1-10Hz. The beam shape is wedge shaped with a cross section of 24 x 6-12mm<sup>2</sup>.

The optical system consists of two high energy excimer mirrors (Newport, Irvine, CA) for directing the beam and two bi-convex (50.8mmØ, 40cm focal length) fused silica lenses for focusing. Also in the beam path to Cham-

---

<sup>11</sup>Optimization schemes, like experimental design, are only of limited help because of the large number of parameters and the non-uniform response surface.

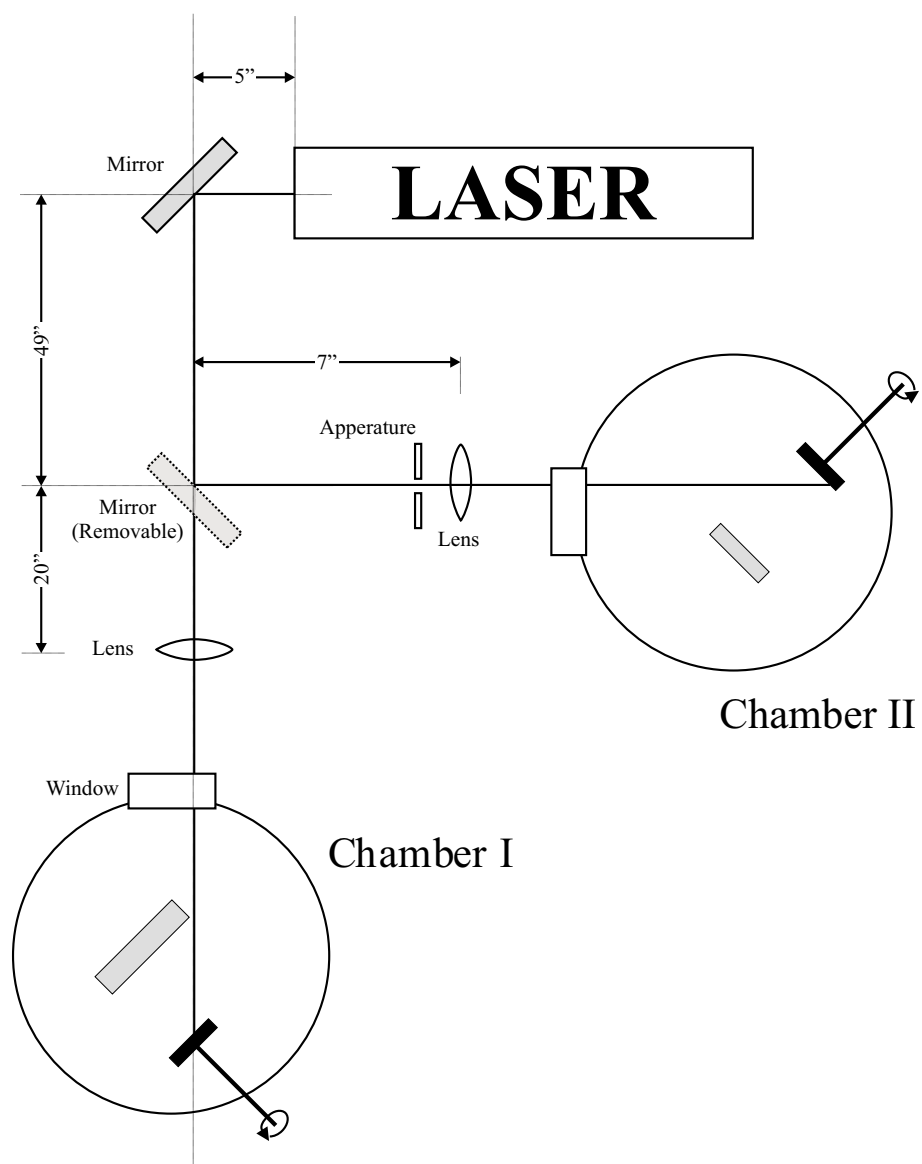


Figure 2.8: PLD deposition system setup.

ber II is a  $9 \times 26 \text{ mm}^2$  aperture, installed in an attempt to minimize diffuse radiation. Chamber windows are made from sapphire.

The chambers consist of a target rotation system, a substrate heater, a shutter, a pumping system, a gas delivery system, pressure gauges and various ports. Each chamber will be described separately since they differ widely.

The substrate heater in Chamber I is fixed on a central axis which may be rotated from outside the chamber so that samples may be loadlocked out into the adjoining glove box. A drawback of this design is that the substrate is fixed, so the target must be moved to change the target-substrate distance. This implies changing the beam path and refocusing. In practice, however, it is difficult to obtain the same focus twice and, thus, the plume characteristics change.

The substrate heater consists of a coil which radiatively heats the rotating 3" substrate holder. Temperature is measured by a thermocouple placed close to, but not in direct contact with, the substrate holder. The true surface temperature, is found by calibrating against a thermocouple spot welded to the plate surface, while the background pressure is kept identical to the deposition pressure. The advantage of using a large rotating substrate holder is that it makes it possible to deposit onto several substrates at the same time. The plume center is moved from the center of the heater so that the substrates pass the bulk of it (Fig. 2.9A). This increases the deposition rate as the density of the plume decreases rapidly with the radial distance from its center.

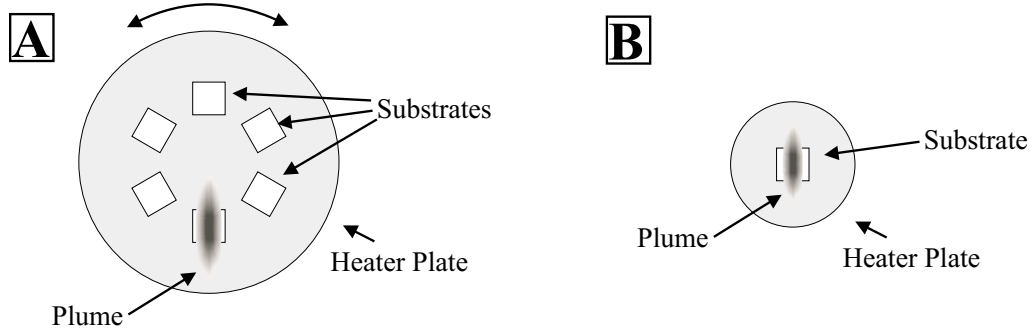


Figure 2.9: Plume cross-section on substrate holder. A) Chamber I and B) Chamber II.

The target is mounted at  $45^\circ$  relative to the incident beam on a target holder which can hold 6 targets that may be rotated in and out of the beam path without breaking vacuum. The target is rotated about its center so that the ablation track is circular.

The pumping system consists of a turbo pump backed by a diaphragm pump which allows for oil free pumping.<sup>12</sup> Pressures are measured by a convection gauge and cold cathode gauge. Finally, the system is fitted with three valves, two coarse valves for  $N_2$  (to vent the chamber) and  $O_2$  (for backfilling before cooldown), and one needle valve to control the  $O_2$  (99.993%) during deposition. The needle valve is mounted in conjunction with a rotameter to ensure that the  $O_2$  is flowing (i.e., that the pressure measured is not the background pressure).

---

<sup>12</sup>Oil backstreaming from the backing pump is a potential source of contamination.

The pumping system and the gas delivery system are similar on Chamber II, except the turbo pump is backed by an oil pump rather than a diaphragm pump and that a flow controller is mounted instead of the needle valve.

The heater of Chamber II is a one inch homemade unit, which may be placed anywhere relative to the plume. Its small size and design allow for rapid heat up and cool down, however, the substrate cannot be rotated which may lead to nonuniform thickness (Fig. 2.9A). The temperature is measured by a thermocouple spotwelded to the back of the heater plate.

The target holder on Chamber II is of a simpler design which require only one vacuum feedthrough. This means that the rotation is around the center of the multi-target holder, rather than around the center of the target as in Chamber I. The ablation track is, therefore, almost linear across the target and a smaller fraction of the surface area is therefore ablated. This is important as the number of pulses per unit area affect the amount of ablated material per pulse [36]. The deposition rate is, therefore, dependent on the ablation track geometry.

## **2.8 Experimental: PLD procedure**

The spot size was deduced from the ablated area of a piece of unexposed, but developed photopaper placed on top of the target. The energy dissipated at the target was measured with a calibrated power meter (JMax

43, Moletron, Porland, OR) after the last optical component<sup>13</sup>, and the average energy density was calculated from the spotsize and the total energy of the pulse. Substrate temperature were measured by a previously calibrated thermocouple placed in contact with (chamber II) or close to (chamber I) the heater plate.

The procedure for depositing thin films used in this dissertation did not differ significantly between the two chambers. The target (Superconductive components, Columbus, OH or home made (see section 2.3)) was sanded to expose a fresh uniform surface. Sanding debris was removed by rubbing with acetone or ethanol wetted KimWipes. Substrates were mounted on the heating plate with silver paint (Structure Probe, Inc, West Chester, PA) and allowed to dry for  $\sim 1$ h in air before mounting in the chamber. The substrate was heated to deposition temperature while the chamber was being pumped down to base pressure ( $< 5 \cdot 10^{-5}$  torr). The rate of pumping was subsequently lowered and the  $O_2$ (99.993%) process gas was introduced. To yield a uniform deposition rate the target were preablated ( $\sim 2000$  pulses (Chamber I) or  $\sim 500$  pulses (Chamber II)) with the shutter placed between target and substrate. Once the shutter had been removed the target was ablated until the desired film thickness was reached. Then, the cool down cycle was initiated and  $O_2$  pressure was increased to  $\sim 500$ torr. During the cool down of the

---

<sup>13</sup>It is important to measure the energy after the chamber window as debris often collects on the window and is burnt into the glass inspite of regular cleaning. Also it is essential to check the expected energy density BEFORE doing the measument, so that the power rating of the meter is not exceeded.

$\text{Y}_{0.4}\text{La}_{0.6}\text{Ba}_{1.6}\text{La}_{0.4}\text{Cu}_3\text{O}_7$  phase an anneal step was employed where the cooling cycle was stopped at  $\sim 400^\circ\text{C}$  for 30 min before cooling to room temperature.

## 2.9 Experimental: Characterization of thin films

X-ray diffraction was performed on either a Phillips or Bruker-Nonius D8 diffractometer using  $\text{Cu}(K_\alpha)$  radiation.

A small amount of clay is used to mount the sample on the Bruker-Nonius diffractometer, which may yield a single peak in the diffractogram.

The R vs. T curves were gathered using a current source (Keithly, model 220) and a voltmeter (Keithly, model 182). The current and voltage connections were placed at the corners of the sample. The cooling was obtained by either dipping the sample into a He dewar or by employing a closed circle cryostat. The temperature was measured using a Lakeshore 330 temperature controller.

## 2.10 On the thin films grown by PLD<sup>14</sup>

As explained in the last sections, one of the most important parameters in thin film growth is the substrate temperature. Thus, for the optimization of the deposition of  $\text{Y}_{0.4}\text{La}_{0.6}\text{Ba}_{1.6}\text{La}_{0.4}\text{Cu}_3\text{O}_7$  a set of standard parameters were used (Table 2.5), which have been shown to work well with parent compound

---

<sup>14</sup>The work presented in this section was completed in collaboration with graduate student Sungwook Kim.



Table 2.5: Deposition parameters for optimization

Laser and focus		
	Energy density	1.6 Jcm <sup>-2</sup>
	Spot area	16mm <sup>2</sup>
	Pulse rate	8Hz
	Deposition time	30min
Target (Y <sub>0.4</sub> La <sub>0.6</sub> Ba <sub>1.6</sub> La <sub>0.4</sub> Cu <sub>3</sub> O <sub>7</sub> )		
	Density	70-90% <sup>b</sup>
Background gas (O <sub>2</sub> )		
	Pressure	200mtorr
Substrate		
	Temperature	700-920°C
	Type	MgO
	$\ell$ (T-S) <sup>c</sup>	~6.5cm
Anneal		
	Temperature	450°C
	Time	30min

<sup>a</sup> Value range for superconductor deposition

<sup>b</sup> of theoretical density

<sup>c</sup> Distance perpendicular from target to substrate

YBa<sub>2</sub>Cu<sub>3</sub>O<sub>7</sub>, in conjunction with several depositions where the deposition temperature was varied systematically.

The result of this study is summarized in Figure 2.11 and Figure 2.10.

Beginning with the effect of deposition temperature on the structure, as seen in the expanded view of Figure 2.10 (Fig. 2.12), low temperatures (<780°C) favors *a*-axis growth while high temperatures (>900°C) favors *c*-axis growth. In the intermediate region, mixtures of *a*- and *c*-axis orientations are produced. It should, therefore, be possible to produce both *a*- and *c*-axis

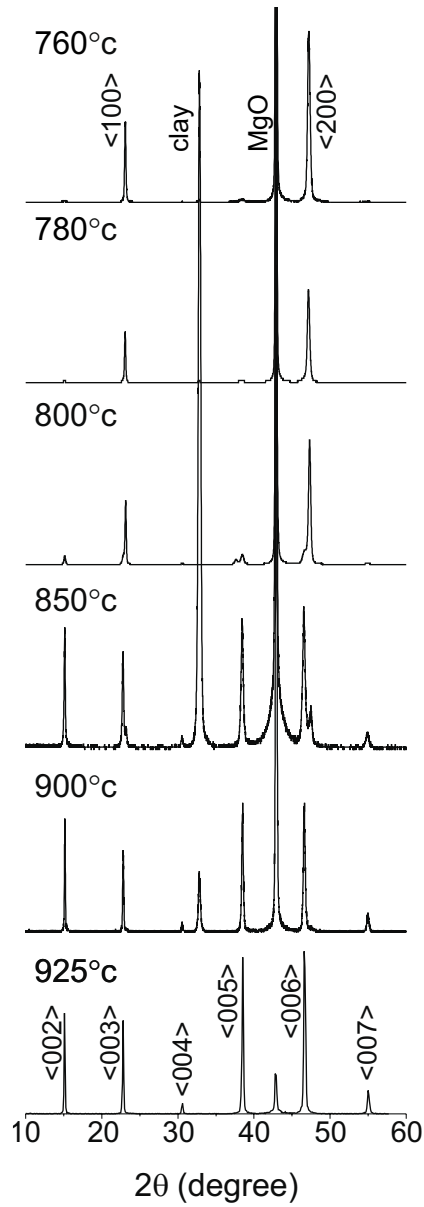


Figure 2.10: Diffraction pattern vs. setpoint temperature for  $\text{Y}_{0.4}\text{La}_{0.6}\text{Ba}_{1.6}\text{La}_{0.4}\text{Cu}_3\text{O}_7$  thin films. Note: At 935°C and 760°C only peaks associated with c-axis and a-axis film, respectively, are seen. (Peak labeled clay stems from the material used to mount the sample. See Table 2.5 for depositing details.)

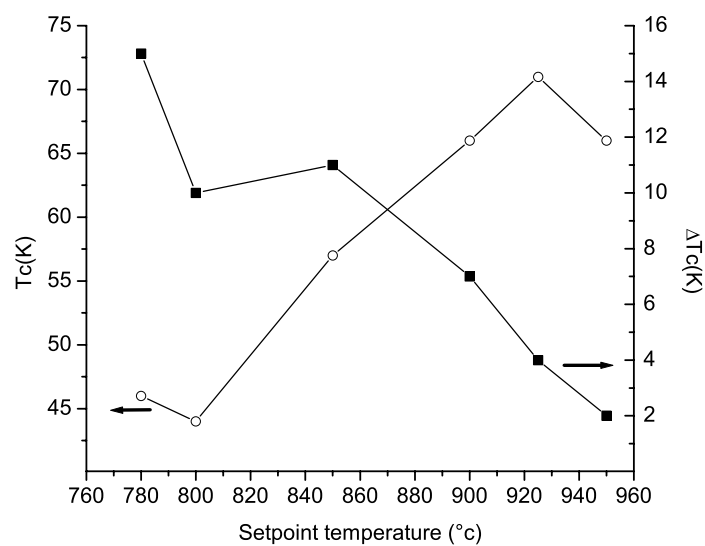


Figure 2.11: Transition temperature and width vs. substrate temperature. (The true calibrated plate surface temperature is  $200 \pm 10^\circ\text{C}$  lower than shown above.)

films at will. However, deposition temperature also effects the superconductor properties (Fig. 2.11). The general trend observed here is that an increase in temperature yields higher transition temperatures and smaller transition widths. This is to be expected as the higher substrate temperature yields higher mobility of the atoms on the surface which, in turn, should lower the amount of structural defects.

From Figure 2.11 and Figure 2.12 it is clear that *a*-axis films and high transition temperatures are mutually exclusive using the normal deposition protocol. This problem, however, had to be overcome as the use of an *a*-axis thin film would improve the prospects of successfully measuring the proximity effect (Section 5.2). Our solution was to deposit a thin template layer at low temperatures before the bulk of the film is grown at higher temperatures. The rationale behind this approach is briefly: Any crystal growth is dependent on energy of nucleation and this energy may be lowered selectively for crystal orientations that exhibit epitaxy with the surface. Thus, if the substrate was modified to yield a surface which was epitaxial to the *a*-axis orientation then *a*-axis growth may prevail even at temperatures which would otherwise support *c*-axis growth. This effect is amplified as growth along the *ab*-plane is faster than along the *c*-axis [38].

To show that the concept of orientation change by seed layer modification works in practice, a number of thin films were produced by first depositing a thin layer (500Å) at a temperature which favors *a*-axis growth followed by a

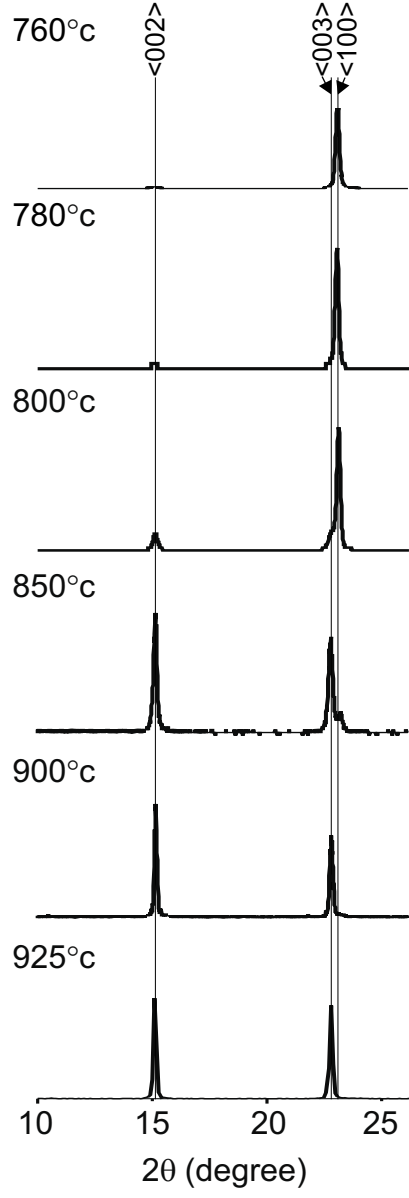


Figure 2.12: Expanded view of diffraction pattern vs. set-point temperature for  $\text{Y}_{0.4}\text{La}_{0.6}\text{Ba}_{1.6}\text{La}_{0.4}\text{Cu}_3\text{O}_7$  thin films prepared by PLD.

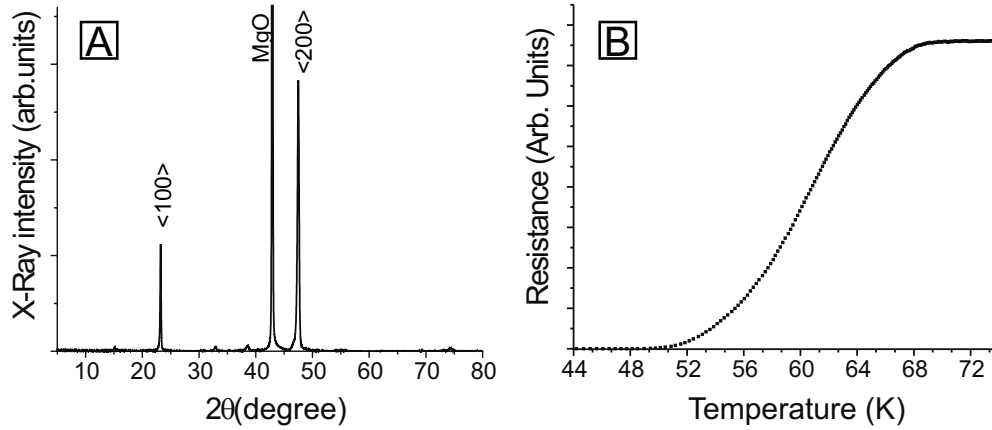


Figure 2.13: A sample of  $a$ -axis oriented  $\text{Y}_{0.4}\text{La}_{0.6}\text{Ba}_{1.6}\text{La}_{0.4}\text{Cu}_3\text{O}_7$  film deposited with a  $\sim 500\text{\AA}$  seed layer. (Total thickness  $2000\text{\AA}$ , substrate temperature, 780, see table 2.5 for other deposition details.)

second deposition at a temperature which favors  $c$ -axis growth. From Figure 2.13 it is clear that the double layer film a) is predominately  $a$ -axis oriented and b) have superconductor properties which are greatly improved compared to the single layer  $a$ -axis deposition. This type of film will be used extensively in Chapter five.

The  $\text{NdBa}_2\text{Cu}_3\text{O}_7$  thin films are interesting as they combine high transition temperature with high corrosion resistance. However, optimizing  $\text{NdBa}_2\text{Cu}_3\text{O}_7$  film deposition has proven difficult in our PLD setup<sup>15</sup> as the superconductive properties vary greatly from batch to batch, or even within batches. This makes it difficult to find a trend, which is a prerequisite for

<sup>15</sup>There are several accounts in the literature of  $\text{NdBa}_2\text{Cu}_3\text{O}_7$  thin films produced by PLD (see reference [34,35]). All, however, use a fixed substrate on a fixed heater.

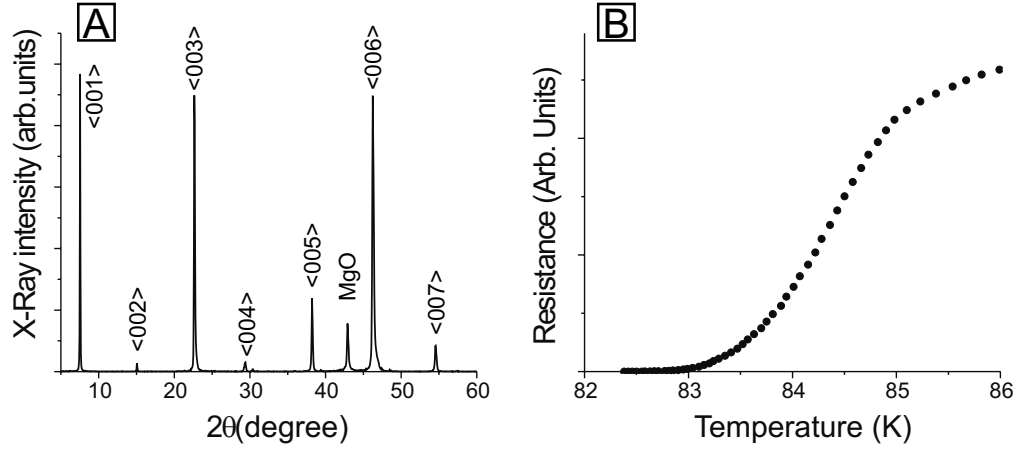


Figure 2.14:  $\text{NdBa}_2\text{Cu}_3\text{O}_7$  film. A) XRD and B) R vs. T (Deposition parameters: MgO substrate radiatively heated to  $\sim 910^\circ\text{C}$ . 3000 pulses of  $0.6 \text{ J/cm}^2$  at 5Hz.  $P(\text{O}_2)=800\text{mtorr}$ , Target-Substrated dist.:5cm )

optimization. Shown here (Fig. 2.14), however, are the characteristics and deposition parameters which may serve as starting points for further optimization once the source of the erratic behavior has been found. While the superconductive properties of these films were less than optimal the bulk structure does not seem to suffer as witnessed by XRD, these films were, therefore, used as substrate for the polymer/superconductor studies of Chapter four.

**To summarize:** This chapter described the practical aspects of working with high temperature superconductor, from bulk synthesis to thin film growth by PLD. Moreover, the corrosion properties of the  $\text{R}\text{Ba}_2\text{Cu}_3\text{O}_{7\pm\delta}$  series were systematically investigated and discussed. Now that the S part of the S/N proximity effect sample has been discussed, the next step will be to modify the surface, which is the subject the next chapter.

## Chapter 3

### Self-assembled monolayers (SAM) on copper oxide superconductors

Self-assembled monolayers<sup>1</sup> (SAMs) offer a simple way to combine the inorganic material properties of conductors [41], semiconductors [39] and superconductors [42] with the design flexibility offered by standard synthetic transformations of organic molecules to form composite structures and control interfaces. The SAM system typically consists of an organic molecule which exhibits *no* strong affinity towards the surface less one functionality. In the well known Au-SAM system, this functionality is a thiol or disulfide, in the high- $T_c$  superconductor system it is an amine. Forming the SAM on the oxide superconductor requires only exposure to a solution of the amine for 12-24h at ambient temperature. One advantage of ambient temperature processing is that the oxygen of the high- $T_c$  superconductor is not labile at these temperatures, there is, therefore, no risk of rendering the surface non-superconducting due to oxygen loss. Likewise, this new "soft chemistry" methodology provides a ideal and simple way to control the interface chemistry of high- $T_c$  systems.

Before continuing with the details of the monolayers derivatized su-

---

<sup>1</sup>For a general introduction to SAMs see references [39] and [40].



superconductor surfaces it must be made clear what is meant by a SAM as this term has become almost synonymous with *any* chemisorbed monolayer in recent literature. For the purpose here, the term SAM is associated with a *chemisorbed two dimensionally ordered monolayer with attractive lateral interactions*. Thus, some of the monolayers described in this section should not be considered SAMs as there is no indication that the molecules are ordered in a structural motif over large areas.

This chapter begins with a description of the experimental methods used to characterize the monolayers, which is followed by a Section on the synthesis of the adsorbate molecules used in this research. Chemical evidence for the adsorbed monolayer is discussed in section 3.3 and the structure of a true SAM atop a single crystal surface of  $\text{YBa}_2\text{Cu}_3\text{O}_7$  is presented in Section 3.4.

### **3.1 Experimental: Fabrication and characterization of monolayer modified superconductor surfaces**

#### **Monolayer adsorption**

The copper-oxide superconductor was exposed to a 1-5mM solution of the amine functionalized molecule dissolved in an aprotic solvent (hexanes or acetonitrile). After 12-24 h, it was removed from solution, rinsed thoroughly with pure solvent, and dried in a gentle stream of  $\text{N}_2$ . Monolayer formation was normally carried out on the bench top<sup>2</sup>.

---

<sup>2</sup>The use of dried solvents, freshly prepared superconductor surfaces and manipulation inside a  $\text{N}_2$  glove box often yields higher surface coverage more reproducibly.

## Electrochemistry

All electrochemical data was gathered using a three electrode PAR 273 (Treton, NJ) or CHI660A (CH Instruments, Austin, TX) potentiostat. Unless otherwise stated, all electrochemical measurements were performed in a N<sub>2</sub> atmosphere ( $P_{O_2} < 10\text{ppm}$ ) of a glove box (MB-150, M. Braun Inertgassysteme GmbH, Garching, Germany) fitted with a fuel-cell oxygen sensor (Teledyne analytical instruments, City of Industry, CA). The counter electrode (Pt-wire) was cleaned by scraping with a razor-blade<sup>3</sup> and activated by cycling in concentrated H<sub>2</sub>SO<sub>4</sub>. The quasi-reference electrode (Ag/Ag<sub>x</sub>O) was prepared by scraping the Ag wire with a razor blade until clean. Oxidation of the surface was done by either leaving the electrode in ambient air overnight or by exposing the wire to a 30% H<sub>2</sub>O<sub>2</sub>/H<sub>2</sub>O solution for 3-5 min. (Caution: The reaction with H<sub>2</sub>O<sub>2</sub> may become violent if prolonged, also H<sub>2</sub>O<sub>2</sub> is a strong oxidant and should be disposed of accordingly). The counter and reference electrodes were rinsed extensively with filtered deionized water ( $\rho > 17.4\text{ M}\Omega\cdot\text{cm}$ ) and allowed to dry in ambient air before introduction to the glove box. All experiments were conducted in 0.1M tetraethylammonium tetrafluoroborate acetonitrile solutions unless otherwise noted. The supporting electrolyte (Aldrich, Milwaukee, WI) was recrystallized from boiling EtOH/ethylacetate and dried under vacuum either overnight at room temperature, or for three days at 60-80°C depending on the level of dryness required. The acetonitrile (Burdick and Jackson, Mushegon, MI) was used without further purification.

---

<sup>3</sup>Sanding the wire leaves deep groves which makes subsequent cleaning difficult.

The superconductor working electrodes, typically thin films, were rinsed with acetonitrile inside the box. Contacts were made with a copper alligator clip<sup>4</sup>.

### **Atomically Resolved Atomic Force Microscopy (AFM)**

The  $\text{YBa}_2\text{Cu}_3\text{O}_7$  single crystal<sup>5</sup> was mounted between two wires with silver epoxy(epotek, Billerica, MA)<sup>6</sup>. Excess epoxy was removed with a file once the epoxy had fully cured. The crystal was then cleaved by applying force perpendicular to the wire-crystal sandwich and immediately exposed to a 1mM  $\text{CF}_3(\text{CF}_2)_3(\text{CH}_2)_{11}\text{NH}_2$ /hexane solution. Subsequent sample handling was preformed according to the protocol described above. The sample was mounted and transferred to AFM (NanoscopeIIIa, Digital Instruments, Santa Babara, CA) once the monolayer protocol had been completed.

A key parameter when doing atomically resolved AFM is a good quality tip with a force constant that allows it to stay in contact with the surface without indenting. For these experiments, silicon nitride tips (Model NP, 0.12N/m, Digital Instruments, Santa Barbara, CA) and scan rates 300-750  $\text{nmS}^{-1}$  were employed. The z-axis feedback loop of the AFM is minimized so that the sample is kept at constant height while the deflection signal is monitored.

---

<sup>4</sup>Great care must be exerted so as not to wet the film contact.

<sup>5</sup>The crystals for this study were facilitated by Koki Mochizuki and Prof. John Markert.

<sup>6</sup>This technique is similar to those developed by de Lozanne and co-worker.

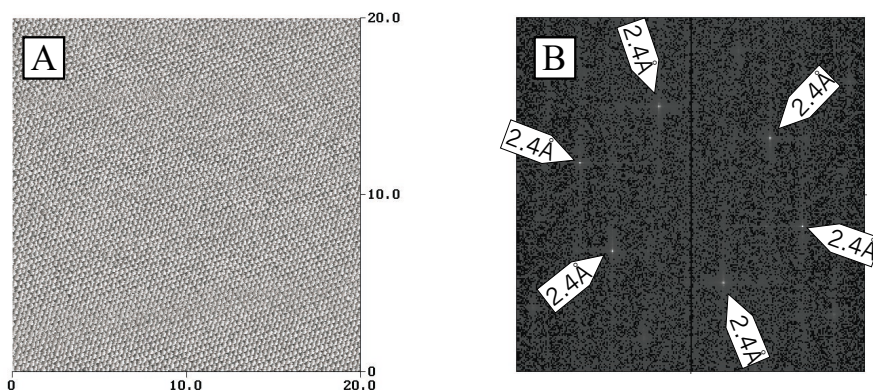


Figure 3.1: AFM of HOPG reference. A) Direct image. B) Fourier transform

Prior to introducing the sample, the quality of the tip was tested by gathering an image of freshly cleaved, highly ordered pyrolytic graphite (HOPG) (Fig. 3.1A) in deflection mode. It is imperative to check that the repeat unit is not affected by changing the scan direction, the speed, or scan size, since noise often resembles a repetitious unit. Also, a two-dimensional fast Fourier transform of the direct image will yield peaks which should be in accordance with the expected unit cell of the reference (Fig. 3.1B)

The  $\text{YBa}_2\text{Cu}_3\text{O}_7$  single crystal superconductor SAM was scanned using the same parameters as the HOPG reference.

### 3.2 Experimental: Synthesis of molecules for surface modification

#### 1-(3-aminopropyl)-pyrrole

(Under  $\text{N}_2$ , in dried glassware using ether distilled from Na/benzophenone)

To a vigorously stirred suspension of  $\text{LiAlH}_4$  in 100ml ether was added drop wise 4.9 g 2-cyanoethylpyrrole (Aldric, Milwaukee, WI) dissolved in 25ml ether. Then 100ml of moist ether was added followed by drop wise addition of 50ml of water. The ether phase was decanted off, washed with brine and evaporated until dryness. Purified by distillation (bp. 45-50°C at 0.1-0.5mmHg). Clear nonviscous oil. Yield: 1.80g (35%)

$^1\text{H}$ -NMR in  $\text{DCCl}_3$  ( $\delta$  vs. TMS)<sup>7</sup>: 1.01 ppm (wide s, 2H, amino), 1.86 ppm (p, 2H, propyl), 2.67 ppm (t, 2H, propyl), 3.94 ppm (t, 2H, propyl), 6.13 ppm (t, 2H, pyrrole), 6.65 ppm (t, 2H, pyrrole). The spectrum showed no other peak from 0 to 10ppm except for one at 7.24 which was assigned to  $\text{CHCl}_3$ .

### **2-aminoethyl-Ferrocene**<sup>8</sup>

(WARNING: Potassium Cyanide is highly toxic but is easily decomposed by *exothermic* reaction with bleach)

Under  $\text{N}_2$  atmosphere,

To a slurry of 20g KCN in 86ml of water was added 20g Ferrocenylmethyltrimethylammonium Iodide (Strem, Newburyport, MA). The solution was then refluxed for 2h during which a red oil formed and separated from the aqueous phase. Once the solution had cooled to room temperature, it was

---

<sup>7</sup>Notation: Center frequency [multiplicity (s)inglet, (d)uplet ect., integration, assignment]

<sup>8</sup>From reference [43] with alterations. Hydrogenation done in collaboration with Suzanne Tobey.

extracted several times with ether yielding a total volume of 250ml. The ether was then dried over  $\text{Na}_2\text{CO}_3$  before evaporation to dryness. Recrystallized from 375ml of hot Hexanes. Yield: 8.3g. The cyanomethylferrocene was not characterized further as it tarnishes readily in air.

A solution of 3g of the cyanomethylferrocene was dissolved in 175ml of  $\text{NH}_3$  saturated EtOH. To this solution was added 3ml RaneyNickel suspension (Aldric, Poresize  $\sim 50\mu\text{m}$ , Surface Area  $80\text{-}100\text{m}^2/\text{g}$  50% water slurry  $\text{pH}>9$ ). The solution was then placed in a high pressure reaction vessel which was subsequently evacuated, backfilled with Ar and evacuated again before it was filled with 250 psi of  $\text{H}_2$ . The solution was removed after 2h of stirring and filtered through zeolite to remove the catalyst before the filtered solution was evaporated to dryness. (WARNING: The catalyst will ignite if it is allowed to dry completely. It may be disposed of by dissolving in a 10% HCl solution). Purified by Kugelrohr distillation (bp.  $81\text{-}91^\circ\text{C}$  at  $\sim 10\text{mtorr}$ ) Dark red oil. Yield 2.71g (90%, Cyanomethylferrocene as limiting reactant).

$^1\text{H}$ -NMR in  $\text{DCCl}_3$  ( $\delta$  vs TMS): 1.22 ppm (wide s, 2H, amino), 2.47ppm (t, 2H, ethyl) 2.80 (t, 2H ethyl), 4.06 ppm (t, 2H, ferrocene), 4.07 ppm (t, 2H, ferrocene), 4.10 ppm (s, 5H, ferrocene).

### **3.3 On the chemical evidence for an adsorbed monolayer**

This section deals with the chemical analysis of monolayer modified surfaces of  $\text{YBa}_2\text{Cu}_3\text{O}_{7-\delta}$ .

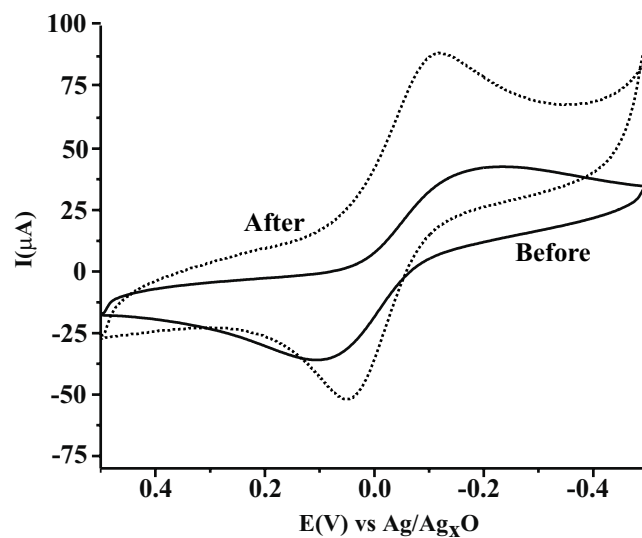


Figure 3.2: Cyclicvoltammetry probing the removal of the corrosion layer by 1min  $\text{Br}_2/\text{EtOH}$  etch from a  $\text{YBa}_2\text{Cu}_3\text{O}_7$  sample. 1<sup>st</sup> Oxidation and reduction wave of TCNQ in dry acetonitrile containing  $\sim 0.1\text{M}$   $\text{Et}_4\text{NBF}_4$ . Note the increase in peak current as well as the reduction in peak splitting after the etch. ( $\text{YBa}_2\text{Cu}_3\text{O}_7$  epoxy encapsulated electrode, geometric area and concentrations are unaltered from the before to the after scan) Data collected by then undergraduate B. Pallohusky.

As described in Section 2.5, surfaces of  $\text{YBa}_2\text{Cu}_3\text{O}_{7-\delta}$  are prone to corrosion and *all* the corrosion products are insulating leaving the surfaces unfit for proximity effect experiments. Several protocols have been developed to etch away the corrosion productions, like  $\text{Br}_2$  in EtOH [44]. Thus, in initial attempts to yield reproducible superconductive surfaces, the  $\text{Br}_2/\text{EtOH}$  etch treatment was applied to a number of epoxy encapsulated superconductor electrodes. As shown by the reduction of peak splitting in Figure 3.2, the  $\text{Br}_2/\text{EtOH}$  (1min etch) does remove the corrosion products. However, it has not been possible for us to develop a  $\text{Br}_2/\text{EtOH}$  etch protocol which can reduce the peak splitting to the theoretical limit of 59mV/n. This situation illustrates a typical dilemma of chemical compatibility when working with copper-oxide superconductor surfaces. The use of EtOH is necessary as the metal bromides formed during the etch must be soluble, but EtOH is hydrophilic so that it is likely that the surface is exposed to water during the final rinse. The use of a glove box would make it possible to handle the solvent and superconductor without exposing it to moisture, but this is precluded by the detrimental effect  $\text{Br}_2$  would have on the oxygen scrubber of the box. The experiments that led to Figure 3.2 were, therefore, conducted in a  $\text{N}_2$  filled glove bag, which, as the data shows, is a less than perfect solution. A more elegant solution was therefore sought.

It has previously been shown that when forming an alkyl amine monolayer on the surface of the superconductor the corrosion products initially present on the surface are dissolved before the surface is passivated by the



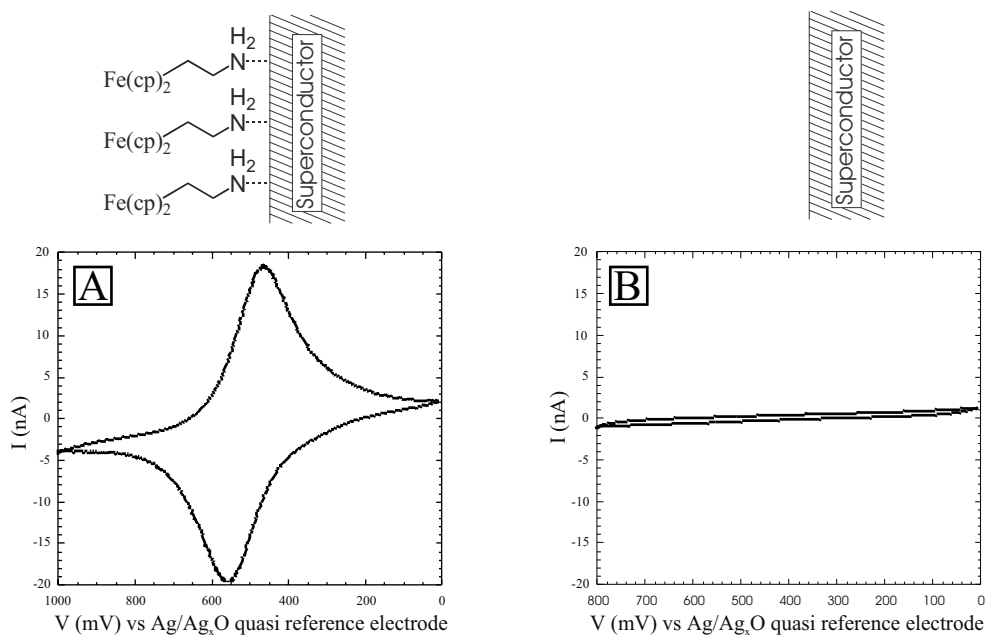


Figure 3.3: Cyclic voltammograms of A) 2-aminoethylferrocene localized atop a  $\text{YBa}_2\text{Cu}_3\text{O}_{7-\delta}$  thin film along with B) bare film of the same superconductor. (Supporting electrolyte  $0.1\text{M Et}_4\text{N}^+\text{BF}_4^-$  in acetonitrile, Scan Rate  $75\text{mV}\cdot\text{s}^{-1}$ ).

monolayer [45]. However, before amine monolayer can be employed in proximity effect research it must be shown that there is good electrical contact between the monolayer and the underlying superconductor. To this end a ferrocene tethered to a short chain amine was synthesized (2-aminoethyl-Ferrocene, Section 3.2), and the electrochemical response of a monolayer atop the superconductor was measured (Fig. 3.3).

The comparison between electrochemical response of the monolayer modified and the untreated superconductor thin film shows that a) no faradaic

electrochemical response is present from the untreated superconductor (Fig. 3.3B) and b) both oxidative and reductive waves of the ferrocene are present in the response of the monolayer derivatized film (Fig. 3.3A). These results suggest that the surface of the superconductor is not rendered insulating by monolayer formation. Furthermore, the electrochemistry shows that electrons may be passed easily between the adsorbed monolayer and the superconductor, which is a prerequisite if adsorbed polymer layers are to exhibit proximity effect from the underlying superconductor.

Previous studies have shown that samples treated like the superconductor in Fig. 3.3B exhibit little or no oxidation or reduction when exposed to ferrocene in solution, i.e. the corrosion layer obstructs electron transfer [46]. Thus, while the response of the untreated film resembles that of normal double layer capacitance, the origin of this voltammetry may be more complicated.

Since there is no mass transfer of electroactive species to and from the surface when the electroactive species are adsorbed, the peak current ( $I_p$ ) shows a different dependence on the scan rate ( $v$ ) compared to solution species [47]. Figure 3.4 shows an attempt at correlating the scan rate with the two extreme cases of irreversibly adsorbed ( $I_p \propto v$ ) and completely dissolved/diffusion limited electroactive species ( $I_p \propto v^{\frac{1}{2}}$ ). Here, the  $I_p \propto v$  yields the best fit of the two models. A similar analysis of  $I_p$  dependence on  $v$  have previously been carried using secondary and tertiary amines and longer tether ( $(\text{CH}_2)_6$ ) between the ferrocene and the amine [42]. In both cases a similar conclusion is derived: The amine is surface bound when examined on the time

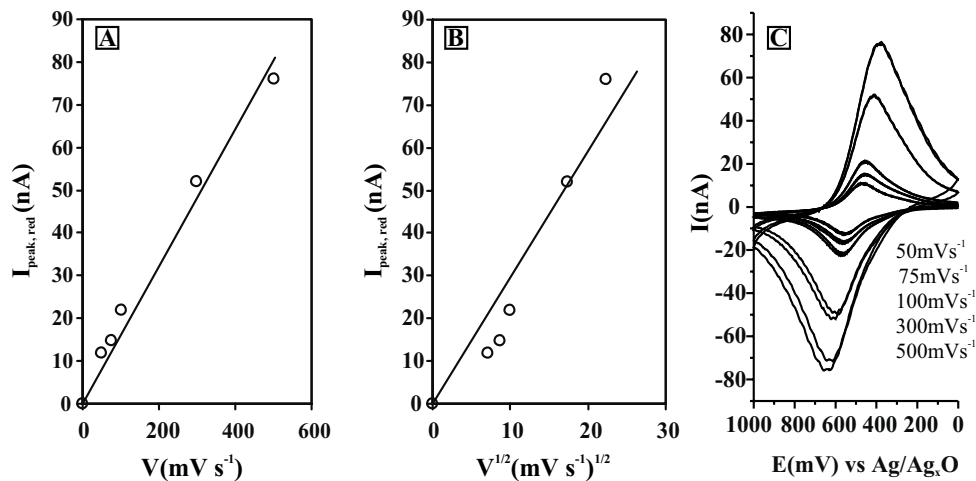


Figure 3.4: Peak Current ( $I_{p,\text{red}}$ ) plotted against A) scan rate,  $v$  (Adsorbed monolayer fit) and B)  $v^{1/2}$  (Diffusion based fit). C) Cyclic voltammograms used for this analysis.

scale of the electrochemical experiment (i.e. minutes).

This conclusion will be used extensively in the next chapter in an attempt to prevent delamination of poly-pyrrole from the superconductor.

While bonding to the surface is necessary for SAM formation, it is not sufficient to yield a structure which is ordered over large areas. It is extremely unlikely that all molecules will adsorb at the right bonding site and in the right conformation during the initial adsorption. There must, therefore, be some mechanism which allows for the defects to anneal. Fortunately, at longer time scales (hours) the amines on the surface will exchange with amines in solution [48]. A cycle of adsorption, desorption, re-adsorption is, therefore, possible and formation of predominately defect free, ordered, monolayers structures, true

SAMs becomes probable. The structure of such a true SAM atop a copper oxide superconductor is the subject of the next section.

### 3.4 Characterization of SAMs atop *ab*-plane of single crystal $\text{YBa}_2\text{Cu}_3\text{O}_{7-\delta}$ <sup>9</sup>

While knowledge of the packing motif is not crucial for the initial study of proximity effect in organic polymer superconductor structures, it is of indispensable value for the design of organic layers which are to be grown *epitaxially* on  $\text{RBa}_2\text{Cu}_3\text{O}_{7-\delta}$  superconductors.

The straight chain alkyl amine employed<sup>10</sup> in this section differs from the ones of the last section as it does not contain an electroactive group. It also differs from the ones previously studied [49] as the alkyl chain of the amine is partially fluorinate in order to enhance crystallinity. The major conclusions from the previous studies of alkyl amine SAM on  $\text{YBa}_2\text{Cu}_3\text{O}_{7-\delta}$  was indirect evidence for a highly ordered monolayer as witnessed by reflectance angle infrared spectroscopy (RAIRS) and a  $\sqrt{2}\times\sqrt{2}\text{R}45^\circ$  packing motif predicted by computer modelling [49]. Thus, the challenge here is to obtain direct experimental evidence for this structure and try to predict the molecular conformation in the monolayer.

One of the significant challenges associated with the direct imaging of

---

<sup>9</sup>This section is, in part, an adaptation of a paper intended for submission to Adv. Mater.

<sup>10</sup>The partly fluorinated alkyl amines used in this section was generously donated by R. Lee and coworkers from the University of Houston.

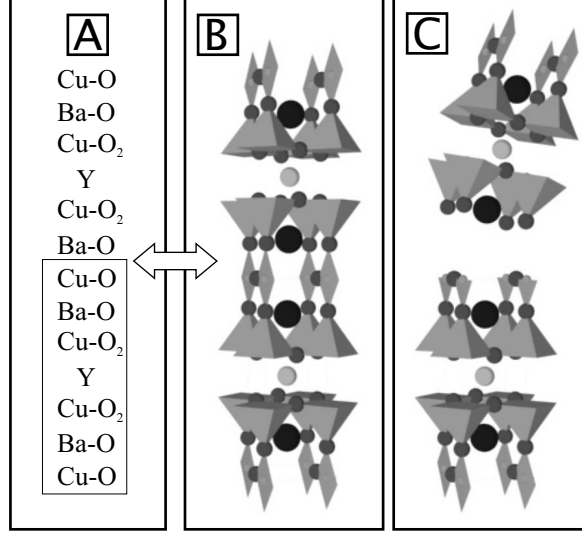


Figure 3.5: Cleaving  $\text{YBa}_2\text{Cu}_3\text{O}_{7-\delta}$  structure A) Labeling scheme for B) and C) (Box indicate one unitcell). The structure before (B) and after C) cleavage. Arrow indicates the cleavage plane between the Cu-O chain layer and the Ba-O sheet layer

the cuprate superconductor-localized monolayers has been identifying appropriate sample specimen with surfaces smooth enough for atomically resolved AFM. In the common SAM systems, like thiols on gold, low roughness can be attained by simply polishing and subsequently annealing the surface at elevated temperatures or by evaporating the metal onto mica [50] [51]. A similar protocol cannot be used with  $\text{YBa}_2\text{Cu}_3\text{O}_{7-\delta}$  system. This is due to the highly reactive nature and complex composition. While previous studies of ceramic and laser ablated cuprate films (Section 3.3) have been shown to be suitable for localizing amine monolayers, these samples were found to be too rough for

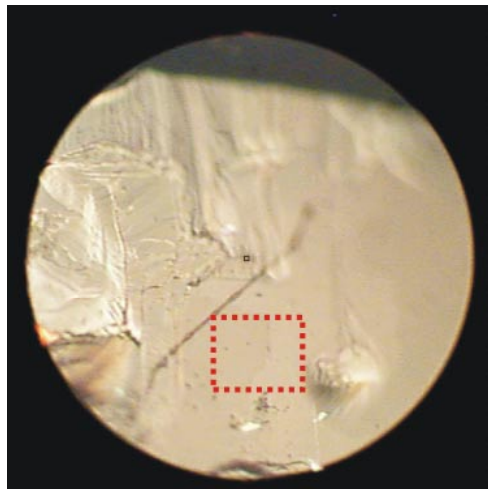


Figure 3.6: Optical micrograph of a cleaved  $\text{YBa}_2\text{Cu}_3\text{O}_{7-\delta}$  crystal. Red box indicates area of low roughness (Field of views  $\sim 2\text{mm}\varnothing$ )

direct structural characterization of the monolayer thereon. Thus, the substrate surfaces used in this study were prepared by cleaving a single crystal<sup>11</sup> along the crystallographic *ab*-plane (Fig. 3.5).

Examining the surface roughness of the cleaved surface after formation of the SAM yields roughness comparable to the Highly Ordered Pyrolytic Graphite (HOPG) reference. Cleaved crystals are therefore the substrate of choice as it yields large ( $0.05\text{mm} \times 0.05\text{mm}$ ) flat terraces (Fig. 3.6). This technique was adapted from a previous study by de Lozanne and coworkers [52], where crystals were cleaved in a similar manner, but at cryogenic temperatures. In the prior studies, the cleaved crystals were used for low temperature scanning tunnelling microscopy (STM) studies of the pristine  $\text{YBa}_2\text{Cu}_3\text{O}_{7-\delta}$

---

<sup>11</sup>The crystals for this study were prepared by Koki Mochizuki and Prof. John Markert.

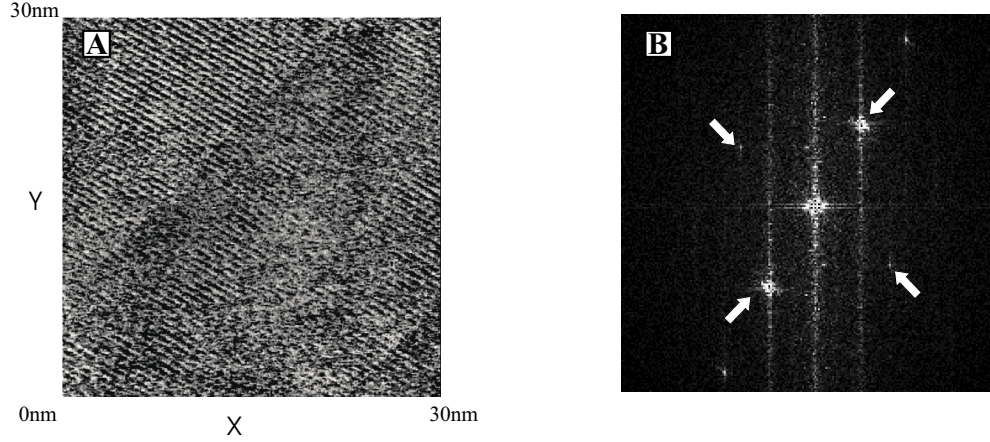


Figure 3.7: AFM of monolayer. A) Direct deflection mode images of  $\text{CF}_3(\text{CF}_2)_3(\text{CH}_2)_{11}\text{NH}_2$  atop  $\text{YBa}_2\text{Cu}_3\text{O}_{7-\delta}$ . B) Fourier transform image. The peaks represent a square  $5.6\text{\AA}$  unit cell.

surface. From this prior work, it was shown by correlating the possible cleavage planes with the STM images, that the cleavage primarily takes place between the Cu-O chain layer and the Ba-O sheet [52](Fig. 3.5).

The atomically resolved AFM images (see Section 3.1 for experimental details) of the SAM atop  $\text{YBa}_2\text{Cu}_3\text{O}_{7-\delta}$  is consistent ( $\pm 5\%$ ) with the  $\sqrt{2}x\sqrt{2}R45^\circ$  superstructure previously predicted for non-fluorinated alkyl amines [49] i.e. a square unit cell with a repeat distance of  $5.6\text{\AA}$  (Fig. 3.7). This unit cell does not correlate with any known surface reconstruction of pristine  $\text{YBa}_2\text{Cu}_3\text{O}_{7-\delta}$  [52–54]. These structural features were repeatedly detected in different areas on the crystal surface using various scan areas, directions and speeds.

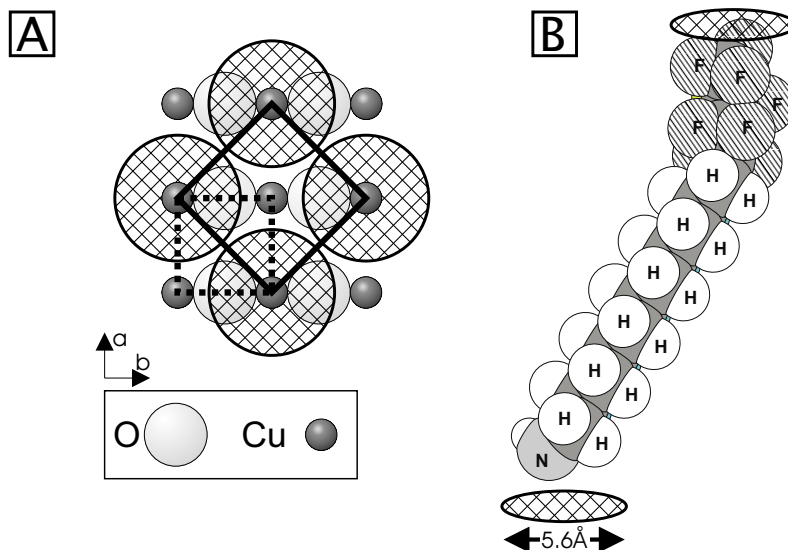


Figure 3.8: A) One possible setting of the  $\sqrt{2} \times \sqrt{2}$  R45° amine unitcell on the copper-oxide chain layer. Dotted line: YBa<sub>2</sub>Cu<sub>3</sub>O<sub>7-δ</sub> unit cell. Solid line:  $\sqrt{2} \times \sqrt{2}$  R45° SAM-superstructure. B) Space filling model of the molecule used for the AFM study. The molecular foot-print shown here (cross hatched circles) is consistent with the model discussed in the text.

To determine the bonding site of the amine on the surface of the superconductor, a surface diffraction experiment may be used. Several days of synchrotron beam time was therefore spent at Hasylab BW-1 (Hamburg, Germany) collecting data on a crystal surface prepared in a similar manner to the one used in the AFM experiments<sup>12</sup>. The data collection confirmed that it is possible to get a grazing incidence diffraction (GID) signal from the crystal surface in spite of the small size (2-3 mm Ø). However, no sharp diffraction

<sup>12</sup>This work was completed as a collaboration with Prof. T. Bjørnholm (University of Copenhagen) and R. Robert Feidenhans'l and coworkers (Risoe).



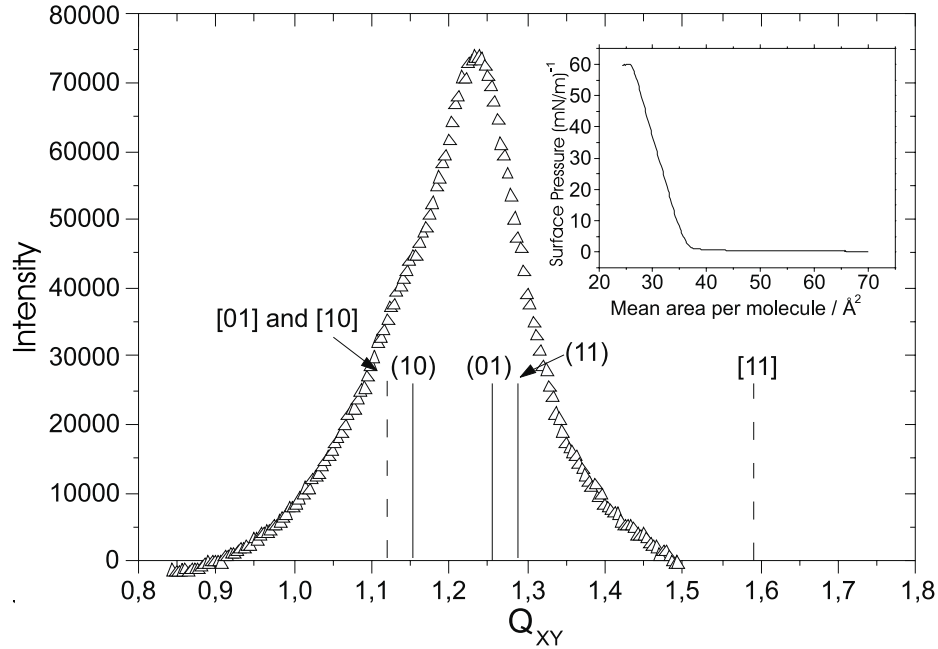


Figure 3.9: Grazing incidence X-ray data of the  $\text{CF}_3(\text{CF}_2)_9(\text{CH}_2)_{11}\text{NH}_2$  Langmuir monolayer supported atop an aqueous subphase. Solid lines: The calculated peaks of the pseudo hexagonal unitcell. Broken line: The calculated reflections of a square  $5.6\text{\AA}$  unit cell. Inset: Compression isotherm of the Langmuir monolayer.

signal was found at the expected  $(hk)=(2\ 0)$ ,  $(0\ 2)$  or  $(2\ 2)$  positions.

An X-ray reflectivity [55] and grazing incidence diffraction (GID) [55] structural analysis of Langmuir film of a similar semi-fluorinated alkyl amine was undertaken by a collaborating group (Prof. T. Bjørnholm and co-workers). The alkylamine used for the Langmuir film is prolonged by six  $\text{CF}_2$  units relative to the alkyl amine used on  $\text{YBa}_2\text{Cu}_3\text{O}_{7-\delta}$  as it has been shown both experimentally and through theoretical studies that the replacement of flexible

hydrocarbon by stiffer fluorocarbon increases the crystallinity of the Langmuir film [56] [57] and, thus, enhances the x-ray signal. This structural analysis was undertaken to: a) elucidate if the molecular packing regardless of surface symmetry would result in a square unitcell, and b) to deduce if the unitcell area  $(5.6\text{\AA})^2$  would be large enough to accommodate at least one formula unit of a closed packed array of the semifluorinated amine.

From the surface pressure vs. surface area graph of the  $\text{CF}_3(\text{CF}_2)_9(\text{CH}_2)_{11}\text{NH}_2$  Langmuir film (Fig. 3.9 inset) it is clear that a dense monolayer is found at surface area from  $\sim 35\text{\AA}^2$  to  $\sim 25\text{\AA}^2$ . The data collection was performed on this monolayer compressed to a surface area per molecule of  $\sim 30\text{\AA}^2$  at a surface pressure of  $P \sim 35\text{mN/m}$  (Fig. 3.9 inset). The subphase temperature and pH was  $21(3)^\circ\text{C}$  and 11, respectively.

The GID measurements of the Langmuir-film of  $\text{CF}_3(\text{CF}_2)_9(\text{CH}_2)_{11}\text{NH}_2$  shows an approximately hexagonal closed packed array with a unit cell area ( $\sim 30\text{\AA}^2$ ) similar to the area per molecule deduced from the compression isotherm, i.e. there is *one* molecule per unitcell. Similarly, the  $31\text{\AA}^2 \pm 10\%$  of the SAM on  $\text{YBa}_2\text{Cu}_3\text{O}_{7-\delta}$  is large enough to accommodate *one* closed packed molecule per unitcell.

The X-ray reflexivity data provides the electron density across the interface ( $r(z)$ ) and is qualitatively similar to previously studied Langmuir films of semi-fluorinated hydrocarbons [58], i.e. fluorocarbon up, hydrocarbon down, orientation (Fig. 3.10A). The measured electron density was fitted to a three box model [55] where each box holds a different number of electrons corre-

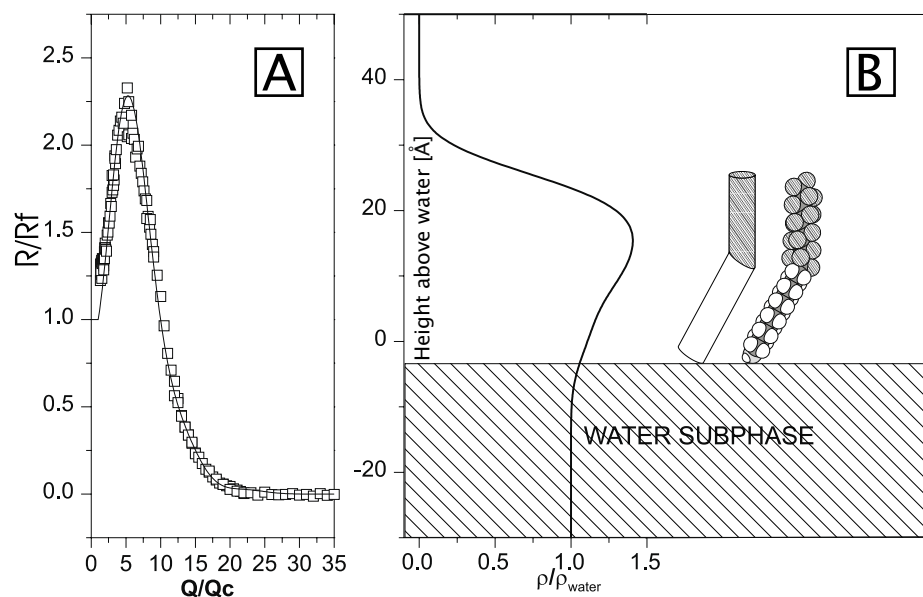


Figure 3.10: X-ray reflectance data. A) In reciprocal space. B) Real space transformation and molecular models consistent with the measured charge distribution. Note: It is not possible to determine if the fluorinated part of the molecule has a helical or all trans structure from this x-ray data.

sponding to the fluorocarbon, hydrocarbon, and amine moieties. A monolayer thickness of 25.5Å was deduced from this fit.

Knowing the base area of the unit cell (from GID data), the height of the unit cell (from the reflexivity), and number of formula units per unit cell makes it possible to construct a stiff rod model where the hydrocarbon and fluorocarbon sections are modelled by rods that has diameter and length deduced from known structures of perfluoro or perhydrocarbon monolayer (Fig. 3.10B). The stiff rod model yields a closed packed structure where the fluorocarbon section is perpendicular to the water surface and the hydrocarbon section is tilted  $\sim 30^\circ$  with respect to the surface normal (Fig. 3.10C). Similar bends have been found in previous structure studies of Langmuir films of semifluorinated hydrocarbons and amphiphiles [58–61].

Returning to the structure of the SAM monolayer on  $\text{YBa}_2\text{Cu}_3\text{O}_{7-\delta}$ . Previous calculations on hydrocarbon amines  $\text{YBa}_2\text{Cu}_3\text{O}_{7-\delta}$  show that a  $\sim 30^\circ$  angle to the surface normal yields a minimal energy structure [49]. By combining this knowledge with the molecular conformation found in the Langmuir films. a model of the molecular conformation of the SAM is derived, where the hydrocarbon subunit forms a  $\sim 30^\circ$  angle with the surface normal and where the fluorocarbon is perpendicular to the surface (Fig. 3.8B)

**To summarize:** The main conclusion of this chapter is that organic molecules may be adsorbed strongly onto superconductor surfaces if they contain an amine functionality. This would, however, be irrelevant in the present discussion if the amine not also served as an etchant removing the corrosion

layer prior to adsorption. The combination of the two processes is an organic layer strongly adhered directly to the superconductor which allows for charged particle to be passed from the superconductor to the organic layer and back. This is a desired feature as charge transfer from the superconductor to the organic layer is central to the superconductive proximity effect.

Presented in this chapter was also, to the best of my knowledge, the first direct image of the packing motif of a SAM atop a copper oxide superconductor. Collectively, the AFM and the prior computational studies [49] point to a consistent picture where straight chain primary amines form highly ordered  $\sqrt{2} \times \sqrt{2}$  R45° overlayers on  $\text{YBa}_2\text{Cu}_3\text{O}_{7-\delta}$ . This knowledge may be exploited in the future to create superconductor/organic conductor interfaces where the organic conductor exhibit enhanced order, and therefore enhanced conductivity.

## Chapter 4

# Superconductor conductive polymer assemblies

In the early days of proximity effect research, two classical experiments were used to prove the existence of this phenomenon (Section 1.6)

- Suppression of superconductivity in a S/N bilayer (where S is a thin film)
- Passing of supercurrent through the N layer of an S/N/S junction

While new scanning probe techniques have been added to the list of possible proximity effect experiments [62–65], these classical experiments will still remain at the center of the pursuit towards proving or disproving proximity effect in conductive polymers/superconductor assemblies.

Previous work by Haupt *et al.* on poly-pyrrole/YBa<sub>2</sub>Cu<sub>3</sub>O<sub>7</sub> bilayers has shown that it is possible to modulate reversibly  $T_c$  in a manner which is qualitatively consistent with the proximity effect [66]. To obtain these results, it was necessary to employ very thin (500-1500Å) mixed *a*, *c*-axis films, which inherently have high surface roughness. The use of rough films makes the assessment of film thickness difficult and without detailed knowledge of the thickness quantitative analysis of such systems would seem to be futile. Thus,

if we are to contribute with new insight into the proximity effect in conductive polymers, it will be necessary to design a sample where the geometry of the superconductor is known in great detail. There are, in theory, at least are two ways to solve this problem: a) deposit a thicker film and subsequently thin it or b) localize the polymer to a small area where the geometry of the sample is known in great detail. While both approaches are conceptually simple, the realization that the characteristic length scales of proximity effect are in the nm range severely limits the number of techniques which are available to this end. Adding another level of complication is the fact that the superconductor readily reacts with common environmental agents like  $\text{CO}_2$  and  $\text{H}_2\text{O}$ , which easily renders the superconductor surfaces unfit for many proximity effect experiments. However, we have designed a protocol which by combination of lithography, scanning probe, and electrochemical polymerization allows for thinning of the superconductor and localization of the polymer above this thinned section. This preparation protocol will be outlined in the next section. The experimental for this protocol will be given in Sections 4.1.1 to 4.1.4. The discussion of the final structure is provided in Section 4.2, as well as a summary.

## **4.1 Superconductor/conductive polymer bilayer preparation**

The sample preparation starts with PLD of a thin superconducting film onto an insulating substrate (Section 2.8) (Fig. 4.1A). Using a thin film has

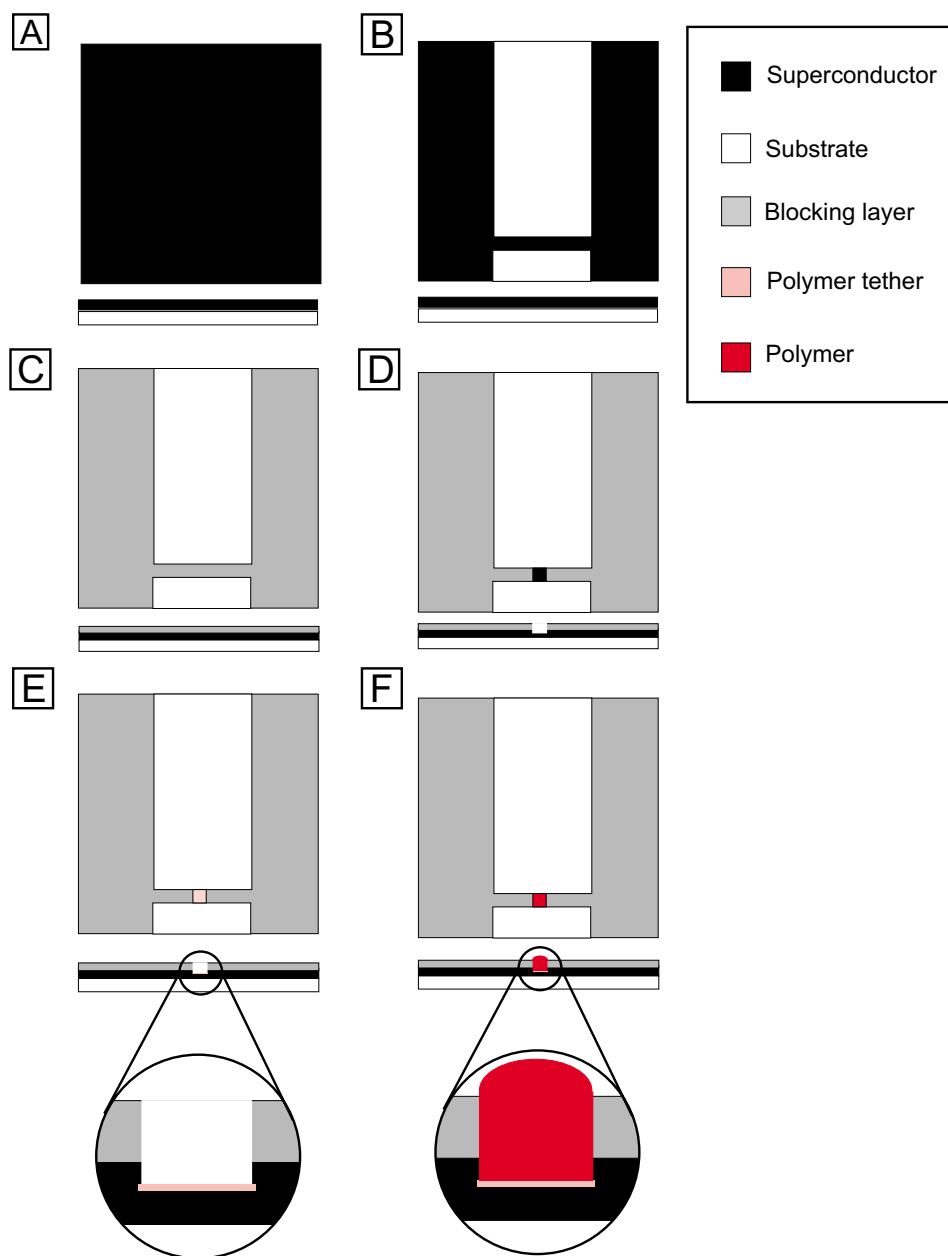


Figure 4.1: Sample preparation. Top and cross sectional views. Notice the thin tether layer in the enlarged view of E and F (See text for details, not drawn to scale).



the advantage over bulk pellet and single crystals in that the large area allows contacts to be made easily to the film while crystallographic orientation still may be controlled. Epitaxially grown thin films also ensure that the superconductor does not delaminate from its insulating support even after it has been patterned. Furthermore, the thickness of the active superconducting layer of the thin film is easily made comparable to the thickness over which proximity effect is expected to take place.

Following the deposition (Section 2.10), the film is patterned into a bridge structure. This is done by masking off the bridge pattern and then removing the unmasked superconductor by ablation (Fig. 4.1B). The bridge structure ensures a uniform current density in the area where proximity effect is to take place and that the current and voltage contacts are removed from this area.

In order to localize where the polymer grows, the bridge must be covered with an organic blocking layer (Fig. 4.1C). A section of the bridge is then thinned using an AFM probe (Fig. 4.1D). The AFM processing has two effects: a) it exposes a small area of the superconductor surface so that it may be further modified and b) it makes it possible to control the superconductor thickness, an important parameter in suppression of superconductivity in S/N bilayer experiments (Section 1.6 and 5.2). The exposed superconductor is then modified with a monolayer of amine tethered pyrrole (Fig. 4.1E) before the poly-pyrrole is grown selectively on top by electrochemical polymerization (Fig. 4.1F). The use of a blocking layer and the SAM tether was omitted in

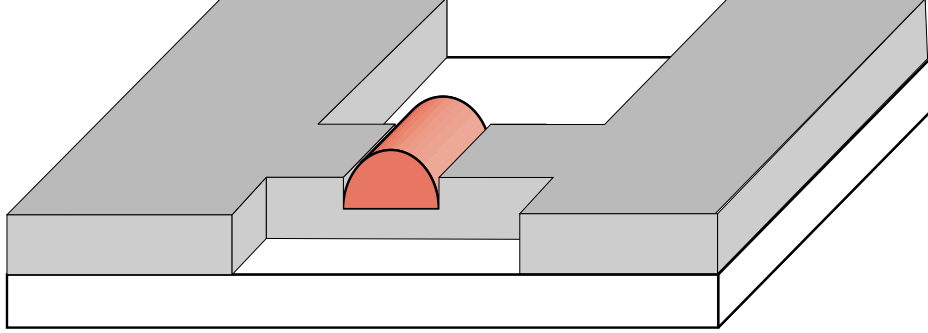


Figure 4.2: The final superconductor (gray) polymer (red) bilayer structure. (perspective view, not drawn to scale)

*some* of the samples described in the following sections.

There are several features of this type of sample (Fig. 4.2) which makes them advantageous, e.g. the critical current is measured in a bridge of small cross sectional area, which lowers the required current needed to exceed the critical current density. In turn, this makes the requirement of good contacts to the sample less stringent and limits the galvanic corrosion at the contacts. Also advantageous is that the area of the bridge where S/N proximity effect takes place can be chosen arbitrarily, which makes it possible to confirm whether the S/N effect scales with the area. Finally, the thickness of the S layer is determined by the extent of AFM thinning, not by the thickness of the original film.

The remaining portion of this section is devoted to the details of sample preparation.

#### **4.1.1 Experimental: Preparation of 100 $\mu$ m wide superconducting bridge structure by ablation through a shadow mask**

The following is an account of a typical protocol used for producing the bridge structure and contact pads pattern used for the critical current measurements described in Section 5.5. Laser and optical setup was described previously in Section 2.8.

Initially the Ag-paint used to bond to the heater during deposition (see Section 2.8) was removed by placing the film face down on a clean cover glass wrapped in lens paper and scraping with a razor blade. This procedure ensures that the Ag will not influence the electrochemical deposition and doping/undoping of the conductive polymer assembly.

The film was then mounted on a steel block using double sided tape and an “H” pattern was masked off using two pieces of Pt foil and a piece of 100 $\mu$ m Pt wire. Then, the masked film was placed beyond the focal point in the laser ablation chamber, where the beam dimensions were ca. 4 x 11mm<sup>2</sup>. 10 pulses with an energy of  $\sim$ 300mJ was delivered at 1Hz to the mounted sample which removed the unwanted superconductor and created the superconductor bridge outline by the shadow mask. While using one pulse will define the pattern, the ablated area will contain droplets which may short the structure during the following steps. Employing 10 pulses, however, removes the vast majority of the unwanted superconductor.

#### 4.1.2 Experimental: Preparation of localized thin superconductor structures by Atomic Force Microscope (AFM) Machining<sup>1</sup>

All AFM measurements were performed on a Nanoscope Multimode III (Digital Instruments, Santa Barbara, CA).

Specialized AFM probes with diamond tips on a stainless steel cantilever are available. However, for the research described here standard Tapping Mode Si-probes (L:125 $\mu$ m, F~300KHz, Digital Instruments, Santa Barbara, CA) or tungsten carbide covered Si-probes (NSC11/W2C, Silicon-MDT Ltd., Moscow, Russia) were found to be adequate. These standard tips were obtained with less expense than the diamond tips.

Initially, the thin film was mounted on the sample puck using double sided tape and placed on the AFM scanner so that a 0 deg. scan is parallel to long axis the of section to be thinned (i.e. scanning was performed in the direction perpendicular to the superconducting bridge). This approach ensures that if debris is trapped under the tip during AFM-machining it will not damage the structure.

Unlike normal tapping mode or contact mode application, exertion of a high force by the tip on the sample is required. The laser beam, which is used to measure the displacement of the tip, is therefore not focused at the endpoint of the cantilever, but rather on the base. This geometry ensured the laser was

---

<sup>1</sup>This technique is commonly referred to as nano indentation. The term is not used here because it usually refers to plastic deformation by a single pass of probe in soft materials and not the abrasive action of the tip on hard materials.

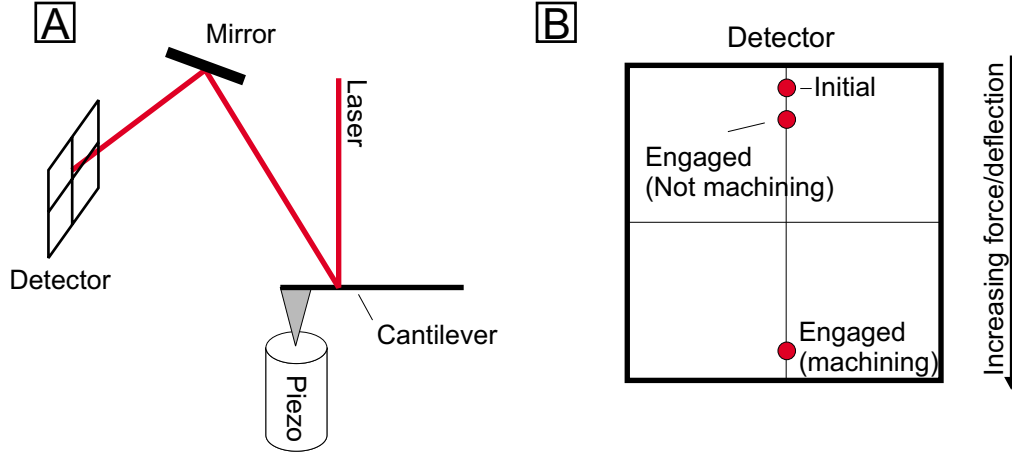


Figure 4.3: A) The AFM setup. B) Laser position during different processes. (Note: The detector may be moved to ensure that the laser will be within range once a high force is applied.)

within the range of the detector once high force was applied. Furthermore, the mirror which is used to direct the laser beam reflected off the tip towards the detector, was tilted so that the laser reached the detector  $\sim \frac{1}{7}$  from the edge (Fig. 4.3, Initial). This procedure leaves most of the detector range available to the response of upward deflection of the cantilever. A "before" image was typically gathered using a deflection set point  $\sim 10\%$  below the the initial disengaged value (Fig. 4.3), a proportional and integral gain of 6, a scan range and speed of  $150\mu\text{m} \times 150\mu\text{m}$  and 5Hz, respectively. Using these parameters, no damage (cracks etc.) was apparent (Fig. 5.6 and 4.9A). Once the area of machining was aligned at the center of the scan range and the scanning aspect ratio had been lowered to yield the desired thickness, the detector was moved

so as to extend the scanner to its maximum length. Immediately after, the stepper motor was employed to move the sample up  $\sim 5\mu\text{m}$  and the feedback deflection set point was then changed until ca. 0V was applied to the z-axis of the piezo (Caution: Do not leave the potential on z-axis piezo at high values ( $>100\text{V}$ ) for extended periods of time. This will cause the piezo to depole).

Occasionally, it was necessary to move the detector even further up, manually, to bring the beam reflected off the cantilever within range. The proportional and integral gain were then lowered so that scanning would maintain a constant height. The scan rates were typically 10-30Hz for a  $100\mu\text{m}$  section. Several attempts at correlating the force applied to the tip, the scan rate and the wear of the tip with the rate of machining proved unsuccessful. Thus, the sample thickness was gauged periodically during scanning by increasing the feedback (integral gain and proportional gain) and lowering the scan rate to 5Hz. Scanning was terminated once the section had the desired thickness. Once the detector was moved back to its original position and the controls were set as the "before" image, a profile of the thinned section was gathered. The scan angle was normally chosen so that it was nonparallel with the feature of interest, as drifts from scan line to scan line might otherwise distort the profile. The "before" and "after" image were, therefore, typically gathered using a 45deg. scan angle.

#### 4.1.3 Experimental: Formation of blocking layer and pyrrole tether layer

The blocking layer was formed by exposing the patterned film to a  $\sim 1\text{mM}$  solution of undecylamine in dry acetonitrile inside the  $\text{N}_2$ -atmosphere glovebox for more than 24h. The film was rinsed extensively and any resulting solvent was removed by using the capillary action from a KimWipe. In spite of this extensive rinse, the blocking layer was found by AFM to be several hundred nm thick. While such thick films would provide complications of experiments which require the formation of single monolayer motifs, the thick assembly here provides a convenient methodology for creating a surface passivation layer.

The pyrrole template layer was formed by exposing the sample to a 70mM solution of 3-aminopropyl-N-pyrrole in hexanes for  $\sim 2.5\text{h}$ . The sample was rinsed extensively with pure solvent before being blown dry in a gentle stream of  $\text{N}_2$ .

#### 4.1.4 Experimental: Electropolymerization of pyrrole

Two different pyrrole<sup>2</sup> solutions were used for the polymerization of pyrrole. The first consisted of 0.1M pyrrole, 1 weight-% MeOH, 0.1M tetraethylammonium tetrafluoroborate in dry acetonitrile. The second of 0.1M pyrrole, 0.1M tetrabutylammonium hexafluorophosphate in dry acetonitrile.

---

<sup>2</sup>The pyrrole was filtered through a short column of activated alumina immediately prior to making solutions.

These solutions were shielded from light and stored in the glovebox during their use, which extended over months. The electrochemistry was conducted using the same setup and procedures as described in Section 3.1. The potential required for polymer growth was determined by increasing the size of the potential sweep of a number cyclic voltammograms until the clear fingerprints of polymer growth were evident ( $\sim 1.0$ - $1.2$ V vs. Ag/Ag<sub>x</sub>O) i.e. an increase in the anodic currents at high positive potentials. The films were then grown to the desired thickness by performing several cyclic voltammograms (CV) from zero to this potential. The thickness increase during growth was gauged by the increase in current in the potential range where no polymerization took place. Once polymerization had been completed, the film was removed from the pyrrole solution rinsed extensively with pure dry acetonitrile and dried by using the capillary action from a KimWipe.

Doping and undoping were performed using the same 0.1M electrolyte solutions employed during the polymerization. The potential needed for doping and undoping was determined by an initial CV before a potential step was applied for  $\sim 60$  seconds. The film was removed from the electrolyte solution while the potential was still being applied.

## **4.2 Characterization of polymer-superconductor assemblies**

The first issue to address is whether the blocking layer does effectively block polymer growth outside the area exposed by thinning with the AFM



probe. As shown in Figure 4.4, this is indeed the case and to the best of our knowledge these studies represent the first reports of conductive polymer localized in a predetermined area atop a high temperature superconductor.

Details of the polymer growth is illustrated using the cyclic voltammograms gathered while preparing the sample of Figure 4.4. These experiments show the general trend of tens of samples prepared in a similar way.

The initial scans (Fig. 4.5) show large anodic current. This behavior is not unique to voltammetry of solutions containing pyrrole and is therefore not an indication of polymer growth.

However, once polymer growth has commenced (Fig. 4.6), there is no evidence that it is hampered by the behavior found in the initial scan.

A major obstacle when working with these samples is that the area of the superconductor, exposed by thinning with the AFM, is smooth, leaving no structural features which may interlock with the polymer. This lack of mechanical interaction leads to delamination (Fig. 4.7) which may prove problematic for the proximity effect measurements as the area of the S/N interface is decreased. On rare occasions even, delamination between different sheets of polymer has been witnessed. In an attempt to overcome the problem with delamination, a number of samples were prepared in which the superconducting film was exposed to a solution of 3-aminopropyl pyrrole prior to polymerization. The rationale behind using this molecule is that it can form a surface tethered monolayer on the superconductor surface, which then may

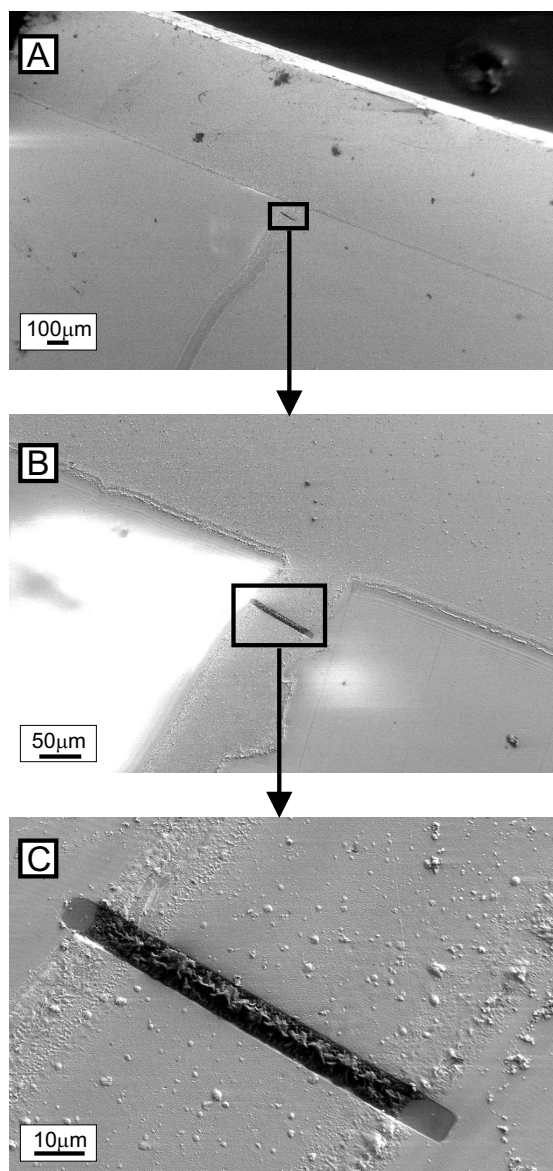


Figure 4.4: Localized polymer growth on a undecylamine blocked  $\text{NdBa}_2\text{Cu}_3\text{O}_7$  bridge. SEM images with increasing magnification from A to C. Polymer appears as a dark line in the center of the image. (Note: The dark patch in upper right corner of A is the carbon support tape, see Fig. 4.5 and Fig. 4.6 for deposition details).

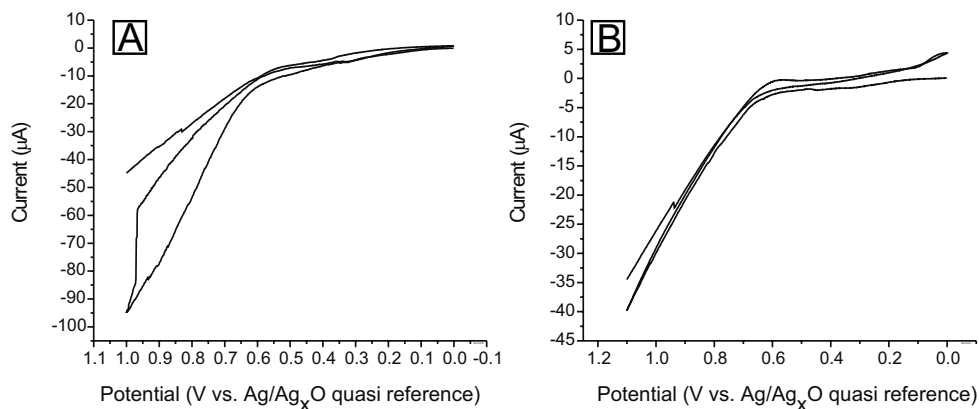


Figure 4.5: Initial CV's of a undecylamine blocked  $\text{NdBa}_2\text{Cu}_3\text{O}_7$  bridge with a  $6\mu\text{m} \times 90\mu\text{m}$  opening. A) First three scans and B) the following three. (Scan rate= $100\text{mVs}^{-1}$ , 0.1 M pyrrole, 1 weight-% MeOH, 0.1M tetraethylammonium tetrafluoroborate in dry acetonitrile.)

serve as a template for polymer growth. It was expected that such a strategy could yield a polymer which is bound to the surface through the amine superconductor interaction. This technique has been used previously to create strongly adherent polymer atop cuprate superconductors [67].

When initially examining the surface of a sample which was exposed to the amine-pyrrole adsorbate solution, it seems that there has been no polymer growth as the surfaces in the trench appear smooth (Fig. 4.9B). Upon closer examination it is clear that there is material in the trench and that it is much smoother than the polymer grown without the tether present (Fig. 4.9C). This is consistent with a previous study of polypyrrole grown on  $\text{YBa}_2\text{Cu}_3\text{O}_7$  films modified with the same molecule [67]. An unfortunate by-product of

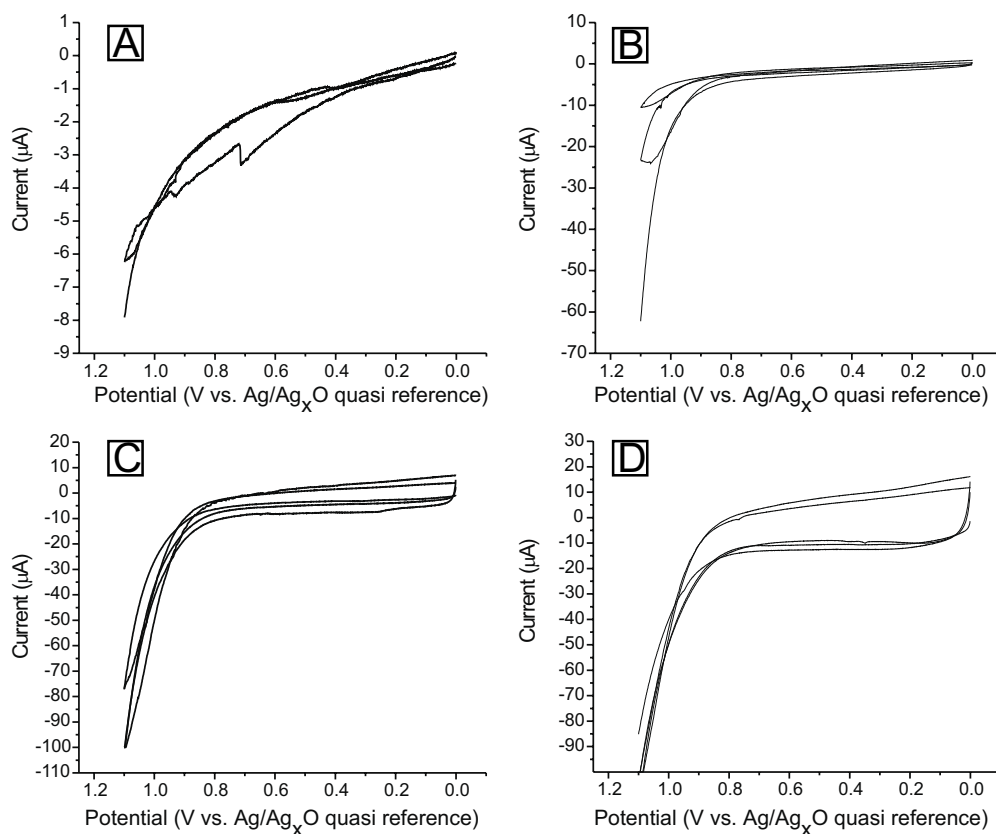


Figure 4.6: Polymer growth on the same sample as Fig. 4.5. A) First three scans which show polymer growth, followed by continued growth five scans at a time in B), C), and D). (Scan rate= $100\text{mVs}^{-1}$ ,  $\text{NdBa}_2\text{Cu}_3\text{O}_7$  bridge with a  $6\mu\text{m} \times 90\mu\text{m}$  opening, 0.1M pyrrole, 1 weight-% MeOH, 0.1M tetraethylammonium tetrafluoroborate in dry acetonitrile.)

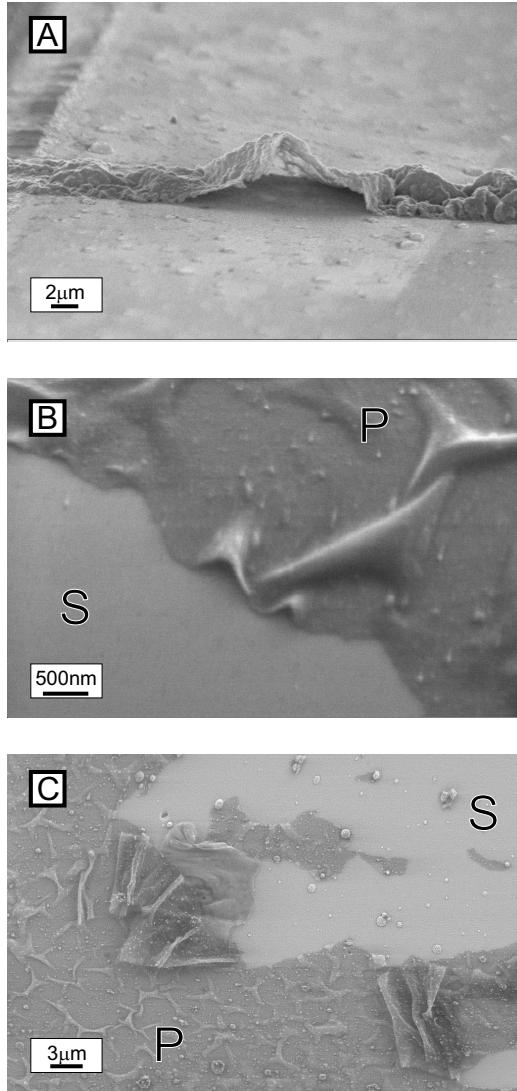


Figure 4.7: Delamination: A) Polymer layer on top of the superconductor microbridge. Viewed at 75° angle. B) Polymer covering a large thinned area. C) Polymer mechanically removed with a wooden stick illustrating poor adhesion (S=Superconductor, P=Polymer). (view angle B and C: 45°)

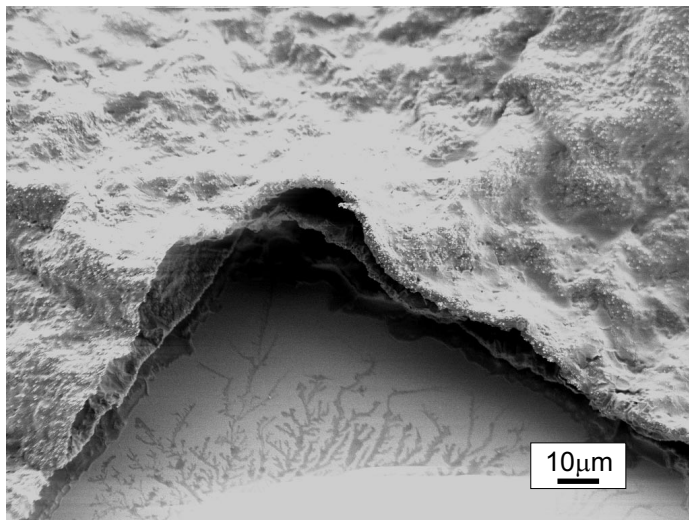


Figure 4.8: Polymer delamination showing that, in select cases, even the polypyrrole separates into sheets.(Polypyrrole on  $\text{NdBa}_2\text{Cu}_3\text{O}_7$ )

using the undecylamine as a blocking layer is that the amine-pyrrole adsorbate molecules may dissolve into it and polymer growth is, thus, found outside the thinned section. This makes the contrast between unthinned and the thinned area weaker. However, the sample still appears distinctly different from a sample which has been treated in the same manner, but without polymer growth (Fig. 4.9A).

The electrochemistry which occurs during polymerization of the modified surface (Fig. 4.10) and unmodified surface (Fig. 4.6) samples appear similar, except the modified sample seems to grow at a more uniform rate. It is not possible to ascribe this response to changes made in the thinned area, as the amine-pyrrole modified sample show polymer growth outside this area

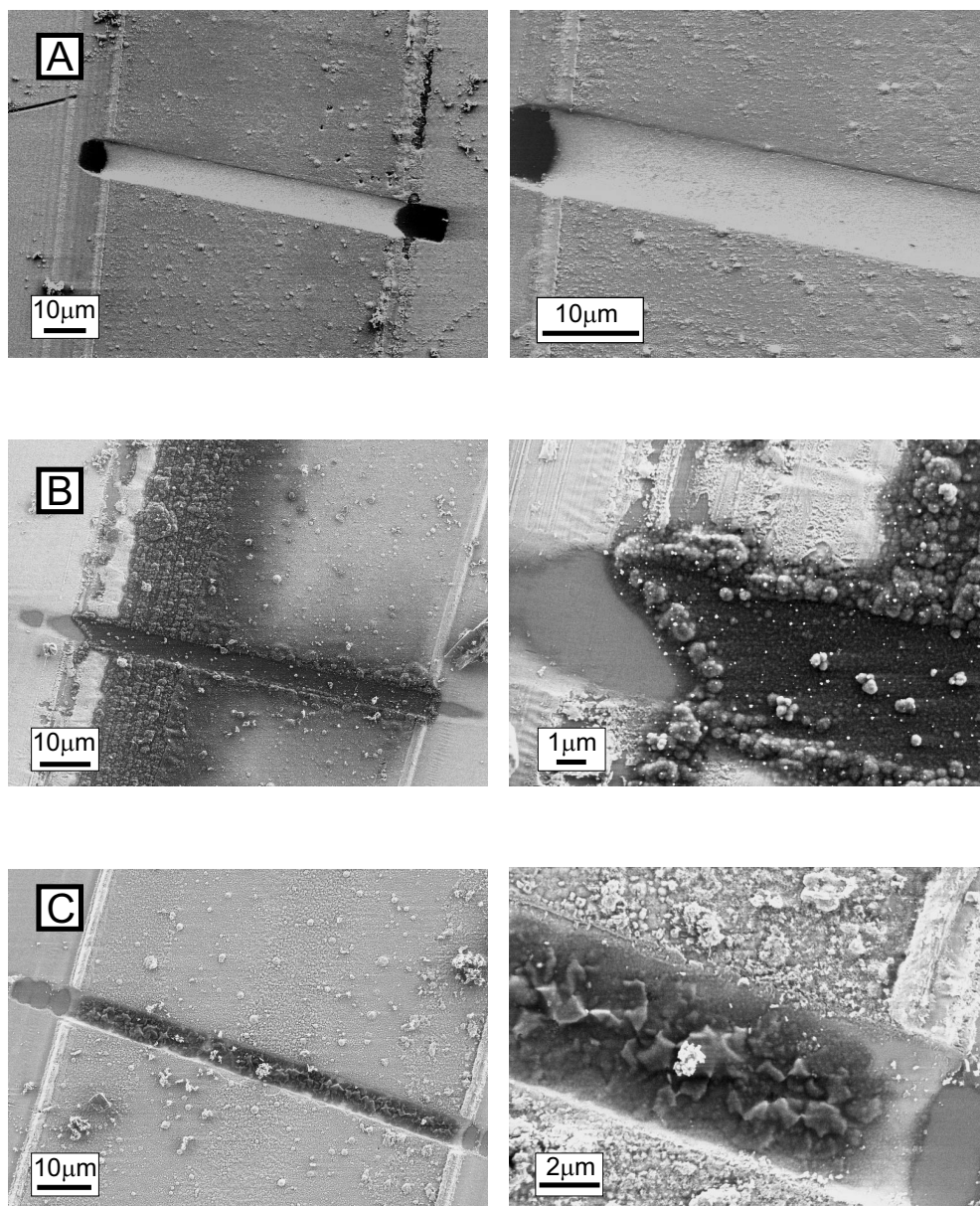


Figure 4.9: Electron micrograph evidence for strong adhesion of tethered polypyrrole to  $\text{NdBa}_2\text{Cu}_3\text{O}_7$ . A) Sample without polymer. B) Tethered polypyrrole (Note: the tether molecule was adsorbed into the blocking layer, leading to polymer growth outside thinned area) C) Polypyrrole without tether. Notice the difference in polymer morphology between B and C.

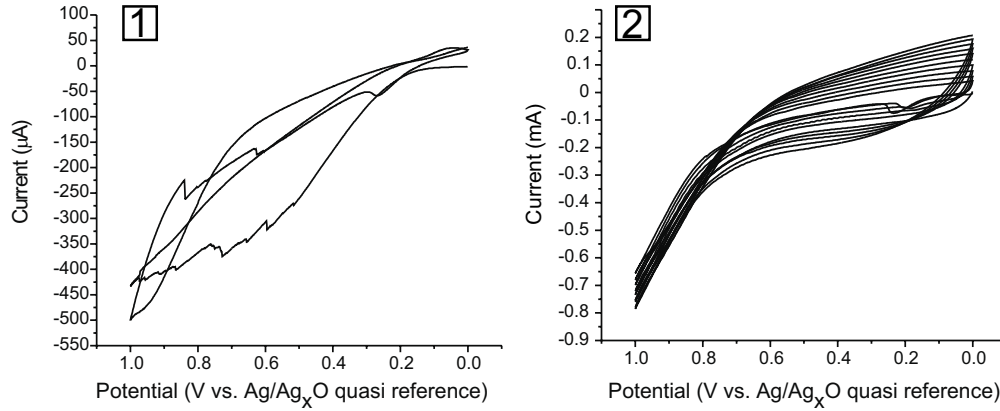


Figure 4.10: Polymer growth on sample in which the thinned area has been modified with 3-aminopropyl-N-pyrrole. 1) Initial four scans which show growth. 2) The following 20 scans. (Scan rate= $100\text{mVs}^{-1}$ ,  $\text{NdBa}_2\text{Cu}_3\text{O}_7$  bridge, 0.1M pyrrole, 1 weight-% MeOH, 0.1M tetraethylammonium tetrafluoroborate in dry acetonitrile.)

(Fig. 4.9B). The doping and undoping cycles of the polymer grown with and without the template layer are presented in Figure 4.11.

**To summarize:** In this chapter a protocol was presented (Sections 4.1 to 4.1.4) which allows for a) localized polymer growth and b) selective thinning of the superconductor. This protocol allows for the creation of S/N bilayer where the geometry of the superconductor can be known in great detail, which, in turn makes quantitative analysis of the proximity effect possible. It was also shown that in the absence of an adhesion layer, the polypyrrole often delaminates. However, some initial evidence was given that delamination could be overcome by treating the thinned area with 3-aminopropyl-N-pyrrole prior to electropolymerization. In these samples the 3-aminopropyl-N-pyrrole



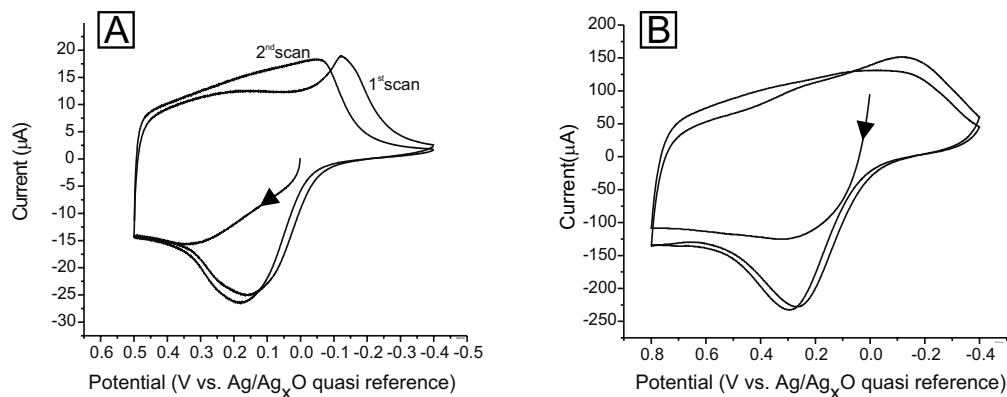


Figure 4.11: Doping and undoping cyclic voltammograms for A) poly-pyrrole not tethered to surface B) poly-pyrrole tethered to surface. (Note: the first undoping cycle is shifted in A as it is the first cycle after polymerization) (Scan rate= $50\text{mVs}^{-1}$ , in  $0.1\text{M} [\text{Et}_4\text{N}][\text{BF}_4]$  acetonitrile solution.)

served both as a templates for the polymer growth and as a tether between the superconductor and the polymer.

Collectively, these new procedures provide methods for bringing conductive polymers and high- $T_c$  superconductors together into functional composites, where the geometry is controlled on the nm scale. With such controlled structures it will be possible to examine conductive polymer/high- $T_c$  superconductor interfacial interactions in greater detail than was previously possible.

## Chapter 5

### On the superconductive properties of high-temperature superconductor/conductive polymer assemblies

Now that the theoretical foundation (Chapter one) and the practical aspect of making conductive polymer/high temperature superconductor composites have been presented (Chapter four), it should be possible to both design and perform measurement on samples which may support the proximity effect. This is the subject of the present chapter, which starts with charge transport across a S/N interface (Section 5.1), followed by an introduction to the quantitative description of suppressing superconductivity on the S side of an S/N interface (Section 5.2). From Section 5.2, it becomes clear that an evaluation of the suppression of superconductivity in S is advised before any S/N/S Josephson like junction is attempted. Also, clear from Section 5.2 is that the  $S/\frac{N}{S}/S$  geometry, where  $\frac{N}{S}$  represents an area where the proximity effect of N has weakened the superconductivity of S<sup>1</sup>, will yield this type of information. Section 5.4 describes the details of making the  $S/\frac{N}{S}/S$  sample

---

<sup>1</sup>This type of sample is known as a Mercereau-Norany bridge, if the length of  $\frac{N}{S}$  area is sufficiently small and the suppression sufficiently large to support Josephson currents. (see reference [68], [69])

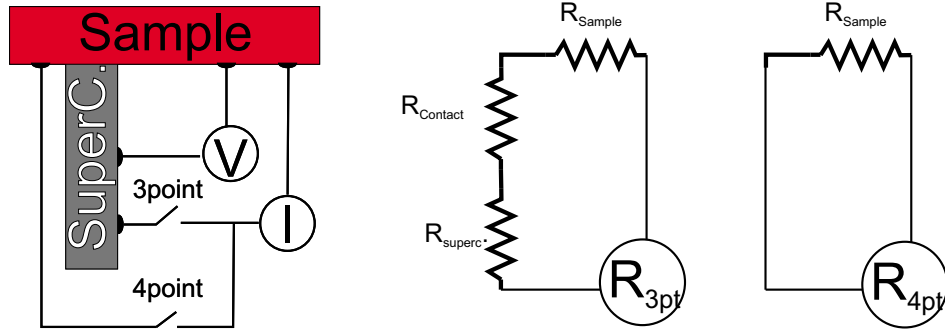


Figure 5.1: Sample setup and equivalent circuit for contact resistance measurement (See text for labeling).

and Section 5.5 provides current transport measurements. The discussion of the observed behavior of the  $S/\frac{N}{S}/S$  sample is left until Section 5.6.

### 5.1 On the measurement of contact resistance of superconductor/normal conductor (S/N) interfaces

The discussion of experimental approaches for exploration of the proximity effect begins with what is, arguably, the simplest possible assembly and measurement: Transport of current across a single S/N interphase. This type of measurement is also known as contact resistance ( $R_c$ ) measurement. While  $R_c$  is *not* the optimal measure of the proximity effect, it is included here to illustrate some of the key problems associated with experimental proximity effect measurement and how these stumbling blocks may be overcome.

Experimentally, the contact resistance is found by combining two separate resistance measurements which are based on a 3-point(3pt) and

4-point(4pt) contact geometries (Fig. 5.1). The two measurements differ by whether or not the superconductor and S/N contact is in the current path as illustrated by the equivalent circuit (Fig. 5.1). Examining the contributions to each circuit reveals:

$$R_{3pt} = R_{sample} + R_c + R_{superconductor} \quad (5.1)$$

$$R_{4pt} = R_{sample} \quad (5.2)$$

$$R_{3pt} - R_{4pt} = R_c + R_{superconductor} \quad (5.3)$$

Thus, when the conditions  $T < T_c$  and  $I < I_c$  are satisfied, the contact resistance may be calculated by

$$R_c = R_{3pt} - R_{4pt} \quad (5.4)$$

as the superconductor line resistance  $R_{superconductor}$  drops out of the equation. To be able to report a  $R_c$  value would require the resistance to be independent of current density (i.e. Ohmic). However, this is not always the case. Thus, reported here instead is the contact potential

$$V_c = \frac{V_{3pt} - V_{4pt}}{I} \quad (5.5)$$

where  $V_{3pt}$  and  $V_{4pt}$  are the potential differences when the current ( $I$ ) is passed in the 3-point and 4-configurations, respectively.

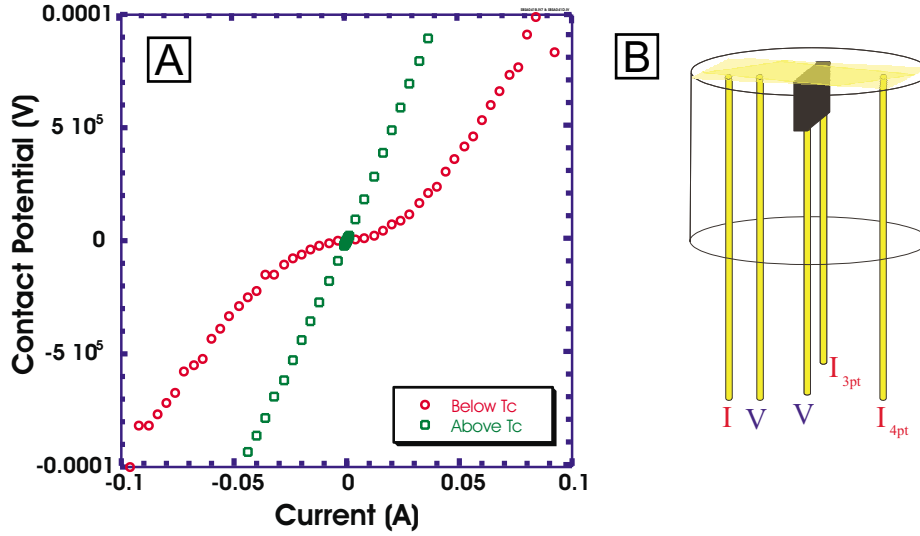


Figure 5.2: Contact resistance on Au/(Pb,Bi)<sub>2</sub>Sr<sub>2</sub>Ca<sub>2</sub>Cu<sub>3</sub>O<sub>7</sub> S/N interface. A) IV curves B) Sample geometry (The Superconductor (black) is embedded in epoxy with three gold wires (yellow) and gold (transparent yellow is evaporated on top).

Experimental data on the S/N interface between (Pb,Bi)<sub>2</sub>Sr<sub>2</sub>Ca<sub>2</sub>Cu<sub>3</sub>O<sub>7</sub> and Au are given in Figure 5.2. From this data it is clear that above  $T_c$  the contact potential is linearly dependent on the current (Omic behavior), while it is nonlinear below  $T_c$ . The difference between the IV curves above and below  $T_c$  is associated with the change of state of the superconductor from normal to superconducting. The non-omic contact behavior witnessed below  $T_c$ , may be due to several different processes, but before embarking on how proximity effects influences  $V_c$ , it will be necessary to elaborate on the nature of the electronic states in the superconductor and explain how these affect the current transport across the S/N interface.

When electrons start pairing to form Cooper pairs at  $T_c$ , a superconductor bandgap opens. This superconducting bandgap is conceptually similar, but significantly smaller than the bandgap known from semiconductors like Silicon. It is manifested as *single electrons* from the normal conductor with an energy smaller than the bandgap are unable to cross the S/N interface. There is, however, a process known as Andreev reflection<sup>2</sup> which allows for transport across the boundary for particles with energy lower than the bandgap. Briefly, when an electron with energy below the bandgap meets the S/N barrier from the N side, it cannot pass through the barrier because the "states" on the S side are filled with Cooper pairs (i.e. by pairs of electrons of opposite spin and momentum (See Section 1.2)). However, if the N electron combines with a second N electron of opposite spin and momentum, then the two electrons may pass through the barrier and join the superconducting state as a Cooper pair. The result is that a hole is generated with the momentum in the opposite direction of the incident electron. Thus, due to the opposite charge and momentum of the hole, the net effect is that  $2e$  charge is carried across the barrier.

The probability of Andreev reflections is dependent on the potential across the barrier. The nonlinearity of the IV curve witnessed in Figure 5.2 is therefore consistent with Andreev reflections. However, it is not the only mechanism which may lead to IV nonlinear behavior, spreading resistance etc. may also contribute. Even in the absence of spreading resistance etc. it is still

---

<sup>2</sup>See reference [70] for an excellent introduction to Andreev reflection.

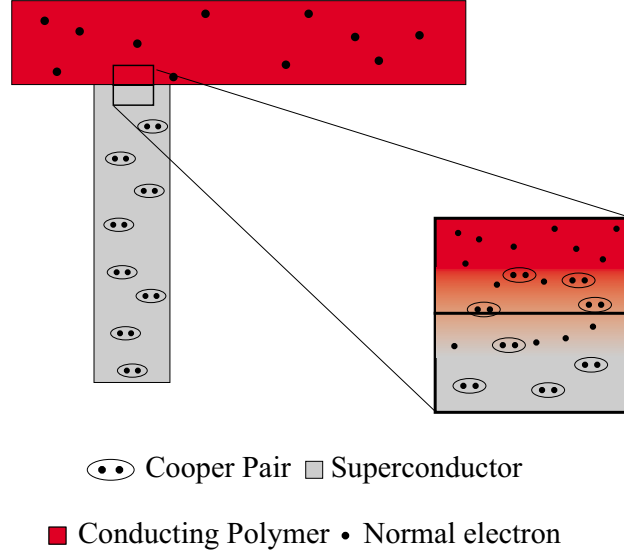


Figure 5.3: Diffusion of quasi-particles and Cooper pair across an S/N interface due to proximity effect.

difficult to obtain information about the proximity effect as will be detailed below.

The proximity effect is manifested by smearing the S/N interface (Fig. 5.3) and, thus, the band gap energy. This leads to changes in the relative probability of Andreev reflection to normal reflection at the interface. To model the precise response of the IV curve due to Andreev reflections in conjunction with the proximity effect would require theory which is well outside the scope of this text.

By combining the above observations, it becomes clear that it is difficult to extract proximity effect information even *if* the only processes responsible

for current transport across the S/N interface was Andreev reflections and proximity effect. This is because the proximity effect is a minor perturbation to the major processes of Andreev and normal reflection. In short, this is not the measurement of choice when trying to obtain quantitative information on the proximity effect. The use of contact resistance measurements should, however, not be completely discouraged. These samples are easy to fabricate and while low contact resistance is not proof that proximity effect is present, high contact resistance which shows an activated behavior upon cooling is proof that it is not<sup>3</sup>. Contact resistance measurements may, therefore, be used as a rapid test to discard a specific protocol or a combination of materials which would never be able to support the proximity effect due to chemical incompatibility.

Conceptually, the problem with transport measurements across the S/N barrier for proximity effect study is, that the Cooper pairs induced into the normal conductor will have to be converted into normal electrons before a measurement can be performed on them. Thus, these problems may be overcome by employing a superconductor probe that measures the Cooper pairs density in N directly. This is basically the S/N/S Josephson junctions described in Section 1.4. To reiterate here briefly: S/N/S Josephson junctions are more than two connected S/N, N/S junctions. The S/N/S junction allows for phase coherent transport of Cooper pairs across the N layer, which is readily detected as it is the source of the unique physical phenomena described in

---

<sup>3</sup>See reference [71] and [72] for the different contact behaviors.



Chapter one. One problem with S/N/S junctions is, however, that the number density of Cooper pairs in the superconductor electrodes is, like all S/N junctions, reduced by the proximity effect even before the N layer is reached. The strength of this suppression is dependent on the transport properties of the superconductor and the normal conductor. If these properties are unfavorably matched, then the critical current of the S/N/S junction may be immeasurably low. It will, therefore, be useful to calculate and/or measure this suppression before an S/conductive polymer/S junction is attempted.

## 5.2 Order parameter suppression at the S/N boundary

The object of this section is to gain quantitative insight into how strongly superconductivity is suppressed on the S side of an S/N interface by the proximity effect. To this end, the order parameter ( $\psi$ ) is introduced. Notice that the same symbol is used for the order parameter as for the superconductor wave function in Chapter one. This is because the order parameter is the solution to the Ginzburg-Landau (GL) differential equations which describe superconductivity at the mesoscopic level. It is outside the scope of this dissertation to introduce GL theory<sup>4</sup>, so for the present discussion it will only be necessary to know that the density of Cooper pairs is given by  $|\psi|^2$ .

To describe the suppression of superconductivity at the S/N interface, the parameter  $\gamma$  has been introduced [74] [75]

---

<sup>4</sup>The interested reader may refer to reference [73] for a introduction to GL-theory.

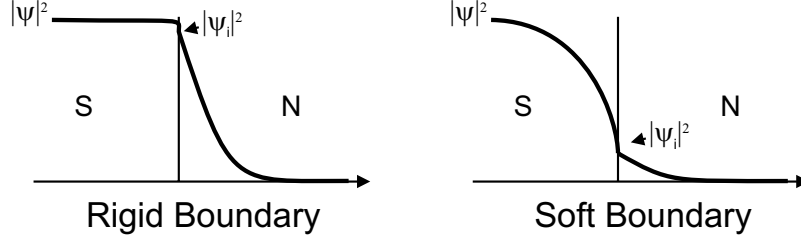


Figure 5.4: Order parameter suppression at the S/N interface (Schematic).

$$\gamma(T) = \frac{\rho_S(T) \cdot \xi_S(0K)}{\rho_N(T) \cdot \xi_N(T)} \quad (5.6)$$

where  $\rho_N$  and  $\xi_N$  is the resistivity and coherence length of the normal conductor. The variables  $\rho_S$  and  $\xi_S$  represent the normal state resistivity and coherence length of the superconductor, respectively. The two extreme cases of  $\gamma \gg 1$  and  $\gamma \ll 1$  are known as soft and rigid boundaries respectively (Fig. 5.4). In the rigid case, there is little suppression of the order parameter and a large density of Cooper pairs is present at the S/N interface. In the soft case, there is a large suppression which leads to a small Cooper pair density at the interface. Note that the boundary conditions are dependent on temperature (eq. 5.6).

The experimental values  $\rho_S(T)$ ,  $\xi_S(0)$ ,  $\rho_N(T)$ , and  $\xi_N(T)$  of the specific S/N sample are unknown, however, it is possible to calculate  $\gamma$ -values based on the combination of literature values and measured data. The details of these calculations are given in Appendix A and summarized in Table 5.1.

Table 5.1: Boundary parameters

	$\gamma_{a-axis}^{a)}$	$\gamma_{c-axis}^{a)}$
Single crystal YBa <sub>2</sub> Cu <sub>3</sub> O <sub>7</sub> and Type I polymer <sup>b)</sup>	0.17	333
Thinfilm and Type I polymer <sup>b)</sup>	17	3333
Thinfilm and Type II polymer <sup>b)</sup>	0.5	1

<sup>a)</sup>axis refers to the axis perpendicular to the S/N interface <sup>b)</sup>Type I and II are samples with high and low conductivity, respectively (see Appendix A).

Given that the  $\gamma$  values based on thin films data suggests either a soft or intermediate boundary, it seems pertinent to confirm this experimentally.

Golubov *et al.* developed a theory which correlates the ratio  $T_c^*/T_c$  and  $d_s/\xi_S^*$  to  $\gamma$  [75]. Where  $T_c^*$  and  $T_c$  are the transition temperature of the bilayer and the bulk superconductor respectively, while  $\xi_S^*$  and  $d_s$  are the superconductor coherence length extrapolated to 0K and the superconductor thickness respectively. The correlations of the theory in the limit where the N layer is so thick the proximity effect has decayed completely before the surface is reached ( $\xi_N \ll d_N$ ) is depicted graphically in Figure 5.5.

From Figure 5.5 it is clear that the largest suppression is found when the  $d_s/\xi_S^*$  ratio is small. As the coherence length is approximately ten times larger along the *ab*-plane than perpendicular to it, aligning the S/N interface perpendicular to this plane should yield the largest response. Thus, an *a*-axis film of the cuprate superconductor is the desired starting point for investigation of the suppression of superconductivity due to proximity effect. The practical

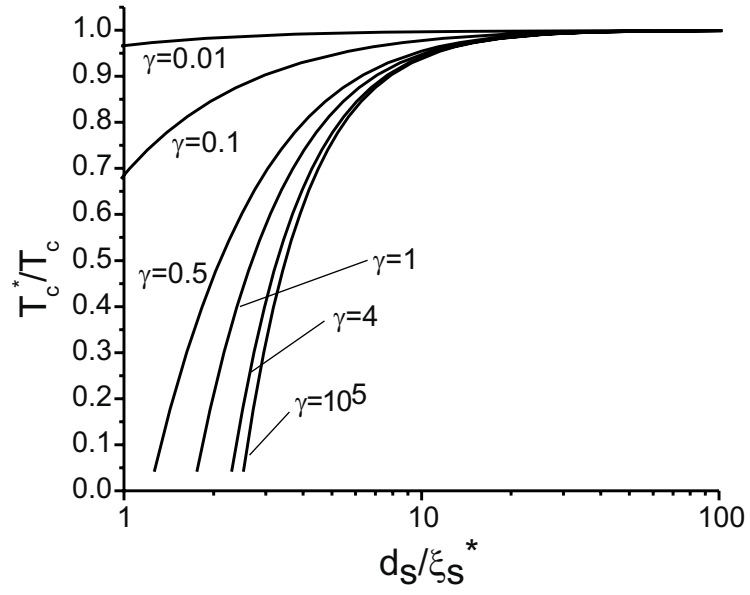


Figure 5.5: Transition temperature reduction as modeled by the theory of Golubov *et al.* [75]

aspects of obtaining a sample which will allow measurement of  $T_c^*/T_c$  in a geometry of known  $d_s$  is discussed in the next section.

### 5.3 Experimental: $S/\frac{N}{S}/S$ sample preparation and transport measurements

The thin films used in this chapter (unless otherwise noted) were  $\text{Y}_{0.6}\text{Ca}_{0.4}\text{Ba}_{1.6}\text{La}_{0.4}\text{Cu}_3\text{O}_7$  grown on  $1 \times 1\text{cm}^2$  polished MgO, using the protocol of Section 2.8 and the following deposition parameters: Pulse rate: 8Hz, Deposition time: 10min at  $780^\circ\text{C}$  and 20min at  $925^\circ\text{C}$ .  $P_{O_2, \text{deposition}}$ : 200mtorr. Anneal 30min at  $450^\circ\text{C}$ .

The films were patterned by shadow mask ablation (Section 4.1.1) before a  $100 \times 100\mu\text{m}^2$  section was thinned by AFM using the protocol of Section 4.1.2. Immediately after AFM thinning, the sample was transferred to the glovebox for poly-pyrrole deposition. The pyrrole was polymerized from a solution of 0.1M pyrrole and 0.1M  $[\text{Bu}_4\text{N}][\text{PF}_6]$  in dry acetonitrile, using the electrochemical protocol of Section 4.1.4 (see Fig. 5.8). The films were then rinsed with acetonitrile and undoped using a 0.1M  $[\text{Bu}_4\text{N}][\text{PF}_6]$ /acetonitrile solution and the protocol of Section 4.1.4. Following an extensive rinse with dry acetonitrile, the samples were transferred from the glovebox to the cryostat. The cryostat was then pumped to a pressure  $<30\text{mtorr}$  within minutes. Extensive care was taken to minimize the time of exposure to ambient air during the transfer step.

Connections to the sample were made with previously sanded Cu-clips.

The R vs. T curves as well as IV curves were collected using the setup described in Section 2.9.

Once the transport data had been collected, the sample was transferred back to the glove box and doped using the same solution as was used to undope the sample (see Section 4.1.4 for doping and undoping protocol). The R vs. T and IV curves were obtained in the same manner as for the undoped sample.

The cycle of doping, collecting transport data, undoping and collecting transport data was repeated until the sample only exhibited  $T_c$  changes derived from corrosion (see section 5.4).

#### 5.4 $S/\frac{N}{S}/S$ sample geometry

The sample used for these transport measurements differs from the ones described in the last section in that a) the area of the thinned section is much larger, b) no blocking layer is employed, rather, all unwanted polymer is removed by scraping with a wooden stick, and c) the acetonitrile solution used for electropolymerization only consists of pyrrole and  $[\text{Bu}_4\text{N}][\text{PF}_6]$  electrolyte. The motivation for these changes are briefly: a) Enhancing the area will enhance the resistance of the thinned section compared to the whole bridge making the signal to background ratio larger. b) The use of a blocking layer exposes the film to a corrosive environment, which would require that the sample be thinned until this layer had been removed. c) Poly-pyrrole with the  $\text{PF}_6^-$ -counter ion has previously been studied intensively in literature, simplifying the analysis greatly [10, 76, 77].

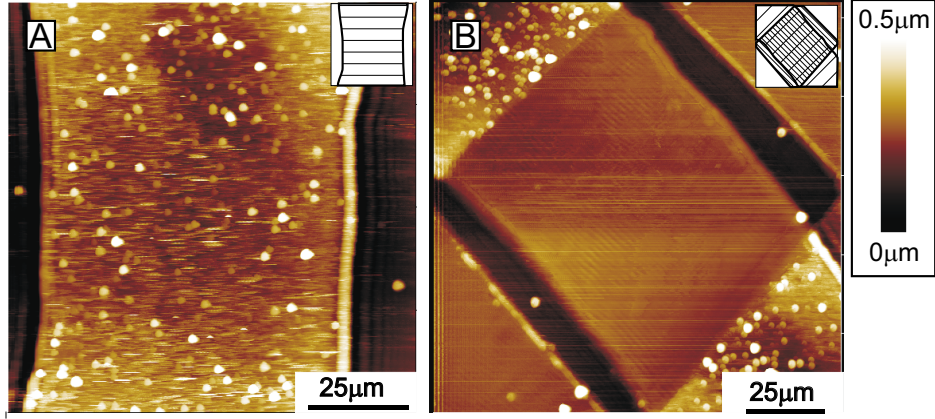


Figure 5.6: AFM of a bridge before A) and after B) thinning. Inset: Sample schematic, hatched area are thinned section and superconductor thus cross-hatched is thinned superconductor. (Image B was collected at a scan angle  $45^\circ$  to avoid noise lines being confused with surface features.)

As shown in Section 5.2, any qualitative analysis requires detailed knowledge of the geometry of the sample. The first objective of this section is, therefore, to obtain the morphology and the thickness of the thinned section. Figure 5.6 shows a sample of the same batch as used for the transport properties measurements described below. The actual sample is not shown as gathering an AFM image would prolong exposure to ambient atmosphere. However, Figure 5.6 shows that morphology of the thinned region appear smooth without the laser droplet protrusions found on the original bridge.

Gauging the thickness of the bridge is complicated by debris from the ablation patterning process, which is present on both the bridge and on the ablated surface. Thus, to measure the true thickness of the superconducting

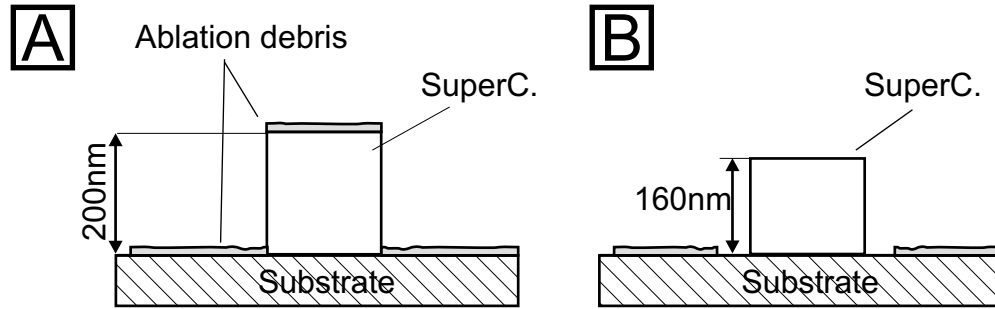


Figure 5.7: Superconductor bridge profile. A) Area not thinned. B) Thinned area.

layer another film from the same batch was patterned by photolithography and its thickness measured to  $200\text{nm} \pm 10\text{nm}$  (Fig. 5.7A). Returning to the sample used for conductivity measurement, the original superconductor bridge profile was revealed again after all transport properties had been obtained by transferring the polymer to an adhesive surface. The height of the thinned section was subsequently measured to be  $\sim 160\text{nm}$ . Note that this height was measured from the top of the bridge onto the bottom of the section cleaned off during AFM machining. The measured thickness should, therefore, be considered an upper estimate as the thinning process may have removed some of the MgO substrate (Fig. 5.7A).

As shown in Section 5.2, knowledge of four parameters is required in order to determine if the poly-pyrrole/superconductor interface exhibit rigid or soft boundary conditions. These were: The thickness of the superconductor layer ( $d_s$ ), which was just shown to be  $\sim 160\text{nm}$ ; the coherence length of



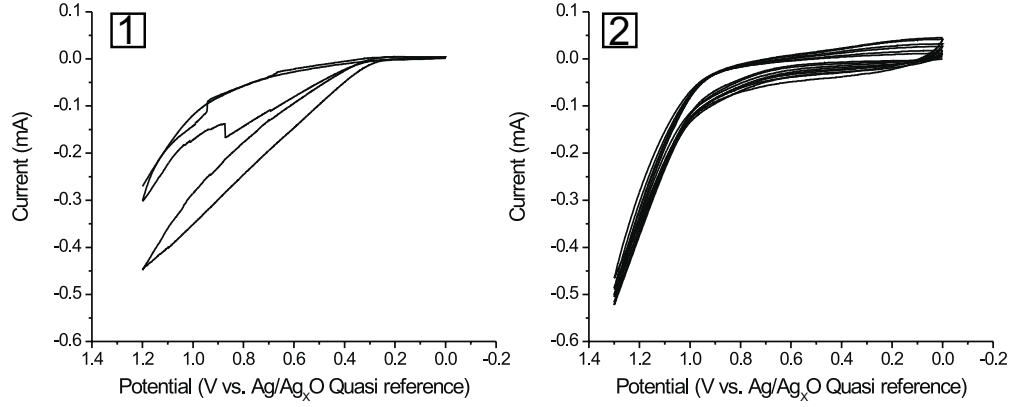


Figure 5.8: Polymer growth on transport measurement sample. 1) Initial scans 2) Polymer growth scans. (Scan rate= $100\text{mVs}^{-1}$ ,  $0.1\text{M}$  pyrrole and  $0.1\text{M}$   $[\text{Bu}_4\text{N}][\text{PF}_6]$  in dry acetonitrile)

the superconductor ( $\xi_s$ ) and the transition temperature of the bilayer in the absence ( $T_c$ ) and the presence of the proximity effect ( $T_c^*$ ). The coherence length is not a measurable quantity in our sample setup, so further analysis will rely on literature values (see Section 5.6). The last two parameters,  $T_c$  and  $T_c^*$  were obtained by measuring how the transport properties of the superconductor are affected by the presence and absence of mobile charge carriers in the poly-pyrrole layer. These transport measurements are described in Section 5.5. The remainder of this Section is devoted to describing the polymer part of the superconductor/polymer bilayer.

The polymer was grown atop the  $\text{Y}_{0.6}\text{Ca}_{0.4}\text{Ba}_{1.6}\text{La}_{0.4}\text{Cu}_3\text{O}_{7-\delta}$  sample by polymerization of pyrrole using  $[\text{Bu}_4\text{N}][\text{PF}_6]$  as the electrolyte. The polymerization (Fig. 5.8) appears to follow the pattern described in the last chapter

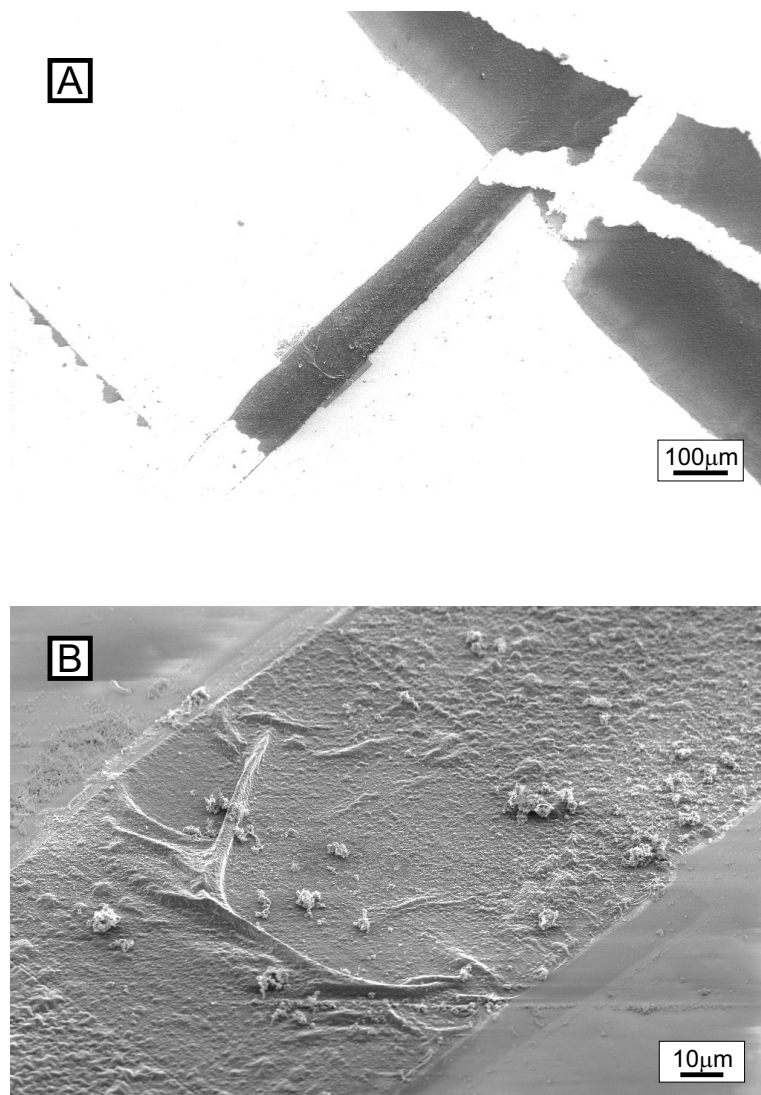


Figure 5.9: Scanning electron micrographs of polymer on current transport sample. A) Low magnification. Light areas are substrate and superconductor thin film, while dark areas are the polymer. B) An enlarged view of the polymer on top of thinned area. Note the folds suggesting partial delamination selected regions of the active area.

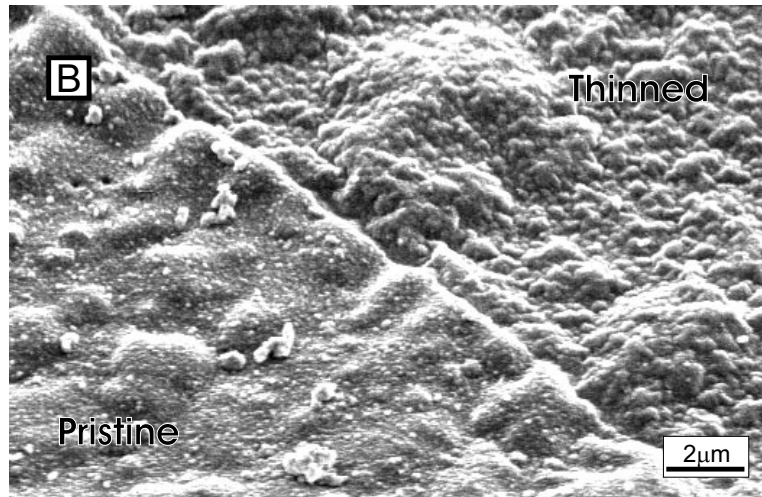
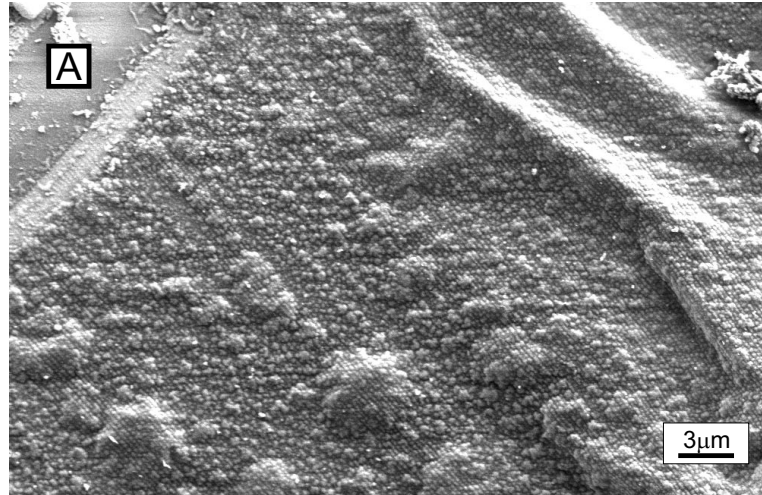


Figure 5.10: Polymer morphology on the  $\text{Y}_{0.6}\text{Ca}_{0.4}\text{Ba}_{1.6}\text{La}_{0.4}\text{Cu}_3\text{O}_7$  thin film sample. A) Thinned section. B) Thinned and unthinned section.

where the initial scans exhibit anodic currents that are not associated with polymer growth (Fig. 5.8A) followed by scans which clearly exhibit the fingerprints of growth (Fig. 5.8B).

Examining the sample after all transport measurements had been completed showed that ca. 80% of the bridge is covered with polymer (Fig. 5.9A) and that the thinned region represented  $\sim 20\%$  of the polymer covered bridge length. Closer inspection of the polymer atop the thinned area shows folds which are consistent with some degree of delamination. However, the delamination does not extend over the hole of the thinned Section (Fig. 5.9B).

Enhancing the magnification further shows that the polymer atop the thinned section exhibits a pattern of thin lines (Fig. 5.10A) not found on the part of the sample which was not thinned (Fig. 5.10B). Interestingly, these lines are in the same direction and have the same spacing ( $\pm 10\%$ ) as the scan lines of the AFM.

## 5.5 Current transport properties of the $S/\frac{N}{S}/S$ superconductor conductive polymer bilayer structure

No conductivity measurements were performed on the sample prior to the electrochemical polymer deposition, as this would have prolonged exposure to ambient air.

To gauge the effect that the mobile charge carriers of the polymer has on the superconductor, at least two transport measurements must be performed. One measurement where the polymer is oxidized to the conducting

Label	Polymer state	Proximity effect	N-state Resistance
R1	Reduced	No	$R_{superc}$
O1	Oxidized	Yes	$\frac{R_{superc} - R_{polymer}}{R_{superc} + R_{polymer}}$
R2	Reduced	No	$R_{superc}$

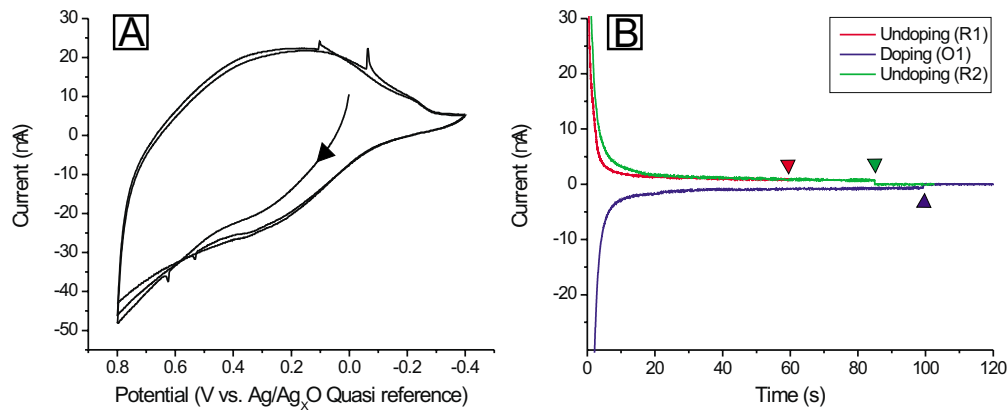


Figure 5.11: Doping and undoping of the superconductor/poly-pyrrole bilayer. A) CV (scan rate= $50\text{mV}\cdot\text{s}^{-1}$ ) B) Chronoamperometry (Potential step: undoping  $-0.4\text{V}$  and doping  $0.8\text{V}$  vs  $\text{Ag}/\text{Ag}_2\text{O}$ ) Arrows indicate when sample was removed from electrolyte solution ( $0.1\text{M}$   $\text{Bu}_4\text{NPF}_6$  in acetonitrile).

form and one where it is reduced to the insulating form. In this work, a third measurement with the reduced polymer was performed to gauge influence of the unavoidable corrosion experienced during the measurements.

The collected current transport data is summarized in Figure 5.12, Figure 5.13, and Table 5.2 and since these data are key to proving or disproving proximity effect in these structures the rest of this chapter is left for their detailed analysis and discussion. In this section a brief qualitative overview is

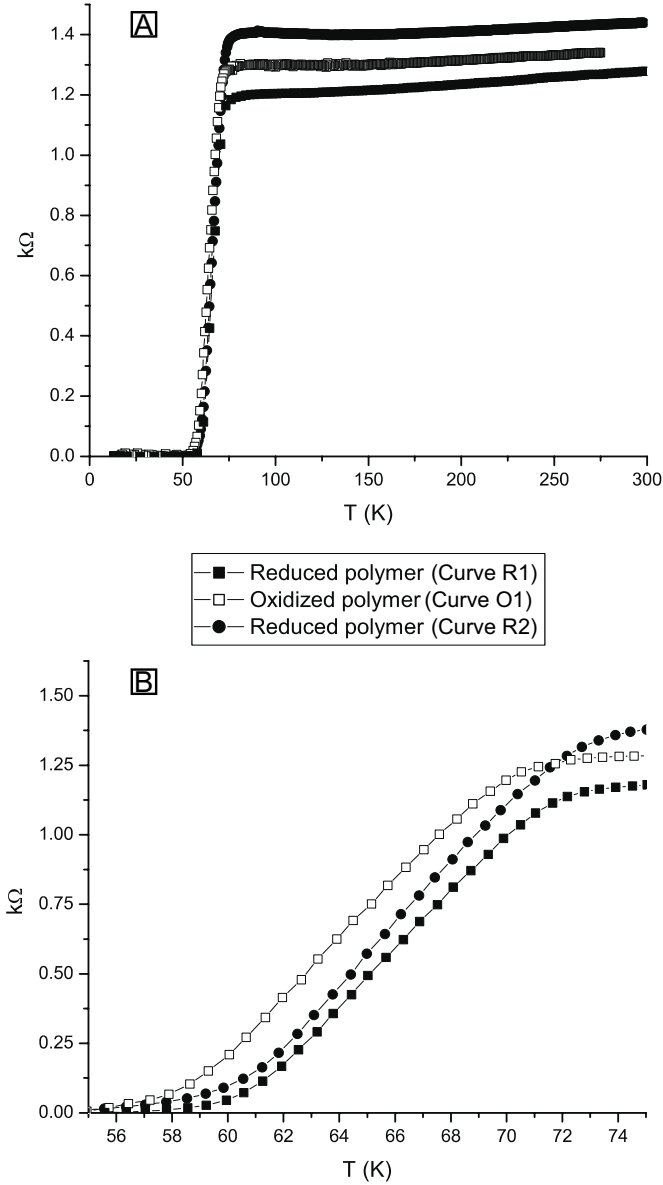


Figure 5.12: Resistance vs. temperature for the superconductor/polymer bi-layer. A) Complete data set. (source current  $10^{-6}$ A). B) Expansion of the region around  $T_c$ . (200nm X 800 $\mu$ m x 100 $\mu$ m bridge made from a  $a$ -axis  $\text{Y}_{0.6}\text{Ca}_{0.4}\text{Ba}_{1.6}\text{La}_{0.4}\text{Cu}_3\text{O}_7$  on MgO with a 160nm x 100 $\mu$ m x 110 $\mu$ m thinned section covered with poly-pyrrole, dopant  $\text{PF}_6^-$ .)

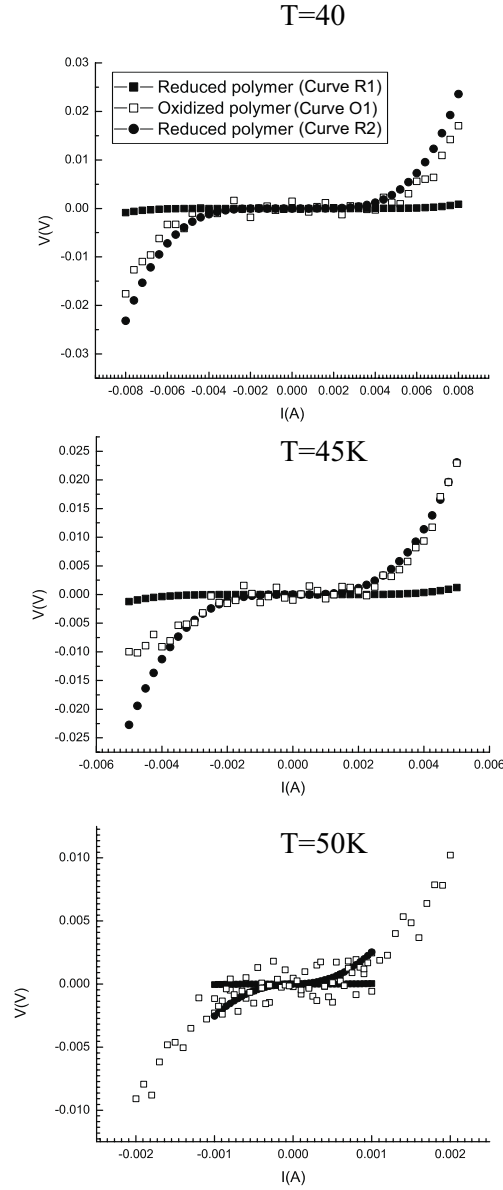


Figure 5.13: Current voltage response of the bilayer below  $T_c$ . (200nm x 800 $\mu$ m x 100 $\mu$ m bridge made from an  $a$ -axis  $Y_{0.6}Ca_{0.4}Ba_{1.6}La_{0.4}Cu_3O_7$  on MgO with a 160nm x 100 $\mu$ m x 110 $\mu$ m thinned section covered with poly-pyrrole, dopant  $PF_6^-$ . Same sample as Figure 5.12).

given.

First, focus is placed on the R vs. T curves. After polymerization the sample is left in the reduced form (curve R1). The  $T_{c,mid}$  of this curve is  $\sim 66\text{K}$ , and since there are no charge carriers in the polymer this is in the absence of any proximity effect. Then the polymer is oxidized, that is, charge carriers are introduced into the polymer and  $T_{c,mid}$  is suppressed to  $\sim 64\text{K}$  (curve O1). A suppression is to be expected due to corrosion alone as the sample has been exposed to ambient air during transfer from the cryostat to the glovebox and back. The polymer is then reduced again and  $T_{c,mid}$  recovers to  $\sim 66\text{K}$  (curve R2). This recovery of  $T_c$  is inconsistent with corrosion. Notice that the normal state resistance increased from curve R1 until curve R2. Corrosion is, therefore, a constant factor, even when reduction of the polymer leads to a  $T_c$  increase. Whether or not the modulation of  $T_c$  during redox cycling may be explained by the proximity effect is the subject of the next section, but before continuing it is important to elaborate the experimental conditions which do *not* lead to successful recovery of  $T_c$  after redox cycling.

The first group of samples that will be discussed were based on  $\text{NdBa}_2\text{Cu}_3\text{O}_{7-\delta}$  films patterned into a  $100\mu\text{m}$  wide bridge structure. Across this bridge was deposited a  $1\text{-}10\mu\text{m}$  wide poly-pyrrole line. The preparation protocol was the same as described in Chapter four, where a undecylamine blocking layer was employed to localize the polymer. Note that similar to the sample of Figure 5.12 no aminepyrrole tether was used. A representative example of the R vs. T response of this group of samples are show in Figure



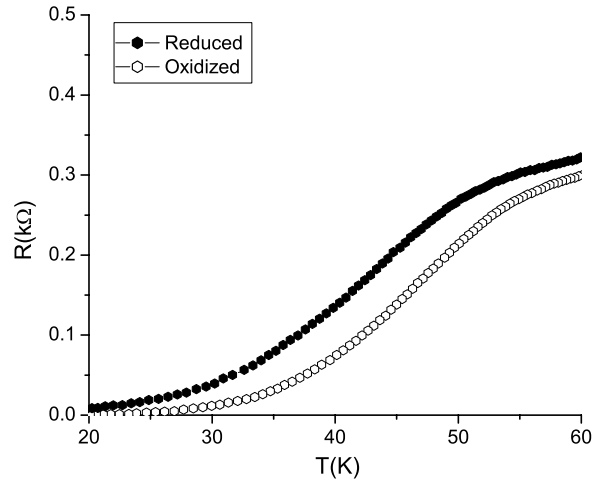


Figure 5.14: The lack of  $T_c$  recovery in the  $\text{NdBa}_2\text{Cu}_3\text{O}_{7-\delta}$  samples ( $I=10^{-6}\text{ A}$ ,  $100\mu\text{m}$  wide bridge with a  $<10\mu\text{m}$  thinned section covered with poly-pyrrole, dopant  $\text{BF}_4^-$ )

5.14.

The order of oxidation and reduction was reversed for these samples so that the measurement where the polymer was in its oxidized form was preformed before the measurement of the reduced form. This reversal makes it possible to measure a possible recovery of  $T_c$  by only performing two R vs. T measurements, which in turn minimizes the sample exposure to ambient air. This protocol was not used throughout this dissertation because it does not allow for gauging the contribution to  $T_c$  suppression due to corrosion, relative to the size of suppression due to the proximity effect. In spite of using the reversed protocol, no  $T_c$  recovery was ever witnessed in the tested samples (see Fig. 5.14 for the typical behavior).

The comparison between the behavior of the sample depicted in Figure 5.12, which does exhibit a recovery of  $T_c$ , and the samples exemplified by Figure 5.14 *would* suggest that recovery of  $T_c$  require that a large area of the bridge ( $100 \times 100 \mu\text{m}^2$ ) is covered with polymer. This *would* conversely mean that the effect was intimately coupled with the polymer oxidation state as expected if proximity effect was the origin of the suppression. It *would* also be consistent with the observation of Haupt *et al.* [66] that no recovery of  $T_c$  is witnessed when a bare superconductor bridge is redox cycled. However, great caution should be exerted when interpreting negative control experiments as the ones described above. This point will be elaborated further in the following.

The sample used to illustrate the ease by which one may obtain a false negative due to corrosion, is the familiar one of Figure 5.12. This sample

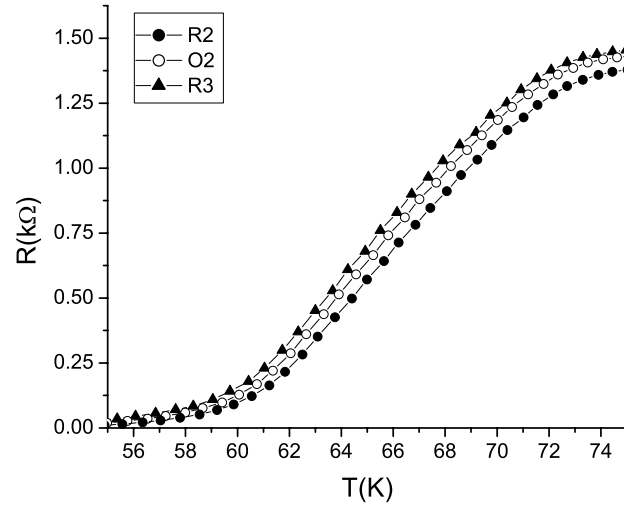


Figure 5.15: Second redox cycle (Same sample as Fig. 5.12,  $I_{source}=10^{-6}$  A,  $200\text{nm} \times 800\mu\text{m} \times 100\mu\text{m}$  bridge made from a  $a$ -axis  $\text{Y}_{0.6}\text{Ca}_{0.4}\text{Ba}_{1.6}\text{La}_{0.4}\text{Cu}_3\text{O}_7$  thin film on MgO with a  $160\text{nm} \times 100\mu\text{m} \times 110\mu\text{m}$  thinned section covered with poly pyrrole, dopant  $\text{PF}_6^-$ ).

shows a recovery of  $T_c$ , during the first reduction-oxidation-reduction cycle. However, the second oxidation-reduction which was preformed immediately after the first one (Fig. 5.15 Data label O2, R3 respectively), does not yield a recovery of  $T_c$  large enough to exceed the suppression caused by corrosion. (Fig. 5.15). Similar, decay in  $T_c$  recovery following repeated redox cycling was also found by Haupt [78]. In short, this means that any lack of  $T_c$  recovery following redox cycling may simply be due to corrosion and, thus, not the intrinsic properties of the sample. This is especially true for samples where the superconductor is not protected by a polymer layer either because it is intentionally left bare as in the experiment by Haupt *et al.* [66] or because the polymer has delaminated as in the  $\text{NdBa}_2\text{Cu}_3\text{O}_{7-\delta}$  samples described above.

## 5.6 Analysis and discussion of current transport properties of superconductor/conductive polymer bilayers

The object of this section is a) to show how the redox state (i.e. doping level) of the polymer affect the transport properties of the superconductor and b) to try to explain the cause of this effect.

Normally, S/N bilayers are examined for proximity effect by comparing measurements on the bare S layer to measurements of the bilayer. While ideally the S layer would be the same in both measurements it is often found that the deposition of the second layer affects the S layer (see Section 1.6). The polymer/superconductor samples described in this dissertation have two

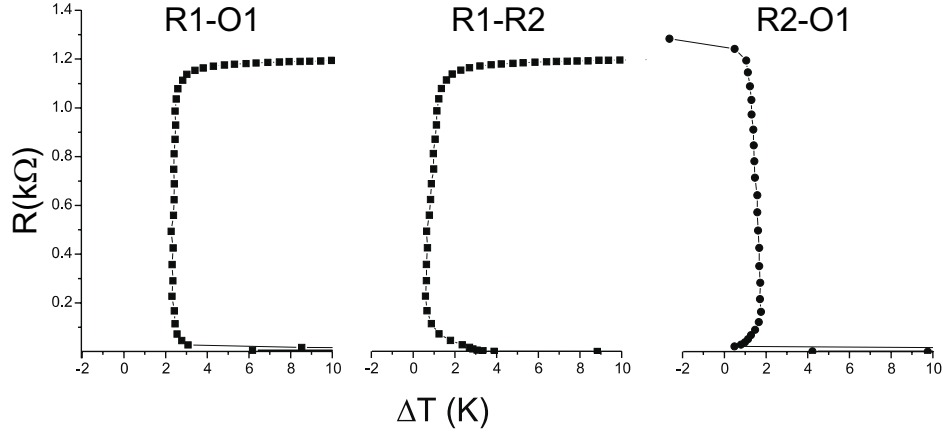


Figure 5.16: Transition temperature differences due solely to corrosion (R1-R2), and due to the combination of corrosion and change in oxidation state (R1-O1) (R2-O1). (Data from Figure. 5.12) (Note: The effect of corrosion is an increase in  $\Delta T_c$  for curve R1-O1, but a decrease for curve R2-O1).

advantages compared to the previously studied inorganic S/N bilayers. First, low temperature processing is used to deposit the N layer. This minimizes the problem of interdiffusion between the S and the N layer commonly found during deposition at elevated temperature. Second, the polymer can be reversibly modulated from an insulating to a conductive state. This makes it possible to deconvolute effects which are coupled with the redox state of the polymer from those which are not. Thus, returning to the data of Figure 5.12, the difference between curve R1 and curve R2 (Fig. 5.12) provides a measure of how corrosion has affected the sample (Fig. 5.16) as the oxidation state of the polymer is identical. Furthermore, since curve O1 was obtained after curve R1 and before curve R2, the differences R1-O1 and R2-O1 represents the upper

Table 5.3: Modulation of  $T_c$  for Polypyrrole/YBa<sub>2</sub>Cu<sub>3</sub>O<sub>7</sub> bilayers

$d_s(\text{\AA})^a)$ (Mixed a-c axis)	$T_c^*/T_c^a)$	$\xi_s^{*c)}$
200 <sup>b)</sup>	0.32	<66Å
500	0.83	83Å
1500	0.98	86Å

<sup>a)</sup> adapted from reference [66]

<sup>b)</sup> 800Å film deposited over a 1500Å step edge

<sup>c)</sup> Calculated using the theory of Golubov *et al.* [75]

and lower limits, respectively, for the change in current transport properties due to the change of polymer oxidation state (Fig. 5.16). It is, thus, clear that changing the state of the polymer from the state with few charge carriers of low mobility (reduced) to the state with many charge carriers of high mobility (oxidized) yields a suppression of  $\Delta T_{c,mid} = 1.5 \pm 0.5\text{K}$  or

$$0.96 < T_{c,mid}^*/T_{c,mid} < 0.98$$

where  $T_{c,mid}^*$  and  $T_{c,mid}$  are the transition temperatures when the polymer is conducting and isolating, respectively<sup>5</sup>. *Suppression of  $T_c$  caused by changing the sample characteristics from a S/I to a S/N bilayer is qualitatively consistent with the superconducting proximity effect.* Similar effects have been witnessed by Haupt *et al.* using mixed *a-c*-axis YBa<sub>2</sub>Cu<sub>3</sub>O<sub>7</sub> / poly-pyrrole bilayers, and selected data from this study is given in Table 5.3.

Returning to the processed data of Figure 5.16 where the geometry is known in greater detail; the height of the thinned section was estimated at

---

<sup>5</sup>Note there is some uncertainty in the definition of  $T_{c,mid}$  as 50% of the normal state resistance is not the same resistance in curve A to C.

160nm of which  $\sim 500\text{\AA}$  is the template layer deposited to ensure  $a$ -axis growth (Section 2.10). This template layer will also impose a proximity effect as it is a normal state conductor. However, this will not shorten the superconducting layer thickness by more than approximately  $d = 4 \cdot \xi_s^* = 64\text{\AA}$  which is within the error of the calculation. Using a thickness of  $1100\text{\AA}$  when examining the suppression of  $T_c$  in the framework of the theory of Golubov *et al.* [75] leads to the  $\xi_s^*$  values which seem unreasonably large ( $\xi_s^* > 63\text{\AA}$ )<sup>6</sup>, when compared to single crystal values for  $\text{YBa}_2\text{Cu}_3\text{O}_7$  ( $\xi_s^* = 16\text{\AA}$ ) [79]. A similar trend is found in the data of Haupt *et al.* (Table 5.3). Two potential reasons for the discrepancy between theory and experiment immediately arise. First, the theory of Golubov *et al.* while having predicted the behavior of metallic superconductors in combination with both metal [75] and semiconductors [80], may not be adequate for the description of conductive polymer/High- $T_c$  bilayers. Second, while  $\xi_s^*$  is normally considered a constant associated with a material composition, it may not be correct to use a value derived from single crystal experiments to describe the  $a$ -axis  $\text{Y}_{0.6}\text{Ca}_{0.4}\text{Ba}_{1.6}\text{La}_{0.4}\text{Cu}_3\text{O}_{7-\delta}$  thin films. Indeed, there are several observations which suggest that the superconductive properties of the sample described in Section 5.5 are not similar to those of single crystals. For example, the transition from the normal to the superconducting state ( $\Delta T_c$ ) occurs over more than 10K (Fig. 5.12) while the literature suggest that it should occur within 1K in a single crystal sample [79]. Furthermore, the critical current density is substantially lower than what is found

---

<sup>6</sup>Based on softest possible boundary ( $\gamma=\infty$ ,  $d_s=1100\text{\AA}$ ,  $T_c^*/T_c = 0.98$ )

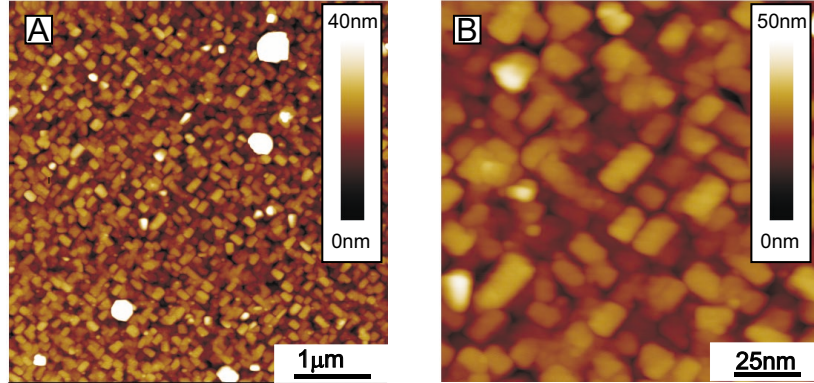


Figure 5.17: AFM image of  $\text{Y}_{0.6}\text{Ca}_{0.4}\text{Ba}_{1.6}\text{La}_{0.4}\text{Cu}_3\text{O}_{7-\delta}$   $a$ -axis film morphology before thinning. A)  $5 \times 5 \mu\text{m}^2$  and B)  $1.5 \times 1.5 \mu\text{m}^2$  scan area AFM images.

in literature for highly ordered thin films<sup>7</sup> ( $j_c=10^4 \text{ A}\cdot\text{cm}^{-2}$  vs  $j_c=10^6 \text{ A}\cdot\text{cm}^{-2}$  at  $T/T_c \approx 0.8$ ). The source of this suppression is to be found in the film morphology (Fig. 5.17), which clearly show that the film is a collection of aligned grains. Thus, while XRD patterns may have suggested a single crystal film, this is, in fact, not the case. The XRD pattern instead stems from several single crystal grains which are crystallographically aligned. This means that the resistance associated current transport is likely to be dominated by the transport between grains as the grain boundaries is where the material exhibits least order. The problem before us is, therefore, conceptually a known one: supercurrent transport between superconductors separated by an area where superconductivity is weakened, i.e. Josephson-like junctions. These junctions are also known as grain boundary junctions (GBJ).

---

<sup>7</sup>Reference [14] p.157



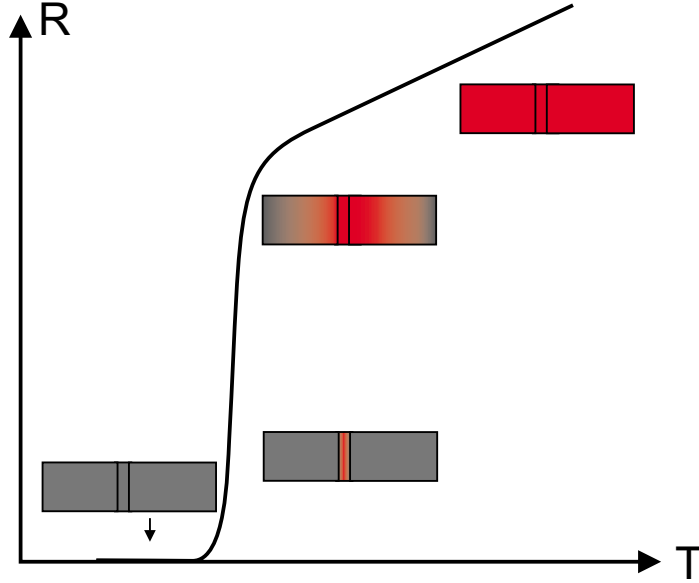


Figure 5.18: Grain boundary junction as it passes from normal conductor to superconducting (red is normal and gray is superconducting state respectively)

Quantitative modelling of current transport across a GBJ's is still a source of great debate<sup>8</sup> and adding a polymer layer with alterable transport properties does not simplify the analysis, at least not until the cross sectional geometry and composition of the grain boundaries is known.

With this in mind, the first observation to be made is that the relative contribution of grain boundary to the total resistance of the sample is enhanced as the temperature is lowered through the transition from normal to superconducting (Fig. 5.18). It is, therefore, expected that *if* the  $T_c$  depression associated with oxidizing the polymer is due to the modulation of the

---

<sup>8</sup>See reference [81] for a current review of GBJ.

Table 5.4: Superconductive properties of oxygen deficient single crystal<sup>a)</sup>

	YBa <sub>2</sub> Cu <sub>3</sub> O <sub>6.65</sub>	YBa <sub>2</sub> Cu <sub>3</sub> O <sub>7</sub>
$T_c$	$\approx 60\text{K}$	92K
$\xi_{s, ab-plane}(T = 0)$	20Å	16Å
$\xi_{s, c-axis}(T = 0)$	4.5Å	3Å
<sup>a)</sup> reference [82]		

grain boundaries, then this effect would be more pronounced in the lower part of the R vs. T curve. This is indeed found as  $\Delta T_c$  increases until approximately 90% of the transition is complete (Fig. 5.16 curve R2-O1)<sup>9</sup>. In the last 10% of the curve any effect is obscured by corrosion as shown by curve R1-R2 (Fig. 5.16).

One model for GBJ is a variation of the S/I/S junction: The S/S'/I/S'/S junction, where S' is a superconductor with lower transition temperature than S. The reduction of S to S' can be rationalized as GBJ have been shown to be oxygen deficient [82], which in turn is known to lower the transition temperature (see Section 2.1). This is important as it has also been shown that in single crystals, lowering the oxygen content increases the coherence length (Table 5.4). While an enhancement of  $\xi_s$  around GBJ is *suggestive* that the proximity effect may extend deeper into the film, which in turn will yield a larger suppression of  $T_c$ , it does not *prove* that the effect is sufficient to justify size of the  $T_c$  suppression that has been measured. To obtain a more detailed estimate on how proximity effect influences GBJ's would require new

---

<sup>9</sup>Note that the behavior of curve R1-O1 does not show the same trend as it contains both negative corrosion effect as well as the suppression from changing the oxidation state of the polymer.

measurement on a single junction of known geometry and as well as a thorough theoretical analysis. However, the proximity effect is not the only mechanism which may explain the redox induced suppression of  $T_c$ . Electromigration of oxygen may also play some role as detailed below.

Knowing that the S' layer is deficient in oxygen and that the oxygen atoms can migrate, even at room temperature under electric field gradients suggest, that oxygen would move away from the I layer during oxidation and toward it during reduction of the polymer. This migration would greatly alter the transport properties of the GBJ as the effective thickness and the electron transport characteristic of the S' layer are changed. Oxygen migration has previously been used to explain how the transport properties of GBJ change when large static fields are applied across the junction [83].

Before closing, it is necessary to address why when measuring the IV behavior below  $T_c$  does not show the recovery of the superconducting properties after reducing the polymer (curve R2). Two explanations immediately arise. First, corrosion may obscure the effect in the IV curves as illustrated by the large difference between curve R1 and curve R2<sup>10</sup>. Second, the conductivity of the polymer decreases as it is cooled and the size of the proximity effect is, therefore, expected to be smaller at lower temperatures.

**To summarize:** From the studies of thinned high- $T_c$  film/poly-pyrrole bilayers presented in this chapter it has been shown that  $T_c$  of these bilay-

---

<sup>10</sup>See Section 5.5 for a discussion of the adverse effect of corrosion.

ers may be semi-reversibly modulated by cycling the redox state of polymer. Unique to the sample used in this study is the level of knowledge of the geometry of the sample, which allowed for quantitative analysis of the  $T_c$  modulation in the framework of the proximity effect. This analysis shows that the coherence length and, thus, the spacial extent of the suppression of superconductivity is much larger than what is expected based on literature values of the superconductor coherence length. It is suggested that this behavior is due to the structure of the superconductor thin film which was shown to contain a large number of grain boundaries.

While the grain boundaries make it possible to explain the witnessed suppression of  $T_c$  in the standard frame work of the proximity effect they also make other possible mechanisms plausible, e.g. oxygen migration due to electric field during redox cycling of the polymer. To be able to deduce the origin of the redox induced  $T_c$  modulation, more experiments using different sample geometries will be needed. To this end the sample preparation protocol developed during this dissertation research may serve as a valuable tool that will allow for both localization of the polymer and control over the local superconductor geometry.

## Chapter 6

### Closing remarks

The goal of this dissertation was *to develop methodologies that allow for the fabrication of high temperature superconductor/organic-conductor composites with well defined geometries for the study of the superconductor proximity effect in polymers*. To this end, a number of new advances have been made including the observation that the R=Nd member of the  $\text{RBa}_2\text{Cu}_3\text{O}_7$  class of superconductors possess enhanced corrosion resistance. Furthermore, control over the crystallographic orientation of  $\text{Y}_{0.6}\text{Ca}_{0.4}\text{Ba}_{1.6}\text{La}_{0.4}\text{Cu}_3\text{O}_7$  thin films may be gained by deposition on a template layer. However, the most important advance toward the above goal is the ability to machine the superconductor on the nanometer scale using an AFM probe. This technique has been shown to yield samples where both the thickness of the superconductor and the location of the polymer could be controlled in great detail.

Using the AFM thinning technique has made it possible to produce  $S/\frac{N}{S}/S$  structures and measure their superconductive properties. This type of sample showed a semi-reversible suppression of  $T_c$  when the polymer was made conducting by electrochemical oxidation. *Qualitatively*, this is consistent

with the proximity effect and confirmed that earlier studies<sup>1</sup> on bilayers of YBa<sub>2</sub>Cu<sub>3</sub>O<sub>7</sub>/poly pyrrole could be extended to other, more stable members of the RBa<sub>2</sub>Cu<sub>3</sub>O<sub>7</sub> family. However, unique to the sample of this dissertation, the geometry was well known due to the use of the AFM thinning technique. In turn, this allowed for *quantitative* analysis, which interestingly showed that if the proximity effect is the source of the semi-reversible suppression of  $T_c$ , then it would require a coherence length ( $\xi_s$ ) much larger than what would be expected from previous experiments on single crystals. This observation led to the hypothesis that it is not the bulk of the film that is affected by the change in oxidation state by only the grain boundaries. However, further work both experimentally and theoretically will be needed before this hypothesis can be confirmed or rejected.

This dissertation research has also yielded a spin off from the fabrication of the  $S/\frac{N}{S}/S$  sample which shows how versatile the AFM machining technique is. The  $S/N/S$  junctions require a gap between the S electrodes smaller than approximately  $10 \cdot \xi_N$  if any Josephson current is to be measured [75]. For the conductive poly-pyrrole samples, this value may be as large as 40nm at 4.2K. While 40nm is close to, or below, the lower limit of the AFM thinning technique, it should be remembered that the calculation of  $\xi_N$  was based on a semiconductor model which describes inorganic semiconductors well, but may be inadequate conductive polymer due to their anisotropy. Therefore, measuring a Josephson current in a S/conductive polymer/S sample would

---

<sup>1</sup>See reference [66]

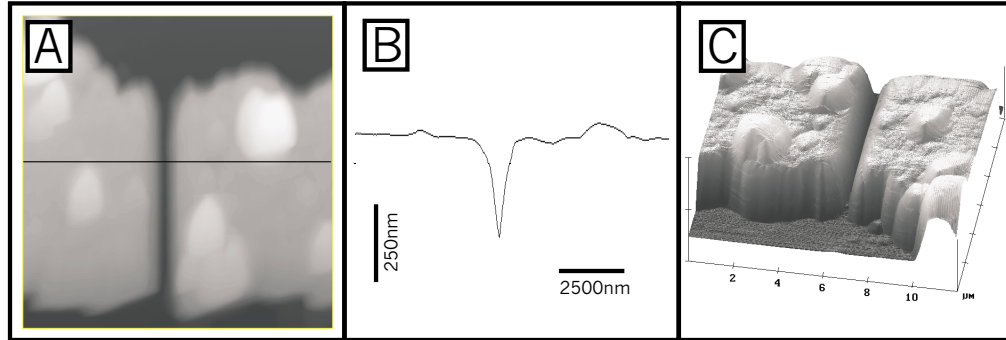


Figure 6.1: Superconductor bridge severed by AFM machining A)Top view. B) Cross-sectional profile. C) Perspective view.

yield proof that the conductive polymer is unique *also* in the superconducting state (Figure 6.1 illustrates the initial efforts towards this goal).

## Appendix



## Appendix A

### Calculation of $\gamma$ -values

#### Calculation of $\xi_N$ :

Using data from the class of poly-pyrrole<sup>1</sup> which yields the highest conductivities at low temperature (TYPE I hereafter) [10]

$$n_c = 2.3 \cdot 10^{28} \text{m}^{-3} \text{ and } \mu = 2.7 \cdot 10^{-5} \text{m}^2 \text{V}^{-1} \text{s}^{-1} \text{ (at 77K)}$$

$$n_c = 7.8 \cdot 10^{27} \text{m}^{-3} \text{ and } \mu = 5.7 \cdot 10^{-5} \text{m}^2 \text{V}^{-1} \text{s}^{-1} \text{ (at 4.2K)}$$

yields, using eq. 1.28

$$\xi_N(77\text{K}) = 6\text{\AA}$$

$$\xi_N(4.2\text{K}) = 40\text{\AA}$$

However, using transport properties from poly-pyrrole<sup>2</sup> with conductivities in the lower range (TYPE II hereafter)

---

<sup>1</sup>Polymerized at low temperature -20°C to -30°C using  $[\text{Bu}_4\text{N}^+][\text{PF}_6^-]$  as electrolyte and propylene carbonate as solvent.

<sup>2</sup>Polymerized using sodium p-toluenesulfonate in acetonitrile (reference [84]).

$$n_c = 2 \cdot 10^{27} \text{m}^{-3} \text{ and } \mu = 3 \cdot 10^{-6} \text{m}^2 \text{V}^{-1} \text{s}^{-1} \text{ (at 77K)}$$

$$n_c = 1 \cdot 10^{23} \text{m}^{-3} \text{ and } \mu = 2 \cdot 10^{-4} \text{m}^2 \text{V}^{-1} \text{s}^{-1} \text{ (at 4.2K)}$$

yields, using eq. 1.28

$$\xi_N(77\text{K}) = 0.9\text{\AA}$$

$$\xi_N(4.2\text{K}) = 1\text{\AA}$$

A note of caution. The above calculation were based on an isotropic Drude-like model, which is arguably the simplest model capable of describing normal-state charge transport. Also, the calculation is based on macroscopic transport properties while it is well known that these are dominated by interface between crystallites [8]. The resistance values described here should therefore be used as upper limits. With these reservations duly noted, the above calculations makes for a reasonable starting point for further analysis.

$\rho_N$  :

These values are directly available in the literature [10] [84]

	Type I ( $\Omega\text{m}$ )	Type II ( $\Omega\text{m}$ )
$\rho_N(77\text{K})$	$3 \cdot 10^{-5}$	$10^{-3}$
$\rho_N(4.2\text{K})$	$3 \cdot 10^{-5}$	0.3

$\rho_S$  :

The normal state cuprate superconductor properties may either be found in literature as single crystal  $\text{YBa}_2\text{Cu}_3\text{O}_7$  data (T just above  $T_c$ )<sup>3</sup>

$$\rho_s(\text{along } ab\text{-plane}) = 2 \cdot 10^{-6} \Omega\text{m} \text{ and } \rho_s(\text{along } c\text{-axis}) = 2 \cdot 10^{-4} \Omega\text{m}$$

or from our patterned  $\text{Y}_{0.6}\text{Ca}_{0.4}\text{Ba}_{1.6}\text{La}_{0.4}\text{Cu}_3\text{O}_7$  films<sup>4</sup>

$$\rho_s(c\text{-axis film}) \approx 2 \cdot 10^{-4} \Omega\text{m} \text{ and } \rho_s(a\text{-axis film}) \approx 2 \cdot 10^{-3} \Omega\text{m}$$

$\xi_S^*$  :

Here, we must rely on single crystal  $\text{YBa}_2\text{Cu}_3\text{O}_7$  data (at 0K)

$$\xi_s^*(\text{along the } ab\text{-plane}) = 16 \text{ \AA} \text{ and } \xi_s^*(\text{along } c\text{-axis}) = 3 \text{ \AA}$$

Using a mix and match approach, it is now possible to calculate  $\gamma$  values (at 77K):

Case 1: Single crystal  $\text{YBa}_2\text{Cu}_3\text{O}_7$  and type I polymer [79].

$$\begin{aligned} \gamma_{a\text{-axis}} &= \frac{2 \cdot 10^{-6} \Omega\text{m} \cdot 16 \text{ \AA}}{3 \cdot 10^{-5} \Omega\text{m} \cdot 6 \text{ \AA}} = 0.17 \\ \gamma_{c\text{-axis}} &= \frac{2 \cdot 10^{-4} \Omega\text{m} \cdot 3 \text{ \AA}}{3 \cdot 10^{-5} \Omega\text{m} \cdot 6 \text{ \AA}} = 333 \end{aligned}$$

---

<sup>3</sup>Reference [12]p.201

<sup>4</sup>The notation while confusing in this context is kept consistent with literature, i.e. in a  $c$ -axis film the current is transported along the  $ab$ -plane

where  $a$ -axis signifies the superconductor axis perpendicular to the S/N interface

Case 2: Thin film and type I polymer

$$\begin{aligned}\gamma_{a-axis} &= \frac{2 \cdot 10^{-4} \Omega_m \, 16 \text{\AA}}{3 \cdot 10^{-5} \Omega_m \, 6 \text{\AA}} = 17 \\ \gamma_{c-axis} &= \frac{2 \cdot 10^{-3} \Omega_m \, 3 \text{\AA}}{3 \cdot 10^{-5} \Omega_m \, 6 \text{\AA}} = 3333\end{aligned}$$

Case 3: Thin film and type II polymer

$$\begin{aligned}\gamma_{a-axis} &= \frac{2 \cdot 10^{-4} \Omega_m \, 16 \text{\AA}}{10^{-3} \Omega_m \, 6 \text{\AA}} = 0.5 \\ \gamma_{c-axis} &= \frac{2 \cdot 10^{-3} \Omega_m \, 3 \text{\AA}}{10^{-3} \Omega_m \, 6 \text{\AA}} = 1\end{aligned}$$

## Bibliography

- [1] W. A. Little. *Phys. Rev.*, 135(6A):A1416–A1424, 1964.
- [2] KUNGL. VETENSKAPSAKADEMIEN and THE ROYAL SWEDISH ACADEMY OF SCIENCES. Press Release. The 2000 Nobel Prize in Chemistry.
- [3] R. L. Greene, G. B. Street, and L. J. Suter. *Phys. Rev. Lett.*, 34(10):577–9, 1975.
- [4] Siegmur Roth. *One-dimensional metals : physics and materials science*. VCH, New York, 1995.
- [5] Klaus Bechgaard, Kim Carneiro, Malte Olsen, Finn Berg Rasmussen, and Claus S. Jacobsen. *Phys. Rev. Lett.*, 46(13):852–5, 1981.
- [6] M. Ahlskog. *Synthetic Metals*, 72:197–200, 1995.
- [7] Richard D. McCullough and Paul C. Ewbank. Regioregular, head-to-tail coupled poly(3-alkythiophene) and its derivatives. In Terje A. Skotheim, Ronald L. Elsenbaumer, and John R. Reynolds, editors, *Handbook Of Conducting Polymers*, pages 225–258. Marcel Dekker, New York, 2nd edition, 1998.

- [8] Tue Hassenkam. *Scale dependence in the electronic properties of a polythiophene derivative*. Dissertation, University of Copenhagen, 2001.
- [9] Reghu Menon, C. O. Yoon, D. Moses, and A. J. Heeger. Metal-insulator transition in doped conducting polymers. In *Handbook of Conducting Polymers*, volume 2, pages 27–84. Marcel Dekker, New Yourk, 1998.
- [10] T. H. Gilani and T. Ishiguro. *Synthetic Metals*, 84(1-3):845–846, 1997.
- [11] Charles P. Poole, Horacio A. Farach, and Richard J. Creswick. *Superconductivity*. Academic Press, San Diego, 1995.
- [12] W. Buckel. *Superconductivity. Fundamentals and Applications*. VCH Verlagsgesellschaft, Weinheim, 1991.
- [13] M. Cyrot and D. Pavuna. *Introduction to superconductivity and high- $T_c$  materials*. World Scientific, Singapore, 1992.
- [14] Rainer. Wesche. *High-temperature superconductors : materials, properties, and applications*. Kluwer Academic Publishers, Boston, Mass, 1998.
- [15] G. Deutscher and P. G. de Gennes. Proximity effects. In R.D. Parks, editor, *Superconductivity*, volume 2, pages 1005–1034. Marcel Dekker, New York, 1969.
- [16] J. J. Hauser, H. C. Theuerer, and N. R. Werthamer. *Phys. Rev.*, 136(3A):637–41, 1964.

- [17] J. Clarke. *Proc. Roy. Soc., Ser. A*, 308(1495):447–71, 1969.
- [18] P. G. de Gennes. *Rev. Mod. Phys.*, 36(1):225–37, 1964.
- [19] Hideaki Takayanagi and Tsuyoshi Kawakami. *Phys. Rev. Lett.*, 54(22):2449–52, 1985.
- [20] J. Seto and T. Van Duzer. *Low Temp. Phys.-LT 13, Proc. Int. Conf. Low Temp. Phys., 13th*, 3:328–33, 1974.
- [21] T. Nishino, U. Kawabe, and E. Yamada. *Phys. Rev. B: Condens. Matter*, 34(7):4857–60, 1986.
- [22] T. Nishino, E. Yamada, and U. Kawabe. *Phys. Rev. B: Condens. Matter*, 33(3):2042–5, 1986.
- [23] R. J. Cava. *Science*, 247(4943):656–662, 1990.
- [24] I. D. Brown. *J. Solid State Chem.*, 90(1):155–167, 1991.
- [25] J. P. Zhou, D. R. Riley, A. Manthiram, M. Arendt, M. Schmerling, and J. T. McDevitt. *Appl. Phys. Lett.*, 63(4):548–550, 1993.
- [26] *CRC Handbook Of Chemistry and Physics*. CRC Press, Boca Ration, 76 edition, 1996.
- [27] C. C. Torardi. Structural details of the high-Tc coper-based superconductors. In T.A Vanderah, editor, *Chemisty of superconductor materials*, pages 485–545. Noyes publications, Park Ridge, 1992.

- [28] A. Manthiram, J. S. Swinnea, Z. T. Sui, H. Steinfink, and J. B. Goodenough. *J. Am. Chem. Soc.*, 109(22):6667–6669, 1987.
- [29] J. P. Zhou, R. K. Lo, J. T. McDevitt, J. Talvacchio, M. G. Forrester, B. D. Hunt, Q. X. Jia, and D. Reagor. *J. Mater. Res.*, 12(11):2958–2975, 1997.
- [30] R. D. Shannon. *Acta Crystallogr. Sect. A*, 32:751–767, 1976.
- [31] M. J. Kramer, S. I. Yoo, R. W. McCallum, W. B. Yelon, H. Xie, and P. Allenspach. *Physica C*, 219(1-2):145–155, 1994.
- [32] R. Kelly and A. Miotello. Mechanisms of pulsed laser sputtering. In D. B. Chrisey and G. K. Hubler, editors, *Pulsed Laser Deposition of Thin Films*, pages 55–85. John Wiley and Sons, Inc., 1994.
- [33] Y. J. Li and K. Tanabe. *Physica C*, 324(3-4):198–210, 1999.
- [34] Y. Li and K. Tanabe. *J. Appl. Phys.*, 83(12):7744–7752, 1998.
- [35] Y. Li, X. Yao, and K. Tanabe. *Physica C*, 304(3-4):239–244, 1998.
- [36] M. C. Foote, B. B. Jones, B. D. Hunt, J. B. Barner, R. P. Vasquez, and L. J. Bajuk. *Physica C*, 201(1-2):176–182, 1992.
- [37] D. B. Chrisey and G. K. Hubler. *Pulsed Laser Deposition of Thin Films*. John Wiley and Sons, Inc., 1994.
- [38] Y. Ishimaru, J. G. Wen, N. Koshizuka, and Y. Enomoto. *Phys. Rev. B*, 55(17):11851–11859, 1997.



- [39] A. Ulman. *Chem. Rev.*, 96(4):1533–1554, 1996.
- [40] A. Ulman. *An introduction to ultrathin organic films from Langmuir-Blodgett to Self-Assembly*. Academic Press, INC, 1991.
- [41] R. G. Nuzzo and D. L. Allara. *J. Am. Chem. Soc.*, 105(13):4481–4483, 1983.
- [42] F. Xu, K. M. Chen, R. D. Piner, C. A. Mirkin, J. E. Ritchie, and J. T. McDevitt. *Langmuir*, 14(22):6505–6511, 1998.
- [43] D. Lednicer, J. K. Lindsay, and C. R. Hauser. *Journal of Organic Chemistry*, 23(5):653–655, 1958.
- [44] R. P. Vasquez, B. D. Hunt, and M. C. Foote. *Appl. Phys. Lett.*, 53(26):2692–2694, 1988.
- [45] J.E. Ritchie, W.R. Murray, K. Kershan, V Diaz, L. Tran, and J.T. McDevitt. *J. Am. Chem. Soc.*, 121(32):7447–7448, 1999.
- [46] J. T. McDevitt, S. G. Haupt, and C. E. Jones. Electrochemistry of high-Tc superconductors. In A.J. Bard and I. Rubinstein, editors, *Electroanalytical Chemistry*, volume 19, pages 337–486. Marcel Dekker, Inc., New York, 1996.
- [47] A. J. Bard and L. R. Faulkner. *Electrochemical methods*. John Wiley and Sons, New York, 2nd edition, 2001.
- [48] F. Xu, J. Zhu, and C. A. Mirkin. *Langmuir*, 16(5):2169–2176, 2000.

- [49] J.E. Ritchie, C.A. Wells, J.P. Zhou, J.N. Zhao, J.T. McDevitt, C.R. Ankrum, L. Jean, and D.R. Kanis. *J. Am. Chem. Soc.*, 120(12):2733–2745, 1998.
- [50] C. A. Alves and M. D. Porter. *Langmuir*, 9(12):3507–3512, 1993.
- [51] Thomas M. Schultz. *2 and 3 dimensional systems studied using X-ray crystallographic techniques*. Dissertation, Aarhus University, 1998.
- [52] H. L. Edwards, J. T. Markert, and A. L. Delozanne. *J. Vac. Sci. Technol. B*, 12(3):1886–1889, 1994.
- [53] H. Behner, K. Ruhrschopf, W. Rauch, and G. Wedler. *Appl. Surf. Sci.*, 68(2):179–188, 1993.
- [54] H. P. Lang, H. Haefke, G. Leemann, and H. J. Guntherodt. *Physica C*, 194(1-2):81–91, 1992.
- [55] J. Als-Nielsen, D. Jacquemain, K. Kjaer, F. Leveiller, M. Lahav, and L. Leiserowitz. *Physics Reports-Review Section Of Physics Letters*, 246(5):252–313, 1994.
- [56] M. K. Bernett and M.A. Zisman. *Journal of Physical chemistry*, 67:1534–1540, 1963.
- [57] D. Jacquemain, S. G. Wolf, F. Leveiller, F. Frolow, M. Eisenstein, M. Lahav, and L. Leiserowitz. *J. Am. Chem. Soc.*, 114(25):9983–9989, 1992.

- [58] Z.Q. Huang, A.A. Acero, N. Lei, S.A. Rice, Z.J. Zhang, and M.L. Schlossman. *Journal Of The Chemical Society-Faraday Transactions*, 92(4):545–552, 1996.
- [59] A. A. Acero, M. Y. Li, B. H. Lin, S. A. Rice, M. Goldmann, I. Benazouz, A. Goudot, and F. Rondelez. *J. Chem. Phys.*, 99(9):7214–7220, 1993.
- [60] S. W. Barton, A. Goudot, O. Bouloussa, F. Rondelez, B. H. Lin, F. Novak, A. Acero, and S. A. Rice. *J. Chem. Phys.*, 96(2):1343–1351, 1992.
- [61] D. Jacquemain, S. G. Wolf, F. Leveiller, M. Lahav, L. Leiserowitz, M. Deutsch, K. Kjaer, and J. Als-Nielsen. *J. Am. Chem. Soc.*, 112(21):7724–7736, 1990.
- [62] S. H. Tessmer, M. B. Tarlie, D. J. VanHarlingen, D. L. Maslov, and P. M. Goldbart. *Physical Review Letters*, 77(5):924–927, 1996.
- [63] Y. Levi, O. Millo, N. D. Rizzo, D. E. Prober, and L. R. Motowidlo. *Appl. Phys. Lett.*, 72(4):480–482, 1998.
- [64] Y. Levi, O. Millo, N. D. Rizzo, D. E. Prober, and L. R. Motowidlo. *Phys. Rev. B*, 58(22):15128–15134, 1998.
- [65] A. D. Truscott, R. C. Dynes, and L. F. Schneemeyer. *Physical Review Letters*, 83(5):1014–1017, 1999.
- [66] S. G. Haupt, D. R. Riley, J. Grassi, R. K. Lo, J. N. Zhao, J. P. Zhou, and J. T. McDevitt. *J. Am. Chem. Soc.*, 116(22):9979–9986, 1994.

- [67] R. K. Lo, J. E. Ritchie, J. P. Zhou, J. N. Zhao, J. T. McDevitt, F. Xu, and C. A. Mirkin. *J. Am. Chem. Soc.*, 118(45):11295–11296, 1996.
- [68] R.K. Kirschman, H. A. Notarys, and J. E. Mercereau. *Phys.Lett.*, 34A(4):209–211, 1971.
- [69] J. E. Mercereau and H. A. Notarys. *J.Vac.Sci.Technol.*, 10(5):646–651, 1973.
- [70] T. Schäpers. *Superconductor/semiconductor junctions*. Springer, Berlin, 2001.
- [71] S. G. Haupt, D. R. Riley, J. N. Zhao, and J. T. McDevitt. *Journal of Physical Chemistry*, 97(30):7796–7799, 1993.
- [72] J. W. Ekin, T. M. Larson, N. F. Bergren, A. J. Nelson, A. B. Swartzlander, L. L. Kazmerski, A. J. Panson, and B. A. Blankenship. *Appl. Phys. Lett.*, 52(21):1819–1821, 1988.
- [73] M. Tinkham. *Introduction to superconductivity*. McGraw Hill, New York, 2nd edition, 1996.
- [74] K. A. Delin and A. W. Kleinsasser. *Superconductor Science & Technology*, 9(4):227–269, 1996.
- [75] A. A. Golubov, M. Y. Kupriyanov, V. F. Lukichev, and A. A. Orlikovskii. *Sov. Microelectr.*, 12(4):191–197, 1983.

- [76] N. T. Kemp, A. B. Kaiser, C. J. Liu, B. Chapman, O. Mercier, A. M. Carr, H. J. Trodahl, R. G. Buckley, A. C. Partridge, J. Y. Lee, C. Y. Kim, A. Bartl, L. Dunsch, W. T. Smith, and J. S. Shapiro. *J. Polym. Sci. Pt. B-Polym. Phys.*, 37(9):953–960, 1999.
- [77] J. Joo, J. K. Lee, J. S. Baeck, K. H. Kim, E. J. Oh, and J. Epstein. *Synthetic Metals*, 117(1-3):45–51, 2001.
- [78] S. G. Haupt. *Conductive Polymer/High-temperature superconductor assemblies*. Dissertation, University of Texas at Austin, 1994.
- [79] U. Welp, W. K. Kwok, G. W. Crabtree, K. G. Vandervoort, and J. Z. Liu. *Physical Review Letters*, 62(16):1908–1911, 1989.
- [80] W. M. Vanhuffelen, T. M. Klapwijk, and Eptm Suurmeijer. *Phys. Rev. B*, 47(9):5151–5156, 1993.
- [81] H. Hilgenkamp and J. Mannhart. *Reviews of Modern Physics*, 74(2):485–549, 2002.
- [82] K. G. Vandervoort, U. Welp, J. E. Kessler, H. Claus, G. W. Crabtree, W. K. Kwok, A. Umezawa, B. W. Veal, J. W. Downey, A. P. Paulikas, and J. Z. Liu. *Phys. Rev. B*, 43(16):13042–13048, 1991.
- [83] J. J. Betouras, R. Joynt, Z. W. Dong, T. Venkatesan, and P. Hadley. *Appl. Phys. Lett.*, 69(16):2432–2434, 1996.
- [84] K. Kaneto and K. Yoshino. *J. Phys. Soc. Jpn.*, 55(12):4568–4569, 1986.

## Vita

Steen Brian Schougaard was born August 22, 1972, in Glostrup, Denmark. He is the son of Ernest and Vita Schougaard. After completing Gymnasium (general certificate of education) in 1992, he entered the University of Copenhagen. In 1998 he fulfilled the requirement for the Masters degree by defending his thesis "Exploration of symmetry and multidirectional charge transfer in design of 3rd order nonlinear chromophores: A joint experimental and theoretical investigation." He subsequently left Copenhagen and enrolled as a graduate student at The University of Texas at Austin. He is the recipient of the three year scholarship given out by the Danish research agency for studying aboard.

Permanent address: 2801 Breeze ter., Austin, TX, 78722

This dissertation was typeset with  $\text{\LaTeX}^\dagger$  by the author.

---

<sup>†</sup> $\text{\LaTeX}$  is a document preparation system developed by Leslie Lamport as a special version of Donald Knuth's  $\text{\TeX}$  Program.